MICROCOPY RESOLUTION TEST CHART
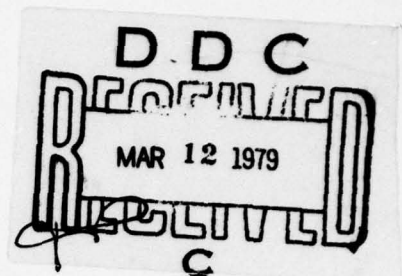
NATIONAL BUREAU OF STANDARDS-1963-A

Bell Laboratories
Western Electric

Lincoln Laboratory
MASSACHUSETTS INSTITUTE OF TECHNOLOGY

JOINT RADAR PROPAGATION STUDY

HILION - A Model of the

High-Latitude Ionospheric F2 Layer

and

Statistics of Regular Ionospheric

Effects at Ft. Churchill, 1968

D.A. Feinblum

R.J. Horan

October 1, 1973

Bell Laboratories
Western Electric

Lincoln Laboratory
MASSACHUSETTS INSTITUTE OF TECHNOLOGY

JOINT RADAR PROPAGATION STUDY

⑥

HILION - A Model of the High-Latitude Ionospheric F2 Layer and Statistics of Regular Ionospheric Effects at Ft. Churchill, 1968

D D C

RECEIVED

MAR 12 1979

C

⑩ D.A./Feinblum
R.J./Horan

⑪ 1 October 1973

⑫ 158 p.

⑮

79 03 07 016

374700

CONTENTS

CONTENTS (Continued)

ILLUSTRATIONS

ILLUSTRATIONS (Continued)

TABLES

HILION — A MODEL OF THE HIGH-LATITUDE IONOSPHERIC F2 LAYER
AND
STATISTICS OF REGULAR IONOSPHERIC EFFECTS
AT FT. CHURCHILL, 1968

Part 1 of this report discusses HILION (HIgh Latitude IONosphere),

1. INTRODUCTION

This document reports on two distinct, but related, ionospheric investigations; one is HILION, an effort to model many features of the high-latitude ionospheric F2 layer with emphasis on the nighttime trough, and the other is a statistical investigation of various ionospheric effects based on data taken at Ft. Churchill, Manitoba, Canada.

The HILION (High-Latitude IONosphere) modeling effort was undertaken in two main stages. The first stage was the modeling of many individual electron-density profiles using as input data values of electron density at various altitudes obtained by the Alouette I and II satellites. Programs were also developed to permit the similar modeling of Thomson Scatter data. The second stage was the ionospheric modeling proper, using the modeled profiles developed in the first stage as the input data.

The most distinctive feature of the high-latitude ionosphere is the trough, and it is on this feature that HILION concentrates. Indeed, it was found that during the nighttime, the trough and trough-wall system cover the region from roughly 50° to roughly 70° (in invariant magnetic coordinates); this latitude regime could be taken as the definition of the term "high latitude". During the daytime, there is no qualitative change in the F2 layer from mid-latitudes to the auroral oval.

The trough region is now sufficiently well understood that it is possible to describe its morphology and to outline the underlying physical processes which cause that morphology.

In the other *(second)* study, F2 critical frequency data ~~have been~~ *(were)* assembled and statistically analyzed for the ionosphere above Ft. Churchill. Similar investigations could be made for other stations.

The diurnal and seasonal variations of the peak critical frequency, foF2, have been depicted, and the possibility of determining foF2 at Ft. Churchill from either local or global parameters ~~has been~~ investigated. This restriction to a limited

region of the ionosphere permits the recognition of unexpected phenomena that might pass unnoticed in a more global study. One such investigation demonstrated a delayed influence of the planetary geomagnetic activity index, K_p, on ionospheric effects, i.e., foF2 was shown to be better correlated with K_p at some time different from the time of the observed foF2. The concept of a lagged K_p was applied to the HILION investigation and found to improve the ordering of the data for low to moderate levels of magnetic activity.

2. HILION — A MODEL OF THE HIGH LATITUDE IONOSPHERIC F2 LAYER

2.1 Preliminary Model

2.1.1 Background. The model described herein has been constructed to describe ionospheric electron densities to aid in radar propagation studies with emphasis on the neighborhood of the radar station at the Millstone Hill facility of Lincoln Laboratories of the Massachusetts Institute of Technology (latitude 42.6°N, longitude 71.49°W). The model is intended to be used for studies of the background ionosphere alone (especially under geomagnetic storm conditions) and as the background for studies of traveling ionospheric disturbances which serve to modulate this ambient electron-density pattern.

The most striking feature of the mid-to-high-latitude ionosphere is probably the highly localized region of very low electron densities at the F2 peak* which is observed at night at geographic latitudes from about 35°N to about 70°N. Muldrew [1965] [†] has described this region and has referred to it as the "main trough." Other authors have also called it the "mid-latitude trough," the "high-latitude trough" or the "Ottawa trough." The latitude of the trough depends primarily on the time of day, the day of the year, the longitude, and the magnetic activity index, K_p.[‡] To the north of the trough is the auroral region, described by Feldstein [1963] as an oval, and the polar region. The densities in these regions are higher than those in the trough and may be higher or lower than those to the south of the trough. The auroral region tends to exhibit irregular (latitudinal) variations of density which last for several hours. These variations were considered to be other (high-latitude) troughs by Muldrew [1965] but were interpreted by Nishida [1967] as distinct peaks of auroral precipitation superimposed on a wide trough.

Thomas and Andrews [1963] examined the relationship between the location of the trough and the high-altitude region of low electron density in the equatorial plane called the "knee" or plasmapause by Carpenter [1963]. It was found that the value of McIlwain's [1961] magnetic shell coordinate (L) is nearly constant in the trough at all longitudes. As local time or K_p varies, the L shell containing the trough changes. The lack of coincidence between curves of constant L and constant

---

*Throughout this document, unless otherwise specified, the word "density" denotes the electron number density at the peak of the F2 layer.

†References are listed alphabetically on page 4-1.

‡Tables of this index for three-hour ranges are published in "Solar Geophysical Data," H. I. Leighton, ed., U.S. Department of Commerce (Boulder, Colorado 80302). The usual scale runs 0, 0+, 1-, 1, 1+, ..., 9-, 9, regarded as equally spaced. In any numerical work, the symbols + and - are regarded as equivalent to +0.33 and -0.33 respectively, giving a scale of 0, 0.33, 0.67, 1, ..., 8.67, 9.

geographic latitude at the altitude of the F2 peak account for the known longitudinal dependence of the trough latitude.

2.1.2 Description of the model. The purpose of the present model is to permit the study of refraction of radar beams, not to predict average electron-density levels. Thus, the spatial variability of the density may be as important as the average values. It is clear that very small-scale latitudinal variations in electron . density will be unimportant (if the variations are slowly varying functions of altitude). However, due to the curvature of the earth, once the scale is of the order of a degree or more this need not be so. The consequence of the foregoing consideration is that the trough and the higher-latitude variability must not be smoothed into nonexistence by simple averaging of a large volume of data or by fitting an analytic expression which forces too much smoothing. This conclusion holds even though it may be impossible to predict where the densities are greater than average and where they are less than average on any given day.

The model discussed here assumes that the basic ionization pattern may be separated into a spatial variation at fixed local time and season, and a temporal variation which may be determined by examining a single longitude. This assumption is equivalent to assuming the longitudinal invariance of the trough latitude for fixed local times in a magnetic coordinate system (e.g., invariant coordinates, corrected geomagnetic coordinates). The basic pattern is then assumed to be varied due to solar influence. If the picture of the solar influence given by Thomas and Andrews [1963] is accurate, the closer the sun to the zenith, the closer the trough should be to the pole of the magnetic coordinates. However, over the United States and southern Canada, a small displacement toward geographic north is a good approximation to an equal displacement toward the pole of any of the magnetic coordinates, particularly since densities vary much more slowly with longitude than with latitude. North of the trough the solar variation decreases rapidly. For example, the diurnal motion of the northern edge of the auroral oval, as described by Feldstein [1963], exhibits a diurnal change of around three degrees in geomagnetic latitude at the most usual K_p values.

2.1.3 Spatial dependence for fixed date, time, and K_p. In order to avoid averaging the trough out of existence, the data used to fit the spatial variation were limited to what was available from three consecutive passes of the Alouette I satellite on October 24-25, 1962 [Muldrew, 1965] for latitudes above 40°N for geographic latitudes. In addition, the trough minimum was taken from a fourth pass. Ideally, a larger data base is more desirable, but only if a proper averaging scheme can be devised.

2-2

The following approximation is used to simulate a magnetic coordinate system: a north pole location is obtained in fitting the data, the latitude and longitude are transformed to a new colatitude θ' and longitude λ_m and then the latitude circles are distorted by the equation

$$\theta_m = \theta' \left(1 - d \cos 2\lambda_m\right) . \qquad (2-1)$$

Here θ_m is the colatitude in model coordinates, λ_m is the model longitude as before, and d describes the strength of the distortion. The model north pole location and d are chosen so that the four minima in electron density are as close to being at the same model latitude as possible.

The density pattern is described by fitting the logarithm of the electron density with the sum of four Gaussians and a quadratic function (Figure 2-1). One Gaussian represents the trough and a second adjusts the southern edge of the trough, while the remaining two represent a high-latitude ridge and trough which were present on the day examined. The quadratic function fits the smooth part of the density variation. The precise fitting equation is given in Section 2.1.4. There was one trough in the auroral region on the given day which was sufficiently variable in model latitude that it was averaged out and is not visible in the model.

On the passes used, the satellite orbit lay very close to the terminator (at a local time of 17:00 to 18:40) with a solar zenith angle of close to 90 degrees at all points in these orbits. Although the coding needed for including the diurnal variation of the trough position is included in the program used for fitting the data, the effects are small under the given conditions. Discussion of this effect is therefore postponed until the following section. Similar remarks hold for K_p, for it had a value of 5- on the first two passes and then changed to 4-.

In order to obtain electron-density maps it is necessary to know, among other things, the dependence of trough width and depth on local time and K_p, and the dependence of the background density on these two variables. Except for a local time near 18:00 and a K_p near 5-, fits for these quantities are based on insufficient data to be considered reliable. Consequently, results are presented only for 18:00 local time and K_p = 5-. These results are shown in Figure 2-2.

2.1.4 <u>Motion of the trough due to solar and magnetic effects</u>. The effect of sun on the trough position was deduced from a set of observations of the location of the center of the trough at the longitude of St. John's, Newfoundland over a period of six months (Figure 2-3) [<u>Muldrew</u>, 1965]. Because this data comes from a satellite, the local time at a given latitude varies only because of orbital precession. For Alouette I, the precession rate is such that local time varied by about two hours per month at the satellite crossing point of each parallel. Consequently, diurnal

2-3
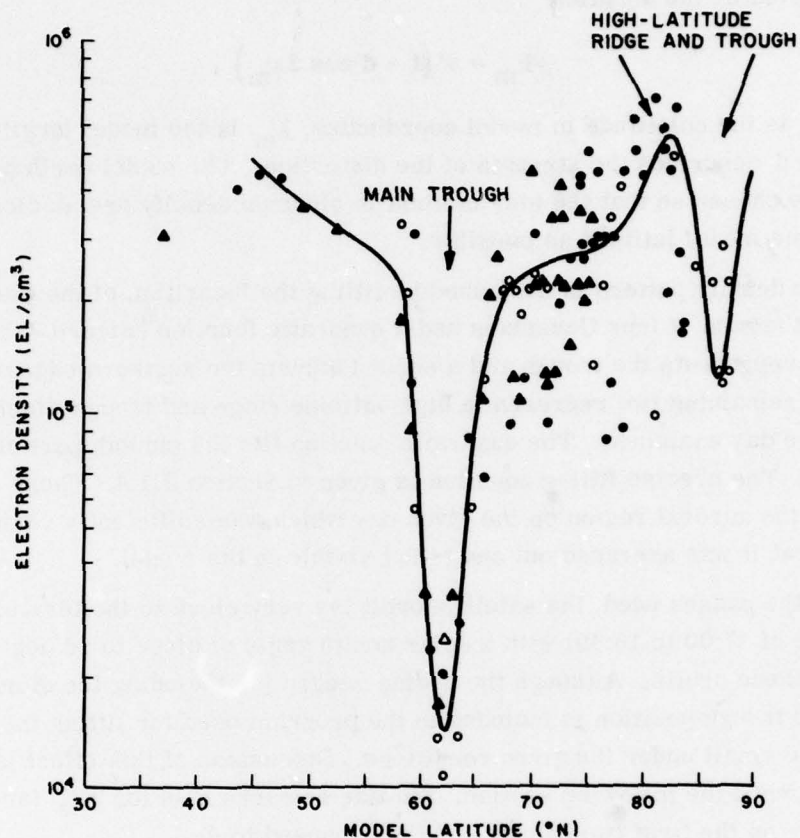
The curve is the electron density as derived from the model for October 24 at 18:00 local time for $K_p = 5-$. The points plotted with a given symbol are obtained from the same satellite pass and regressed to correspond to $K_p = 5-$. The data points were obtained at 18:00 local time (± 1 hr) during the night of October 24-25 (GMT).

Figure 2-1. The Spatial Dependence of the Trough Model Compared with the Data from Which It Is Obtained

2-4
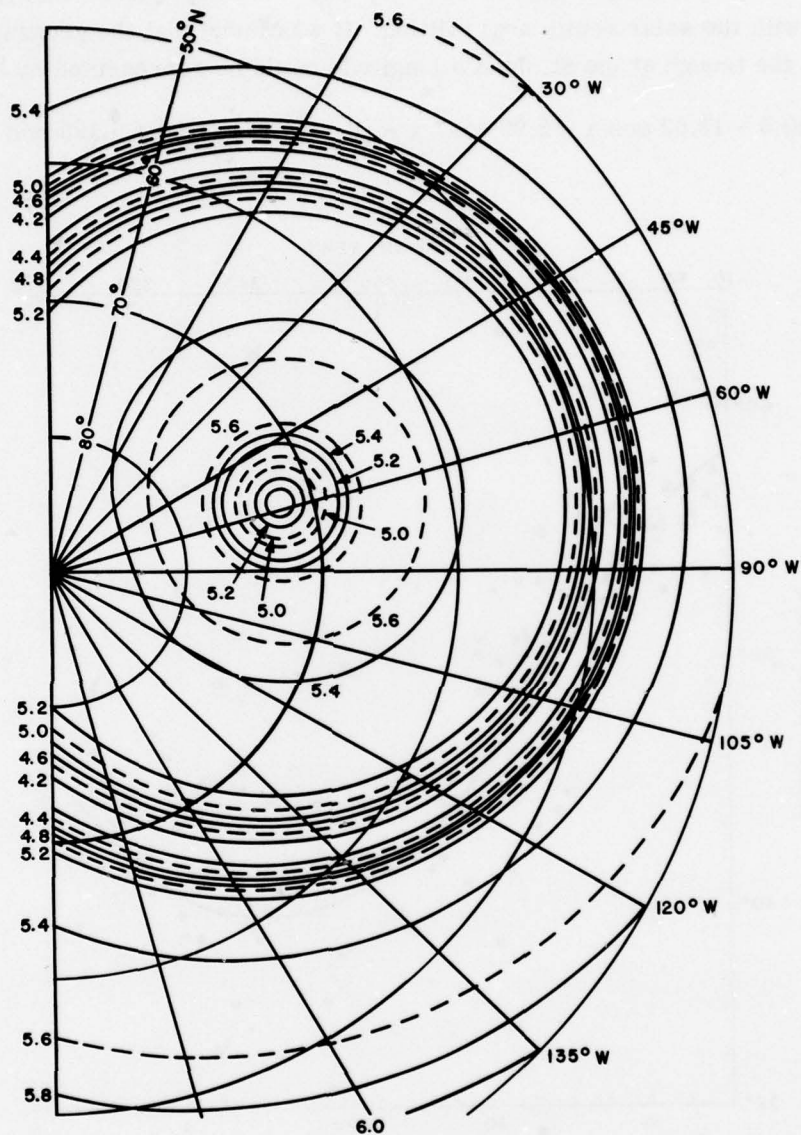
Figure 2-2. Contour Plot In Geographic Coordinates of the
Common Logarithm of the Electron Density (EL/CM^3)
of the F2-Layer Peak at 18:00 Local Time on
December 17 for K_p = 5- Over the Western
Hemisphere As Predicted by the Model

motion of the trough cannot be separated from seasonal motion, and a single parameter must be used. The solar zenith angle was chosen for this purpose.

The trough position is also affected by K_p. This dependence was fitted simultaneously with the solar zenith angle fitting. It was found that the geographic colatitude of the trough at the St. John's longitude could be represented by the equation

$$\theta = 40.5 - 13.62 \cos \chi - 2.90 \cos^2 \chi + \left(K_p - 4.67\right) (1.90 + 0.128 \cos 15t) . \tag{2-2}$$
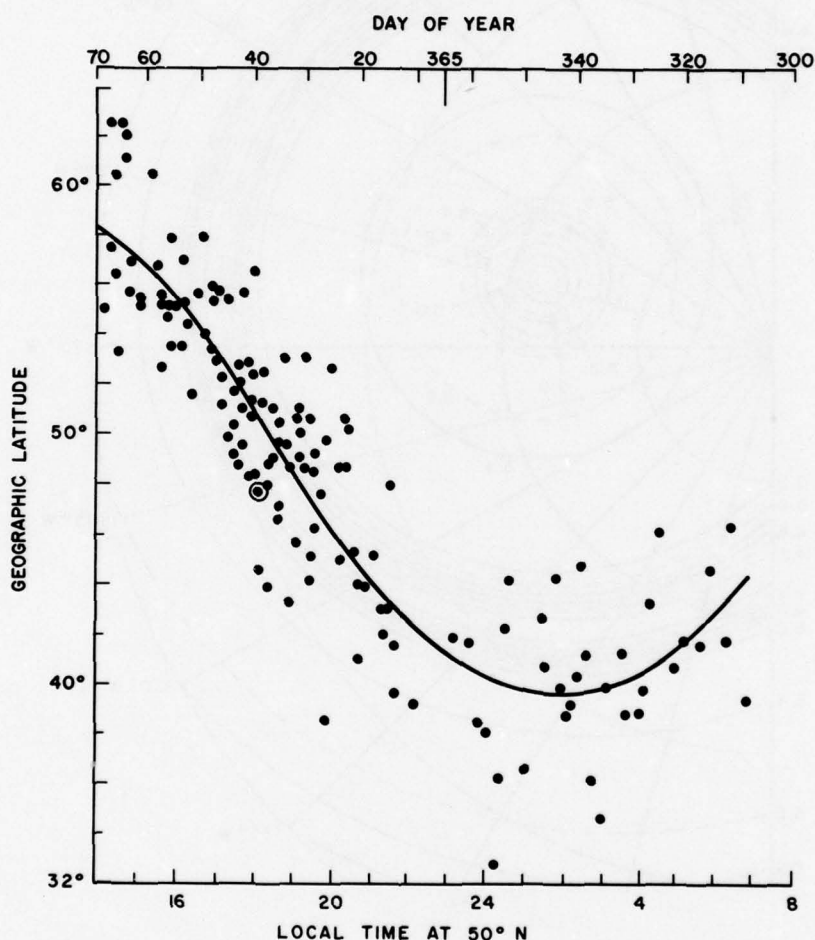
The plotted points are the observed latitudes regressed to $K_p = 5-$. The circled point denotes the trough latitude during the night of October 24, 1962.

Figure 2-3. The Model Fit to the Latitude of the Center of the Main Trough at the St. John's Newfoundland Meridian

2-6

Here t = local time - 2.13 hours, θ is the colatitude in degrees, K_p is the daily mean magnetic activity index, and χ is the solar zenith angle evaluated at time t.

It may be observed from Equation (2-1) that the trough latitude reaches its maximum and minimum values approximately two hours after local noon and midnight respectively. This is in agreement with the experience of the ground-based station at Ottawa. The trough moves an average of 1.9 degrees south per unit increase in K_p. This figure agrees well with the generally accepted value of 2 degrees per unit K_p. The sensitivity of the trough location to K_p was permitted to vary over the day, but this effect was found to be minor. When all the data is regressed to K_p = 5-, a scatter of between 1 and 2 degrees (probable error) is observed (see Figure 2-3).

In order to fit the spatial dependence deduced from the October 24-25 data, an adjustment is required because the trough location over St. John's longitude on that day as expected did not correspond precisely to the average value as given by Equation (2-2). This particular discrepancy happened to be an atypically large 3.9 degrees. (The circled point at 18:00 in Figure 2-3 is the trough location for the path nearest St. John's on the night of October 24-25.) The trough is moved north by this amount from its actual position on October 24-25, destroying the agreement with the data on the given day, but yielding a much more typical location.

One possible source of error is that the trace scaled on a given ionogram need not be vertical as has been assumed here. In the case of Alouette I, a trace due to an oblique ray propagating at an angle of 20 degrees from the vertical would misplace the trough by about two degrees in latitude. To the extent that this effect is random it is largely compensated by the averaging described in the previous paragraph. However, it is plausible that the effect is partially systematic and therefore not fully compensated.

Plots of the location of the trough for the first of each month at 71.49°W longitude (Millstone Hill) are given in Appendix A.

In terms of model colatitude θ_m (and longitude λ_m with respect to which the model is invariant), the F2 peak electron number density N_e is given by

$$\log_{10} N_e \left(\theta_m\right) = B_1 + B_2\theta_m + B_3\theta_m^2 - \Sigma_1^4 F_i A_i \exp\left[- G_i \left(\frac{\theta_m - \theta_i}{H_i}\right)^2\right]. \qquad (2\text{-}3)$$

The coefficients B_i, A_i, θ_i, H_i, are given in Table 2-1. The functions F_i and G_i in general depend on K_p and local time as well as day of year. At the present stage of the model, $F_1 = G_1 = 4.67/K_p$; all other F_i and G_i are set to 1. The assignments for F_i and G_i are not expected to be particularly accurate for K_p

significantly different from 4.67 (i.e., 5-). In addition, the F_i, G_i and B_i are likely to depend on the local time or zenith angle, but the present data does not give a quantitative picture.

Given a feature of the ionosphere in terms of its model coordinates (θ_m, λ_m), and consequently the corresponding density $N_e(\theta_m)$, its location in geographic co-ordinates (θ, λ) can be found as follows. Transform to an intermediate coordinate system (θ', λ_m) in which the curves of constant θ' are circles, using Equation (2-1) inverted,

$$\theta' = \frac{\theta_m}{1 - d \cos 2\lambda_m} \quad . \tag{2-1'}$$

The value of d is listed in Table 2-1. Then, a standard rotation from one set of spherical coordinates to another gives the geographic coordinates (θ, λ) by:

$$\cos \theta = \cos \theta_o \cos \theta_m - \sin \theta_o \sin \theta_m \cos \lambda_m \tag{2-4}$$

Table 2-1

NUMERICAL VALUES OF MODEL PARAMETERS*

A. Indexed Quantities

	B_i	A_i	θ_i	H_i	Δ_i	ε_i
i=1	5.6989	1.223	0.4242	0.0436	0.23774	0.03315
2	-2.0314	-0.15	0.474	0.0175	0.05069	0.002241
3	2.6908	-0.20	0.1140	0.0525	—	—
4	—	0.64	0.052	0.0666	—	—

B. Unindexed Quantities

d	0.0109
θ_o	0.30748
λ_o	-1.28091
τ	2.1265

*All angular quantities are given in radians.

$$\sin \left(\lambda - \lambda_o \right) = \frac{\sin \lambda_m \sin \theta_o}{\sin \theta} \qquad (2\text{-}5)$$

Here θ_o and λ_o are the colatitude and longitude respectively of the model north pole in geographic coordinates. The numerical values are given in Table 2-1.

The effect of the solar zenith angle and K_p are now incorporated. First, the rotation angle from local midnight Ψ, the declination δ, and solar zenith angle χ are calculated:

$$\tan \delta = -0.433775 \cos \left[\frac{2\pi}{365.25} \left(\frac{9 + D + T}{24} \right) \right] \qquad (2\text{-}6)$$

$$\Psi = 0.2617993\, T + \lambda \qquad (2\text{-}7)$$

$$\cos \chi = \cos \theta \sin \delta - \sin \theta \cos \delta \cos \Psi \; . \qquad (2\text{-}8)$$

In these equations, D is the day of the year and T is the universal time. The above prescription fixes the winter solstice at midnight GMT on December 22, where it was in the late 1960's, and neglects the effect of leap years. All angles are measured in radians.

The location of the model feature is then moved south (geographically) from (θ, λ) to $(\overline{\theta}, \lambda)$ as follows: Define Φ by

$$\Phi = \left(1 - \cos \theta_m \right) \left(1 - \cos \theta_1 \right)^{-1} \left\{ \begin{array}{ll} 1 & \theta_m \leq \theta \\ \cos 2 \left(\theta_m - \theta_1 \right) & \theta_m > \theta_1 \end{array} \right\} \qquad (2\text{-}9)$$

Φ is chosen so that it is 1 at the main trough, decreases rapidly north of the trough, is 0 at the model north pole, and varies slowly south of the trough. Now find $\overline{\theta}$ using

$$\frac{\overline{\theta} - \theta}{\Phi} = \Delta_1 \cos \chi + \Delta_2 \cos^2 \chi + \left(K_p - 4.67 \right) \left\{ \varepsilon_1 + \varepsilon_2 \cos \frac{\pi}{180} \left[15(t - \tau) + \lambda_m \right] \right\} \; .$$

$$\qquad (2\text{-}10)$$

Δ_i, ε_i, and τ are given in Table 2-1. Finally, determine the latitude $\overline{\varphi}$ (in degrees) by

$$\overline{\phi} = 90 - \frac{180\, \overline{\theta}}{\pi} \; . \qquad (2\text{-}11)$$

In applying the model in the reverse direction, merely reverse the above steps except for the practical difficulty that F and χ are not determined until after $\overline{\theta} - \theta$ is known, but are needed to calculate this quantity. This just requires iteration to be resolved. The iteration may be accelerated by noting that χ may be calculated from $\overline{\chi}$, the zenith angle at $(\overline{\theta}, \lambda)$, and χ', the zenith angle at $(\overline{\theta} - \pi/2, \lambda)$ or equivalently at $(\pi/2 - \overline{\theta}, \pi - \lambda)$ by

$$\cos \chi = \cos \overline{\chi} \cos (\overline{\theta} - \theta) - \cos \chi' \sin (\overline{\theta} - \theta) \ . \tag{2-12}$$

Then Equation (2-10) may be solved by defining

$$Y(\theta) = \frac{\theta - \theta + \Delta_1 \cos \chi + \Delta_2 \cos^2 \chi + \left(K_p - 4.67\right)}{F} \left\{ \varepsilon_1 + \varepsilon_2 \cos \frac{\pi}{180} \left[15(t - \tau) + \lambda_m \right] \right\} \tag{2-13}$$

and solving Equation (2-13) for the value of θ which causes Y to vanish by, for instance, the secant method. Note, however, that Φ depends on θ_m and therefore on θ. Consequently, Φ must be recalculated at each step.

2.1.5 Comparison of model derived trough locations with other sources. In order to verify that the data used were representative of the densities which might be expected under the conditions (time, date, K_p) for which they were taken, it is useful to check the model against sources which were not used in constructing the model. Such a check also helps to determine the validity of the fitting procedures used. A model of the density at the F2 peak during a time period from 14:00 LMT on December 16, 1971, to 18:00 LMT on the following day had been prepared by Evans et al. [1972] for a longitude of 71.49°W (from satellite tracking data). Because this model is simply a two-dimensional Fourier fit to the observed data, it is expected to be representative of the actual densities observed on a particular day. The densities are markedly smoothed by the twin factors of the experimental technique used, which measures total content (not critical frequency) directly, and the fact that a limited number of terms were used in the Fourier fitting.

The comparison of the two models is given in Figure 2-4, which also indicates data from other sources regressed to 71.49°W Longitude and 300 km where necessary by following L-shells. Also see Table 2-2.

Comparison of the present model with the disturbed day model of Evans [1972] shows general agreement to within one degree. However, at 12:00 LMT and from 20:00 to 22:00 on December 16 (not illustrated), there is agreement only if the value of K_p for the previous three-hour period used. Without this adjustment there is a discrepancy of five degrees. The agreement with the ISIS satellite data is good, with a three degree difference at one of the points and perfect agreement at the other. The Thomas and Andrews [1968] regression equations give fair agreement with discrepancies averaging about two to three degrees at $K_p = 0$. However, these regression equations do not admit a simple summary into one equation, or agree well with the other available sources. Muldrew* has suggested that Thomas and Andrews [1968] may have sometimes confused high-latitude troughs for the main trough.

_____

*Private communication with the author at Communications Research Center, Ottawa, Canada.
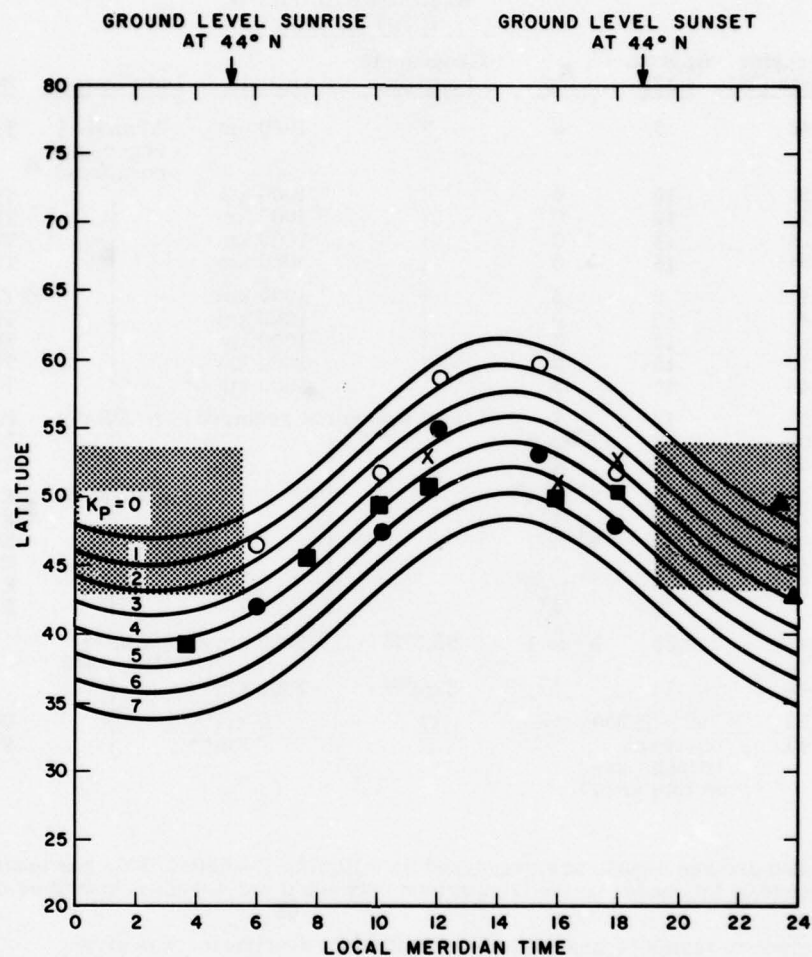
Figure 2-4. Comparison of the Latitude of the Center
of the Main Trough at 7-1/2°W Longitude on
December 17 for Integral Values of K_p as
Predicted by the Model with Data
from Other Sources

Table 2-2

TROUGH LOCATIONS FROM OTHER SOURCES

Figure 2-4 Symbol	Geographic Latitude (°N)	Approx. LMT	K_p	Regressed* to 71.5°W. at 300 km from:		Data Source	Reference
				Geographic Longitude	Altitude		
O	46	6	0	†	1000 km	Alouette I regression equations‡	Thomas
O	51	10	0	†	1000 km		Thomas
O	58	12	0	†	1000 km		Thomas
O	59	15	0	†	1000 km		Thomas
O	51	18	0	†	1000 km		Thomas
●	42	6	3	†	1000 km		Thomas
●	47	10	3	†	1000 km		Thomas
●	55	12	3	†	1000 km		Thomas
●	53	15	3	†	1000 km		Thomas
●	48	18	3	†	1000 km		Thomas
×	54	12	7	regression not required		NAVSAT§	Badura
×	51	16	7^+ to 5^+				Badura
×	52	18	4^+				Badura
■	39	4	3^+ to 4^+			D-NC Model	Evans
■	46	8	4^+				Evans
■	49	10	4^+ to 7				Evans
■	51	12	7				Evans
■	50	16	7^+ to 5^+				Evans
		18	4^+				Evans
△	49	23	2^+ to 1	65.3°W	~3000 km	ISIS-1 Dec 1969	¶
△	46	24	3^-	62.0°W	~3000 km		¶
▓	54	"90% of 200 observed troughs are in this area"		†	0 km**		Van Zandt
	43			†	0 km**		Van Zandt

*All data which require regression are regressed by following L-shells. This has been done to avoid any influence of the model on the comparison between it and the data described in this table.

†This data was given in terms of L-shells. No longitudinal dependence was given.

‡For each time sector a separate regression equation was used. No attempt to maintain continuity from one time sector to another was apparent.

§The data from the SATSUM plots contains a fitting parameter which was not necessarily set optimally. For many of the plots, the trough was not distinguishable from other features because of this. For the data points used, the trough center may be slightly incorrect for the same reason. In the disturbed non-cyclic model [Evans, 1972] the fitting parameter was optimized for each datum; however, the fitting functions do not go through every data point.

¶Private communication with P. Wildman.

**The altitude used for the regression of this data was the one for which the invariant latitude and L-shells listed by the authors agreed.

The agreement of the latitude prediction of the present model with the statistics of Van Zandt and Lund [1967] is complete if the fact that the trough is further to the north during all other months than it is in December is taken into consideration (see Appendix A).

2.1.6 Discussion and conclusions. The model described in this document appears to give a reasonably accurate description of the F2 peak electron density over wide geographic and seasonal limits if the local time and K_p value are kept within narrow limits. In addition, the trough location is well described over the full range of local times and at least $1 \leq K_p < 6$. The present model shows the F2 peak with its dominant structural features within these limits. Previous models either average the structure out of existence or apply only under extremely limited conditions.

The present model can be improved in several ways. For instance, the local time and K_p restrictions should be relaxed. However, this requires a much larger data base. A larger data base brings with it the possibility of losing the structure as already emphasized. The best way of avoiding this possibility might not be to average densities directly but rather to average trough locations, widths and depths, the number of high-latitude ridges and troughs, etc.

There is more residual error in Figure 2-4 than is desirable. This might be reduced by using three hourly values of K_p rather than the daily values available for the data used here. It is also likely that the inclusion of other parameters such as the Zurich sunspot number would help significantly.

2.2 Fitting Electron Density Profiles

2.2.1 Approach. An ideal empirical ionospheric model should include data obtained from both topside and ground-based ionosondes, since the data available from these two sources complement each other. Both types of ionosonde are capable of giving the F2 peak electron density, but ground-based ionosondes give good temporal resolution and poor spatial resolution, while the reverse is true for a topside sounder. What is not so clear, however, is how best to merge data obtained from the two sources.

The simplest procedure for using topside and bottomside data together is to:

A. Model the peak density by regarding both sets of data as equivalent,
B. Model the height of the peak and a scale height at the peak altitude from the ground based data only, and
C. Model the scale height of the topside from the topside sounder only.

This approach, however, founders on the fact that two disjoint models have been created and there is no natural way to join them. The bottomside data stops an unknown distance averaging about five km below the F2 peak (as the data is stored

2-13

by the World Data Center, Boulder, Colorado), while data from the topside stops an unknown distance above the F2 peak averaging about 20 km for the oldest Alouette I data (better for later Alouette I and all Alouette II data). Any error in estimating this height difference produces an error in the total content which is closely approximated by the product of the maximum density and the height error. It should be recalled that total content is one of the parameters which affect radar refraction most strongly. If smoothness is required in fitting the two parts of the model together, small errors in extrapolating the bottomside (or the topside) data can cause substantial errors in the estimation of the above-mentioned height difference.

Aid in improving on this undesirable result is provided by the incoherent backscatter radar. Studies of the data obtained from the Millstone Hill radar facility have shown that the F2 layer is reasonably well approximated by a constant scale height Chapman shape (Figure 2-5), and can be excellently represented by a Chapman shape with a suitably chosen scale-height variation Badura,[1971]. Visual examination of data obtained at the Chatanika radar indicates that the same remarks should hold for the F2 layer over that site, even in the presence of such complex features as the trough and the fat F layers in the auroral region.

With the knowledge of the general shape of the F2 layer thus obtained, it is possible to determine the peak altitude and the scale height at the peak from topside
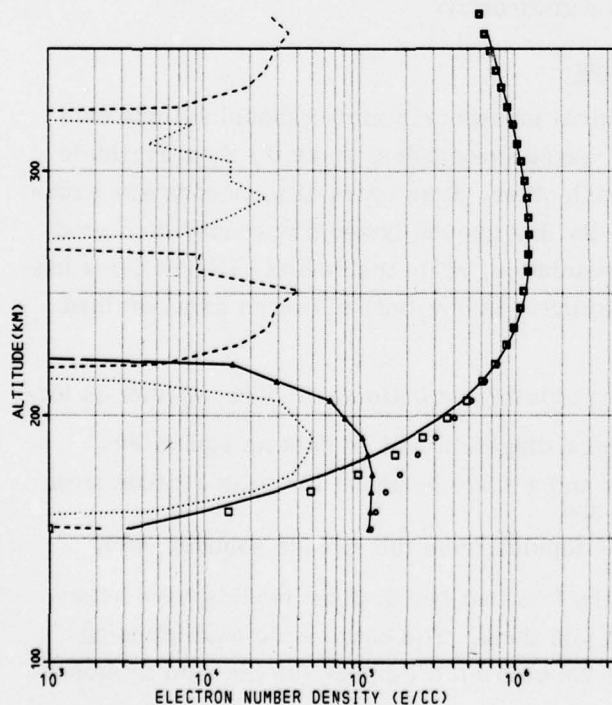
Figure 2-5. Constant Scale-Height Chapman Fit to Millstone Hill Data at 19:46 GMT on January 6

2-14

data. This provides a natural method for assembling a topside and a bottomside profile. The height of the peak may be modeled using the two types of data on an equal footing. Topside data has a larger extrapolation than bottomside data but the shape is simpler (no F1 or E layers are present) and there is no D layer for which the electron content must be estimated. Topside data has been compared with incoherent backscatter radar [Fleury and Taieb, 1971] and in the absence of oblique propagation agrees quite well.

Both topside and bottomside data yield scale heights at the F2 peak and one can either treat the two on an equal footing or permit a discontinuity in the scale height at the F2 peak. Even if the latter choice seems necessary, only the second derivative of electron density with respect to height is discontinuous.

The fitting procedures described in this report are not restricted to topside data in any basic way; they have, in fact, been used on ground-based ionosonde data and incoherent backscatter radar data. However, the assumption is made that a single layer is under examination, which implies that something must be done about F1 and E layers. These layers can be handled by restricting the lowest altitude considered to be well above the F1 peak altitude or by subtracting an approximation to the F1 and E densities from the data before fitting is done: (A subtraction was done in Figure 2-5).

2.2.2 Layer shape. The α-Chapman function yielding the electron density N at altitude h can be written in the following form:

$$N(h) = N_o \exp \frac{1}{2} \left[1 - \frac{h - h_o}{s} - \sec \chi \exp\left(- \frac{h - h_o}{s}\right) \right] \qquad (2\text{-}14)$$

h_o is the height of the peak for a vertical sun, N_o is the maximum density for a vertical sun, χ is the solar zenith angle, and s is the scale height. For any given profile, χ can be eliminated by substituting

$$h_m = h_o + s \ln \sec \chi$$

and

$$N_m = \exp \frac{h_m - h_o}{2s}$$

into Equation (2-14) which yields

$$N(h) = N_m \exp \frac{1}{2} \left[1 - \frac{h - h_m}{s} - \exp\left(- \frac{h - h_m}{s}\right) \right] \quad . \qquad (2\text{-}15)$$

N_m has the significance of the maximum electron density in the profile; h_m has the significance of the altitude at which this density is achieved. Representation

2-15

of a profile in terms of Equation (2-15) has the advantage [with respect to the representation in terms of Equation (2-14)] that no suggestion is implied that values could be found for N_o and h_o which would hold constant over a collection of profiles taken at differing times and locations. Badura [1971] had found that shapes of the form of Equation (2-15) fit incoherent scatter data from two days of data taken at Millstone Hill rather well, and that by replacing s with a polynomial in altitude, a very good representation could be made in all cases. He further found that there was no gain in altering the coefficent of 1/2 in the exponent.

The derivation of the Chapman layer shape can be redone without the assumption of a constant scale height. The form of a variable scale height Chapman layer closest to Equation (15) is:

$$N(h) = N_m \exp \frac{1}{2} \left[1 - z(h) - e^{-z(h)} \right]$$
$$z\left(h_m\right) = 0 \ .$$

(2-16)

The scale height (which in an α-Chapman layer is the same as the neutral scale height) is related to z by

$$\frac{1}{s} = \frac{dz}{dh} \ .$$

(2-17)

It is assumed that the Equation (2-16) for suitable dependence of z on altitude gives the shape of any given electron density profile. Equation (2-17) is maintained as the definition of the scale height. No claim is made that the ion chemistry used in obtaining an α-Chapman layer is valid (indeed, diffusion is more important than recombination on the topside). However, the shape is a useful one and the scale height is usually within about 25 percent of the neutral scale height.

Preliminary studies showed that topside scale heights were better ordered by fitting 1/s than by fitting s, and that (for a few profiles) representing z by a polynomial in altitude permitted better fits than several other functional forms tried. A polynomial has the useful advantage of permitting a linear least squares fitting program to be used, with large cost savings over the use of a general function-maximizing routine. More important however, is the fact that an expansion of the form

$$z = z_0 + a_1h + a_2h^2 + \ldots + a_nh^n$$

(2-18)

permits z to be fit without knowing the value of h_m, but after h_m is calculated using $z(h_m) = 0$, Equation (2-18) may be rewritten exactly as a polynomial in $(h - h_m)$ of the same degree. Since the rewriting is a mathematical identity, any least-squares property possessed by the original fit will be possessed by the new

2-16

polynomial. No new parameters are introduced by the rewriting since the new polynomial must have no constant term. In practice, it was decided to use units of 100 km and to use a polynomial in (h - 3). This choice clarified the relative importance of the coefficients and probably reduces slightly the roundoff errors introduced in rewriting the polynomial into one in $(h - h_m)$.

The degree of the polynomial must be chosen. A linear expansion yields a constant scale height and there is conclusive evidence that the scale height increases with altitude at least on the topside. A quadratic function fits some profiles very well (particularly at night), but others are not well represented. The addition of a cubic term provides the added flexibility to fit these profiles. However, there is of necessity some extrapolation to be done in order to apply the data to the peak region. Therefore, the quadratic expansion should be preferred unless the fit it gives is significantly poorer than the cubic expansion.

By using a stepwise multiple-regression fitting package it is possible to obtain the least-squares quadratic fit and the least-squares cubic fit for each profile. Then, due to the linearity of polynomial fitting in the coefficients, a weighted average can be taken between the two fits. This average fit usually will be a cubic polynomial, but the coefficient of $(h - 3)^3$ will be kept relatively small. Such an average fit need not have any particular residual, but if the residual does not lie between that of the least-squares quadratic and least-squares cubic fits, neither of the latter fits can be trusted to represent the data.

The following algorithm implements the averaging scheme.
Define the average $\bar{z}$ by:

$$z = \frac{1}{n} \sum_{i=1}^{n} z_i \; ,$$

the total variance as:

$$r_0 = \sum_{i=1}^{n} \left(z_i - \bar{z} \right)^2 \; ,$$

the residual variance after fitting a quadratic polynomial as:

$$r_2 = \sum_{i=0}^{n} \left| z_i - \sum_{i=0}^{2} a_i \left(h_i - 3 \right)^i \right|^2 \; ,$$

2-17

and the residual after fitting a cubic polynomial as:

$$r_3 = \sum_{i=0}^{n} \left| z_i - \sum_{i=0}^{3} b_i \left(h_i - 3\right)^i \right|^2 \quad ,$$

where n is the number of points in the profile, the a_i are the coefficients of the quadratic fit and the b_i are the similar coefficients of the cubic fit. Then define

$$\rho = \frac{r_2}{r_3}$$

$$\tau = 100 \, \frac{r_2}{r_0} \cdot \frac{(1 - \rho)^2}{3\rho}$$

and

$$\gamma = \min \, (\tau, 1) \quad .$$

The average polynomial

$$z = \sum_{i=1}^{3} c_i \left(h - h_m\right)^i$$

is given by

$$c_i = \gamma b_i + (1 - \gamma) \, a_i \qquad i = 1, \, ..., \, 3 \quad .$$

This algorithm was chosen simply because, on test cases, it caused the program to make the same choices between the quadratic fits and cubic fits as were made by visual inspection of the data when there was a clearcut choice and it produces a smooth transition in the region where it is not clear which fit to use.

Real height profiles are presented in terms of $[N(h), h]$ pairs or some form which may be reduced to this one. A value for the peak density N_m is obtained from the data (by a procedure described below). Then the equation is solved

$$z + e^{-z} + 2 \ln \left[\frac{N}{N_m}\right] - 1 = 0 \qquad (2\text{-}19)$$

for each altitude in the data. Since there are on the order of 20 altitudes per profile and many thousands of profiles in the Alouette I and II data base, an efficient root-finding algorithm is highly desirable. Because the form of the left side of Equation (2-19) is very smooth, the following extension of the Newton-Raphson iteration scheme to use second derivative information works very well. Denote

2-18

the left side of Equation (2-19) at the ith iteration by F_i and its derivatives with respect to altitude by F'_i and F''_i. Then

$$z_{i+1} = z_i - \frac{F_i}{F'_i - \frac{F''_i}{2F'_i}} \, . \tag{20}$$

The asymptotic convergence rate of this scheme is third order. Once the (N, h) data is rewritten into (z, h) data, the fitting of a polynomial in h - 3 to it is a standard multiple linear regression problem. The IBM written package denoted as STEPR in their scientific subroutine package is adequate to fit any single electron-density profile. A small amount of rewriting was desirable, however, to permit the fitting of many profiles in one run and to replace some very expensive transfer of data via disk files with a corresponding transfer in core. It was also necessary to modify the sample output routines to do the averaging, to compute h_m, to recalculate the polynomial coefficients in order to effect a change in variables from (h - 3) to (h - h_m), to check for various error conditions, and to store the output on disk in a form suitable for later analysis.

A description of the determination of N_m remains to be done. When an ionogram trace can be read to its end, a frequency is obtained which is very close to the peak critical frequency (foF2). For Alouette I data (in the older of two formats used to supply this data) the estimate suggested by the group which scaled the ionograms is that 0.01 MHz should be added to the largest observed frequency to get the best estimate of foF2. In processing the data it is possible to estimate the increase from the maximum observed density to N_m for each profile if one assumes a scale height near the peak. Clearly, the estimation procedure will not be accurate, but the adjustment is small and 30 percent accuracy in the adjustment will give about 2 percent accuracy in N_m when N_m is 10^4 electrons/cm^3. For other (almost invariably higher) densities the relative error in N_m is proportional to N_m^{-2}.

Near the F2 peak, one has

$$N \approx N_m \, e^{-1/4 \, z^2} \tag{21}$$

from which it is possible to extract z by differentiation.

$$z = \frac{-2s}{N} \frac{dN}{dh} \, . \tag{22}$$

Bring the exponential in Equation (2-21) to the left side, expand it in a Taylor series neglecting powers above the quadratic, and substitute Equation (2-22) into the result. This gives

2-19

$$N_m = N + \frac{s^2}{N} \left(\frac{dN}{dh}\right)^2 . \tag{2-23}$$

Since the Alouette I data is presented in terms of critical frequencies, the equivalent expression

$$foF2 = F + \frac{2s^2}{F} \left(\frac{dF}{dh}\right)^2 \tag{2-24}$$

is used for them. A 50-km scale height is assumed. To prevent large errors due to noise in the data, the estimate of foF2 must increase by at least 0.003 MHz, but not by more than 0.04 MHz from the largest observed critical frequency. The ionograms are usually scaled close enough to the F2 peak that this estimate is sufficiently reliable. It is often the best available for the older data. (The new data is smoother and the further analysis described below can be applied much more often.)

When the noise in the data is sufficiently small, this estimate can be checked. If noise is neglected and the distance between the lowest two altitudes for which data exists is comparable with or exceeds the distance between the lowest altitude in the data and the F2 peak, the deviation between the least squares fit to the data and the data itself will be much larger at the lowest altitude in the data than at the next lowest one. Consequently, one can assume that the fitting error at the last point is due entirely to an error in the value of N_m. The change in N_m required to move this data point onto the fitted curve is

$$\delta N_m = \frac{1}{2} \bar{z} \delta z N_m$$

where

$$\bar{z} = \frac{1}{2} \left(z_{fit} + z_{data}\right) \tag{2-25}$$

and

$$\delta z = z_{fit} - z_{data} .$$

Then a second pass through the fitting routines will give a new fitted curve corresponding to the more accurate value for N_m. The process may be iterated, but in the presence of noise, one correction is the most that can be trusted.

In the presence of noise, matters become more heuristic, the maximum improvement possible becomes less, and the possibility of worsening the estimate of N_m occurs. The clearest effect of noise is that one cannot assume that the error in the lowest data point is entirely due to errors in N_m. The remedy is to reduce the error in the last point to the rms noise level (maintaining the sign of the error). It is also clear that an error not much above the noise level need not be due at all

2-20

to an error in N_m. The modification required by this effect is not clear a priori, but trial runs suggest that the error should not be attributed to N_m unless it is at least three times the rms fitting error. Further, it was decided that for relatively noisy data it should be harder to attribute errors to N_m. Consequently, when the rms fitting error in z exceeds 0.07 (about double the average rms actually obtained in production runs) no adjustment of N_m is allowed. When the adjustment in N_m exceeds 2.5 percent is is felt that the distance through which the fit must be extrapolated is too large to be trusted and the profile is rejected.

2.2.3 Speed, accuracy, and robustness of the fitting procedure. Several questions arise with respect to any fitting procedures. These are:

1. With idealized noise-free data of the type anticipated, can the fitting procedure duplicate the data?
2. Does the idealized data correspond to real data?
3. How much accuracy is lost when noise is present?
4. If any assumptions are made about the data which are not checked, how sensitive is the fit to these assumptions?
5. How fast can fits be made?

Various tests were made to answer these questions. Question 2 was largely answered in the affirmative by the work of Badura [1971]. However, it was further checked by fitting data abstracted from the topside of Millstone Hill incoherent backscatter data using the actual value of N_m for the peak density. The portion of the backscatter data above N_m + 60 km was smoothed before the data was made available. Very good duplication of the data was possible despite an extrapolation distance much greater than would be needed in practice (see Figures 2-5 and 2-6). Questions 1 and 3 were addressed with idealized data. Noise was introduced by means of a random number generator for which the output was rescaled to be a Gaussian random variable with specified standard deviation. The noise was specified as either a correlated noise perturbing the critical frequencies or an uncorrelated noise perturbing the altitudes. Correlation was achieved by setting

$$\overline{F}_{i+1} = F_{i+1} + \overline{F}_i - F_i + G_i \qquad (2\text{-}26)$$

where F_j denotes an unperturbed frequency, $\overline{F}_j$ denotes the corresponding perturbed frequency, and G_i denotes the perturbing random variable. Note that the correlation makes the total perturbation grow as $\sqrt{i}$. The detailed tests are tabulated in Appendix B. In these tests, the second iteration correction to N_m was not done and a fixed correction was made to the largest critical frequency to get foF2. The test results are therefore somewhat pessimistic. It was found that with zero noise, the assumed polynomial could be duplicated exactly. In the presence of noise, the important layer parameters were perturbed, but by relatively small amounts.
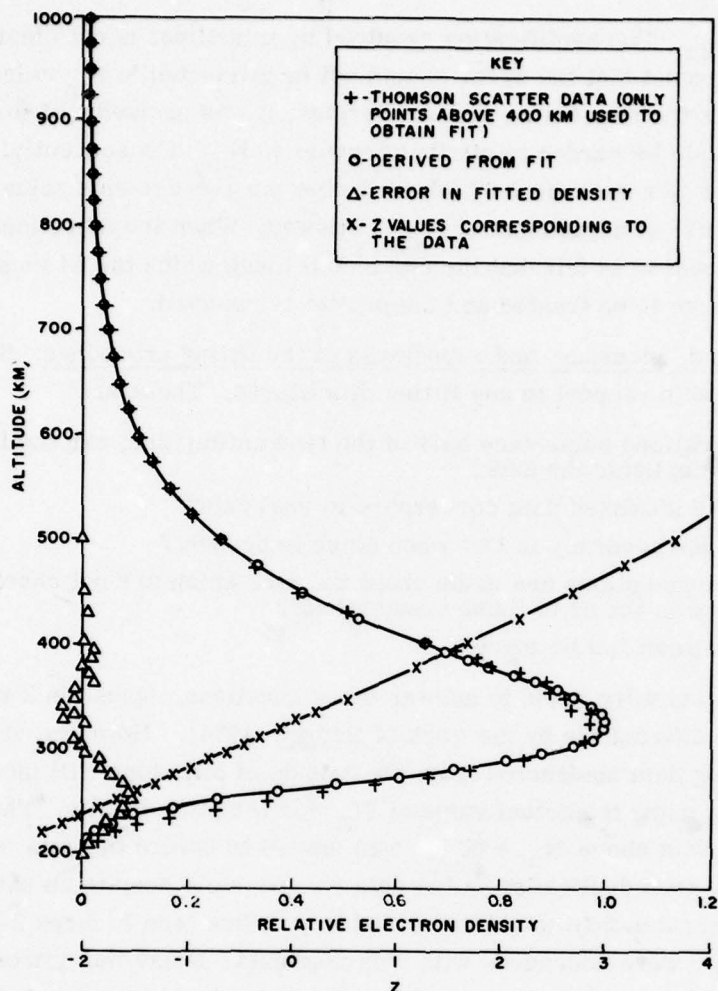
Figure 2-6. Variable Scale-Height Fit to Millstone Hill
Thomson Scatter Data for March 24 at 4:00 EST

The initial choice of scale height affects the initial estimate of N_m. If the data is too noisy, no second-pass correction of this estimate can be made. Even if a correction is made, the correction process is not iterated to completion. A set of profiles was analyzed with assumed scale height of $50/\sqrt{2}$ km and compared with a corresponding run assuming 50 km for the scale height. The typical case is that no change in the fit occurs at all. Small changes are occasionally observed.

It was found that the first 100 profiles of Volume I of the Alouette I data were fitted in two seconds (with a second iteration when suitable). The production runs were consistent with the above figure.

In order to see how the present linearized fitting technique might compare with other nonlinear techniques, a comparison was done with the fitting program used on the Millstone data by Badura [1971]. The program was slightly modified to fit the same functional form as the present analysis uses. N_m was fit as an independent variable on the same footing as the polynomial coefficients and the mean square electron density error was minimized. This procedure avoids the most suspect part of the linearization process. The results are tabulated in Appendix C. Depending on the degree of the polynomial being fitted, the nonlinear fitting process took from 30 to over 200 times as long to fit a profile. Further, only least-squares fits were obtained; the comparison (and averaging) of the quadratic and cubic fits was not done. There are faster function minimization routines now available than were present in the deck used, but it is unlikely that a factor of improvement as high as five could be achieved by changing to one of these routines.

Even worse, however, is the fact that, occasionally, modest amounts of noise produced huge errors in some of the layer parameters (particularly h_m and s). This did not occur frequently (and would never occur when the program is used for incoherent backscatter data as originally intended) but the linearized fitter never succumbed to this problem even with more noise in the data than provoked the above-mentioned problem. After eliminating the fits which are clearly bad (in the sense that the F2 peak is at an altitude never observed in nature) there are a moderate number of very erroneous fits obtained which are nevertheless plausible F2 layer profiles and would not be eliminated in the processing of real data. These fits produce errors sufficiently serious that the nonlinear fitter performed noticeably worse in terms of rms errors in h_m, s_m, and N_m than did the linear fitter.

The increased sensitivity to noise is believed to be due to the fact that only the altitudes near the F2 peak (about half a dozen points) contribute strongly to the residual. There are simply too many parameters to be determined accurately by these few points. A logarithmic transformation would remedy this defect, but the fitting algorithm would then be very similar to the linearized one actually used.

2.3 Alouette I Scatter Plots

2.3.1 Overview of the data. The data from the first four volumes of Alouette I data tapes were plotted. The data was sorted into six local time bins, four season bins, and four bins of K_p. Only data from latitudes north of 30°N, from longitudes between 50°W and 150°W, and with daily Zurich sunspot numbers R_z less than or equal to 50 were plotted.

The following layer parameters were plotted vs latitude: Peak electron density N_m, altitude of the F2 peak h_m, scale height of the F2 peak s_m, rate of

2-23

change of scale height at the F2 peak s_m, an approximation, $N_m s_m$, to the total columnar electron content and the scale height at 300 km above the F2 peak (see Figure 2-7). Note that, by the shape assumed for the layer (see previous section), the relation

$$s(h) = s_m + \dot{s}_m \left(h - h_m \right)$$

is valid only over a limited height range. Plots were also made of the solar zenith angle and R_z in order that the actual scatter in these quantities could be assessed, rather than forcing a need to assume that the full R_z and local time bins were filled.

Geographic coordinates are not suitable for observing fine scale latitudinal dependences unless the longitudinal spread in the data for a given plot is small. However, the local time for a given latitude varies only due to the precession of the satellite's orbit. Consequently, the local time restrictions also impose longitude restrictions. Some ionospheric structure is apparent even in the preliminary survey.

The most striking feature of this set of plots is that the smallest amount of scatter occurs in the scale-height gradient. For all latitudes south of the trough (as defined by the model of Section 2.2), $\dot{s}_m$ is very close to 0.1 km/km [Figure 2-7(D)]. Also very striking is the increase in scale height going north until roughly 70°N, followed sometimes by a less clear decrease [Figures 2-7(C) and 2-8(A)]. The trough is visible in the nighttime fall and winter bins [Figure 2-9(A)].

The depth (a factor of 8 to 10 in N_m) near midnight is noteworthy as is the sharpness of the walls at low K_p and the width ($\geq 10°$), especially considering the fact that any smearing of the latitude of the center of the trough due to the drift of geographic parallels across magnetic shells (as longitude varies) will decrease the width, decrease the slope of the walls, and decrease the depth. To anticipate a result found later while examining the trough, it happened that the satellite passes which provided the data spanned a relatively small longitude range (despite the fact that the data base spans a period of four years). Also, the longitudes were near 70°W where magnetic shells are nearly parallel to curves of constant geographic latitude. The trough was not visible in any of the bins with a local time from 16 to 20 although there often is a trough at dusk.

The auroral oval is not revealed as a striking feature in any of the lower K_p range plots, except for the auroral influence on the north trough wall [Bates et al., 1973]. However, the oval can be noticed by comparing the behavior of more than one parameter. In the region of the noontime auroral oval (about 60 to 65 degrees for the longitudes in this data) there are peak densities similar to those to the immediate south [Figure 2-7(A)]. Just north of the auroral region, N_m begins a strong

2-24
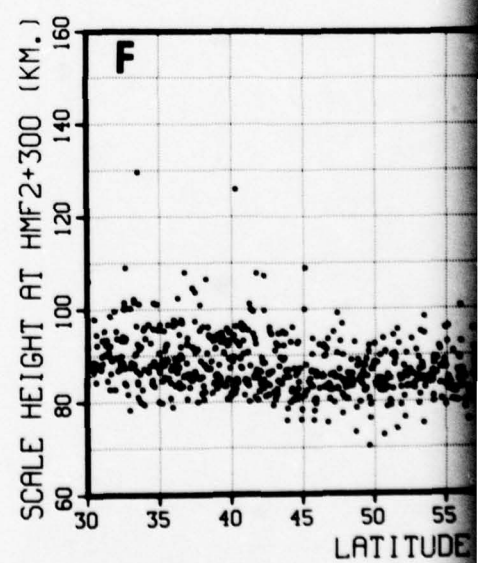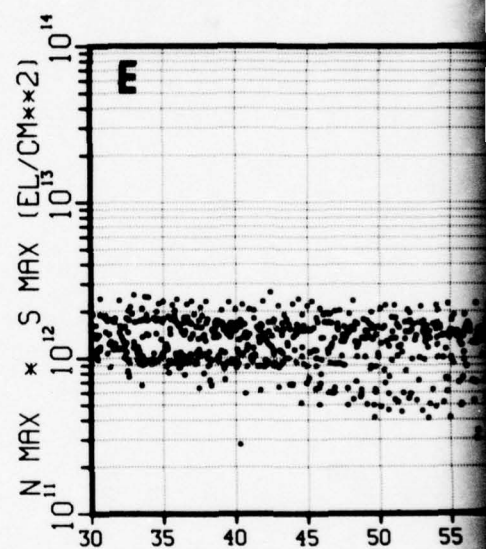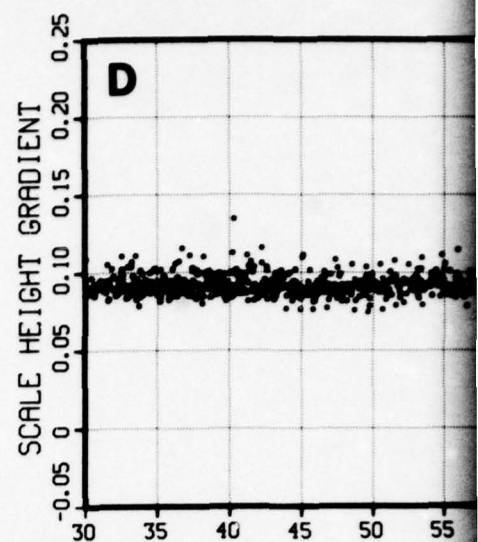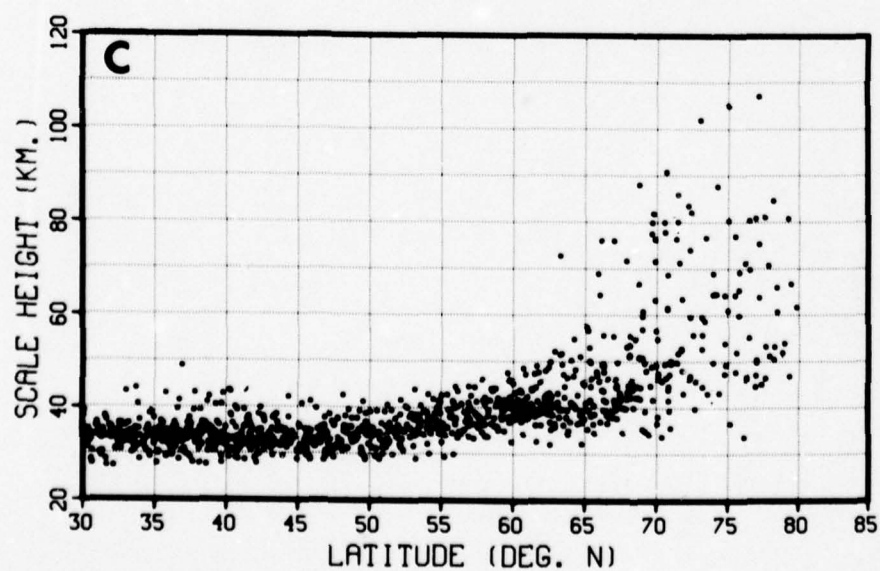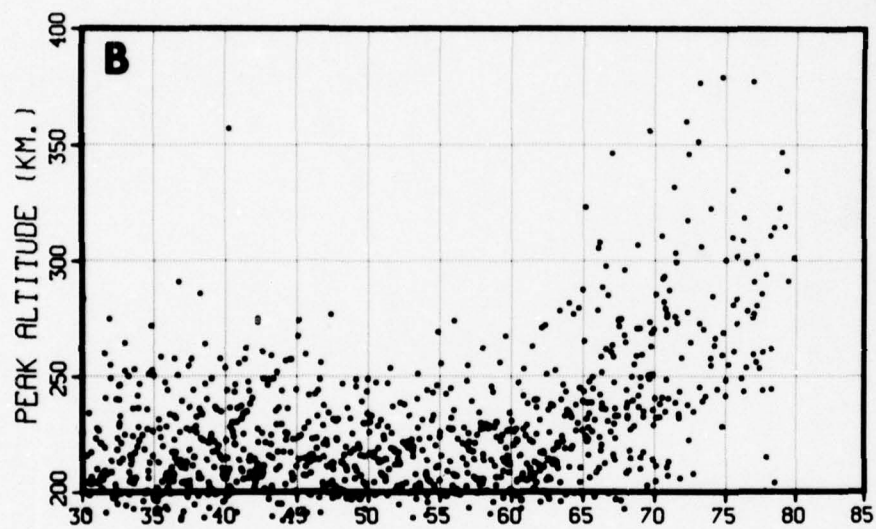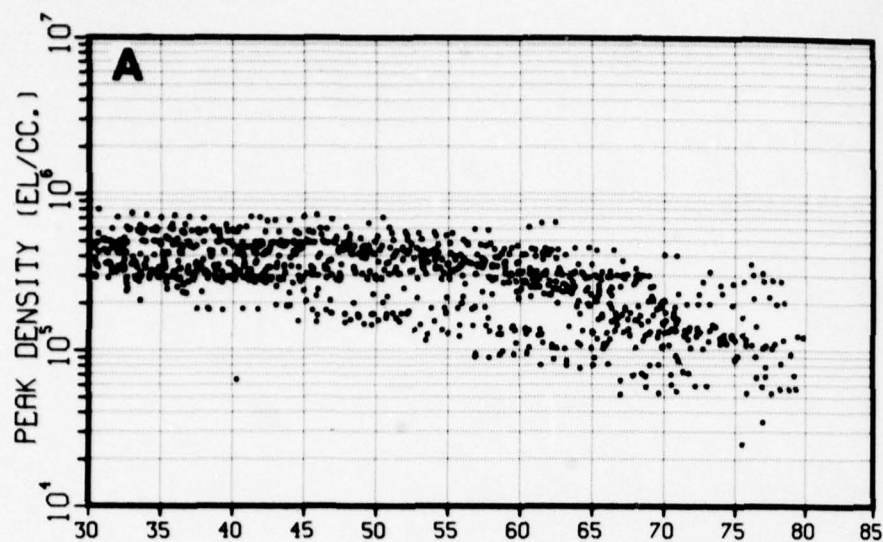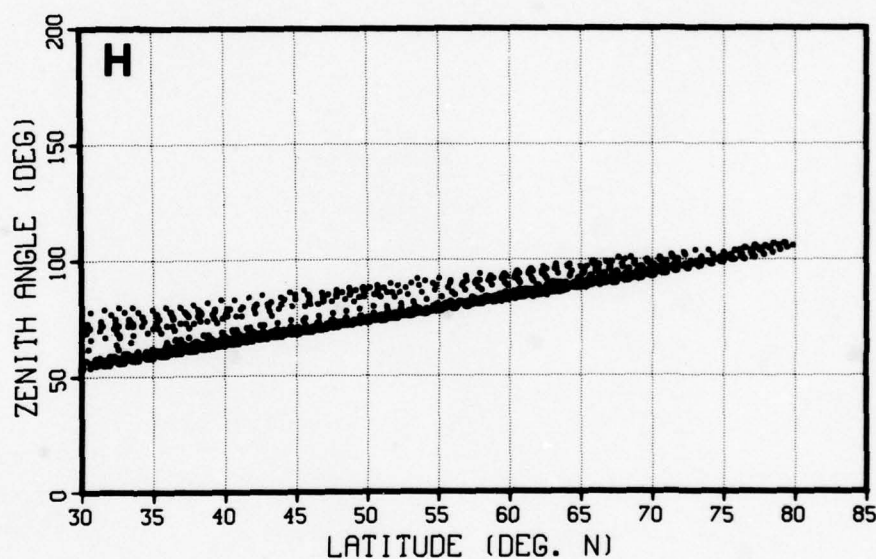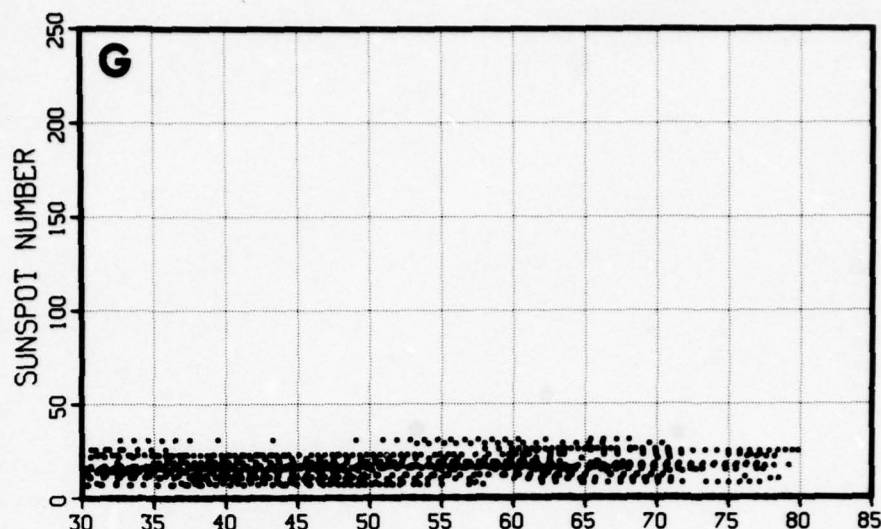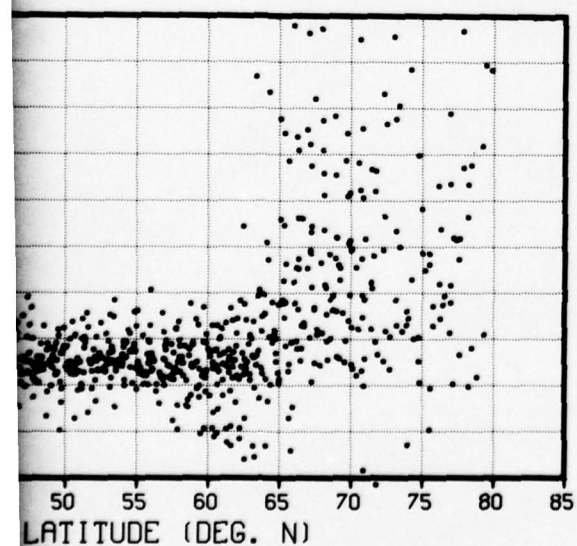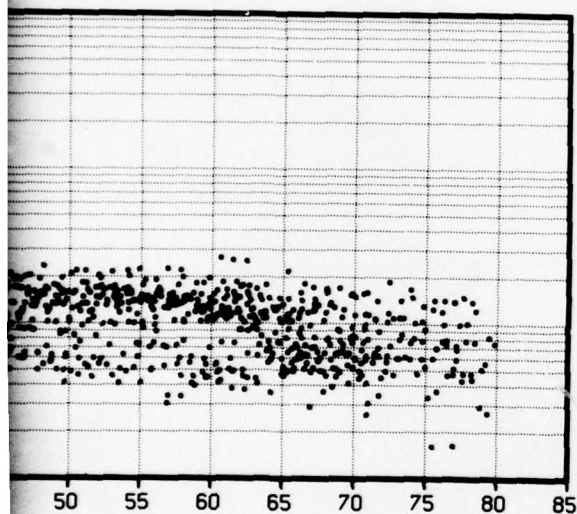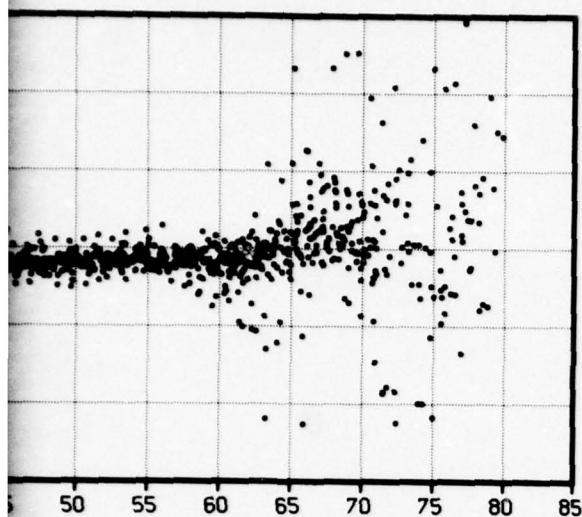
	Date	LMT	K_p	R_z	Longitude
Minimum	12/1	08:00	0	0	50°W
Maximum	2/28	12:00	20	50	150°W

A. Peak Density

B. Peak Altitude

C. Scale Height at the F2 Peak

D. Scale Height Gradient at the F2 Peak

E. Product of the Peak Density and Scale Height

F. Scale Height at 300 km Above the F2 Peak

G. Sunspot Number

H. Zenith Angle

Figure 2-7. Scatter Plots of Fits to Alouette I Data,
12/1 to 2/28, 08:00 to 12:00 LMT
(924 points are plotted)

2-25
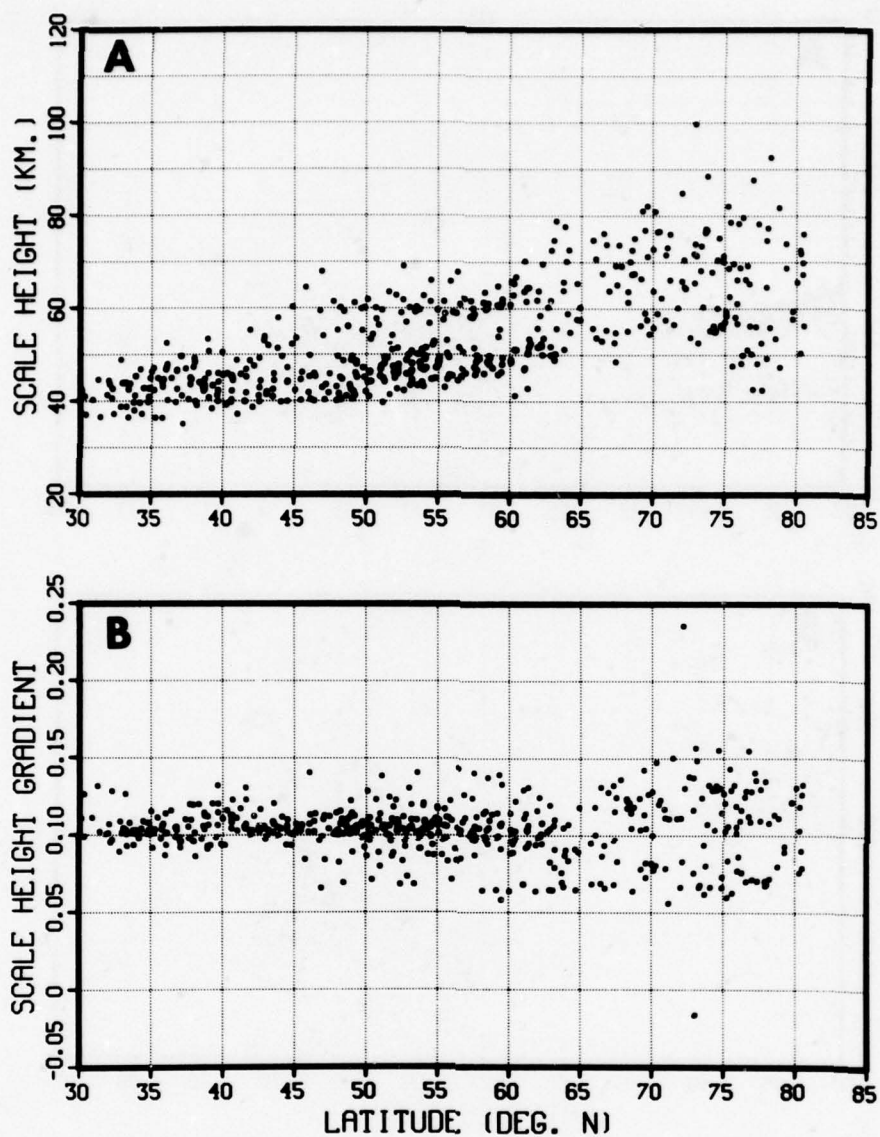
	Date	LMT	K_p	R_z	Longitude
Minimum	3/1	08:00	0	0	50°W
Maximum	5/31	12:00	20	50	150°W

A. Scale Height at the F2 Peak

B. Scale Height Gradient at the F2 Peak

Figure 2-8. Scatter Plots of Fits to Alouette I Data,
3/1 to 5/31, 08:00 to 12:00 LMT
(510 points are plotted)

2-27
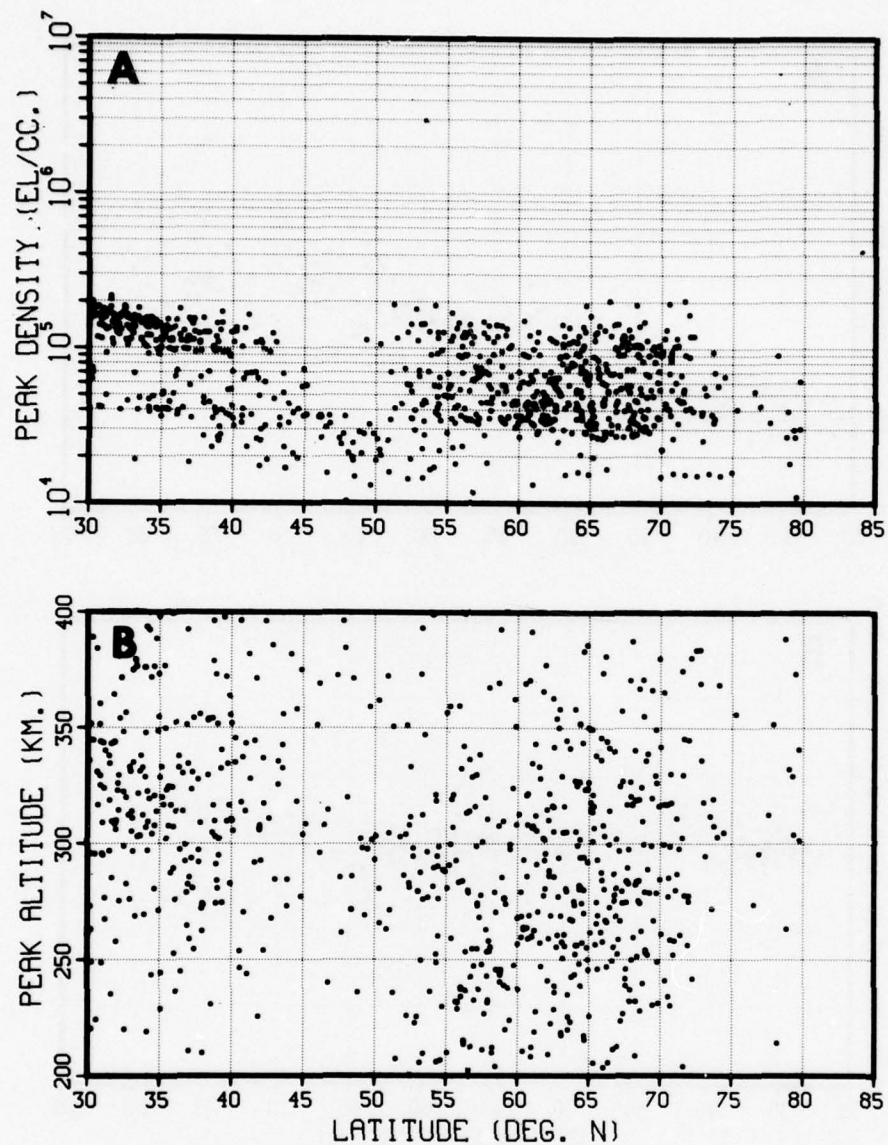
	Date	LMT	K_p	R_z	Longitude
Minimum	12/1	00:00	0	0	50°W
Maximum	2/28	04:00	20	50	150°W

A. Peak Density

B. Peak Altitude

Figure 2-9. Scatter Plots of Fits to Alouette I Data,
12/1 to 2/28, 00:00 to 04:00 LMT
(779 points are plotted)

decrease. The scale height at the peak and 300 km above it begins a marked increase just south of the oval region [Figure 2-7(C) and (F)]. The decrease in N_m in the oval region is essentially balanced by the increase in S_m, leaving the product nearly constant [Figure 2-7(E)]. A density plot for some topside altitude should show a peak.

The effect of increasing magnetic activity is relatively difficult to assess due to the extreme decrease in the volume of available data with increasing K_p. Except for a few features of the trough — deferred to the next section — and the auroral oval, little fine structure can be deduced directly from the scatter plots. Figure 2-10 shows one of the more populous high K_p bins. Figure 2-11 shows the best populated bin in the highest K_p range. The auroral oval is clearer as K_p increases. In the $K_p > 60$ bin it is visible as the region of 100 km scale height from 55 to 60 degrees. In the $37 \leq K_p \leq 57$ bin, it appears as the region of 60 to 70 km scale heights at the peak from about 58 to 63 degrees (one point at 100 kms at 65 degrees), and as the region of 100 to 170 km topside scale height in the latitude region. Rather surprisingly, the extreme K_p auroral region topside scale heights are smaller; they are not much greater than the trough region topside scale heights and comparable with the polar cap scale heights [Figure 2-11(F)].

2.3.2 <u>Trough region.</u> A program was written to locate possible troughs. In contrast to the approach of <u>Tulunay and Sayers</u> [1971], it was considered preferable to include all data which could be part of a trough rather than only data which exhibited a very definite trough. In this manner, it was hoped to see the trough even under conditions for which it is weak. It was anticipated that the proportion of these troughs would be high enough that a consistant picture of the trough could be established and the spurious structures eliminated after a comparison with this picture.

The algorithm used to detect possible troughs is outlined as follows:

A. Eliminate any satellite pass that does not contain consecutive peak densities (N_m) which differ by at least 15 percent.
B. Scan passes from south to north.
C. Examine a 21-point (21 degrees barring missing data points) region around the density jump unless the end of a pass truncates the region. If the N_m change is a decrease, the southern edge of the trough is five points south of the decrease, otherwise it is 15 points south of the increase.
D. Considering N_m changes of eight percent or less between consecutive points as noise, move the southern edge north as long as N_m does not decrease more than noise would permit.
E. Locate the point which ends the region of strong, steady decrease. This is the southern edge of the trough bottom.
F. Locate a point at the end of the region of non-increase in N_m north of the southern edge of the trough bottom. This is the northern edge of the

trough bottom. For some satellite passes the trough bottom may be a sharp valley. In this case the northern and southern walls coincide.

G. Locate a region of non-increase in N_m north of the trough bottom. The most northerly point south of this region is the northern boundary of the trough region.

H. Compare the latitude of the center of the trough bottom with an approximation (for speed) to the model of Section 2.1. Accept the possible trough as real if the discrepancy is less than ten degrees.

I. If there are several possible observations of the trough from a given pass, keep only the southernmost acceptable one.

The algorithm, which is more compact in its actual code than the above description, usually gives reasonable-looking trough cross sections. It sometimes depicts single gradients which appear to be one of the trough walls, with the data truncated by the end of a pass or a sufficiently-large gap in the data that it is considered an end of a pass. Dips not much larger than the assumed eight percent noise threshold also appear. These are probably spurious.

The data obtained by the algorithm described above was plotted in a format similar to the one used for the scatter plots described in Section 2.3.1. The present series, however, is plotted in centered-dipole (geomagnetic) coordinates. The longitude bin was necessarily changed; it now covers the range from 100°W to 20°E (dipole). Individual profiles are plotted with an alphabetic character which changes from pass to pass. The sunspot numbers are now plotted as a one-dimensional set of line segments on the zenith angle plot and a plot of the longitudes actually occurring is produced. The data on the latter plots are given by labeled curves. For each satellite pass the same letter is used in all plots in the set.

Several interesting features are revealed. In the nighttime fall and winter bins (20 to 24 and 0 to 4 hrs) the trough is revealed very clearly, although there is little improvement over the geographic scatter plots (Figures 2-12 and 2-13). The corresponding longitude plots [Figures 2-14(A) and 2-14(E)] clearly explain the phenomenon, as described in Section 2.3.1. The formless scatter of the peak altitude plots [Figure 2-9(B)] is now alleviated [Figure 2-13(B)]. Note the increase in h_m near the equatorward trough wall. The dawn bins show new results. The winter and summer data shows a clear set of troughs (Figure 2-15), but the fall and spring data seem at first to be confused (Figure 2-16). However, study of the zenith angle plots explains the situation (Figure 2-14). In the winter and summer data, at the trough latitudes the solar zenith angle always exceeds 90 degrees (ground-level sunrise). In the fall and spring data, zenith angles of both greater than and less than 90 degrees appear. When the zenith angle is significantly greater than 90 degrees, a wide (10-degree or greater) trough is found and when it is below 90 degrees, no trough is found at low K_p. In the fall moderate K_p bin [Figure 2-16(C) and 2-16(D)],
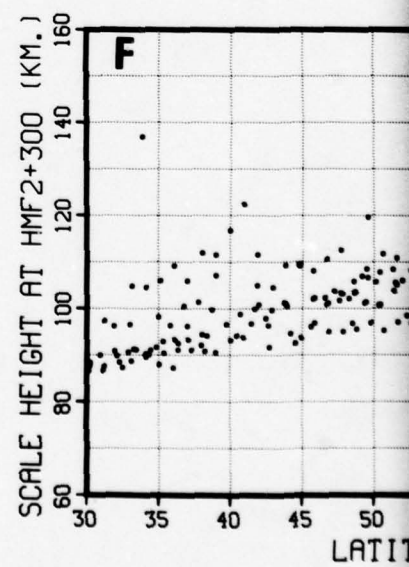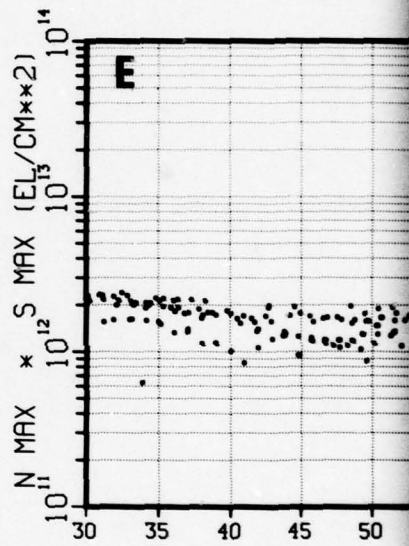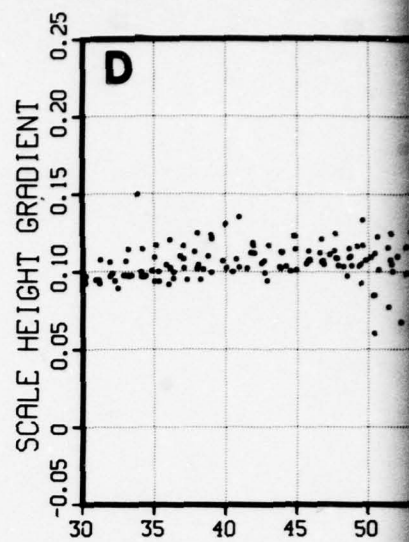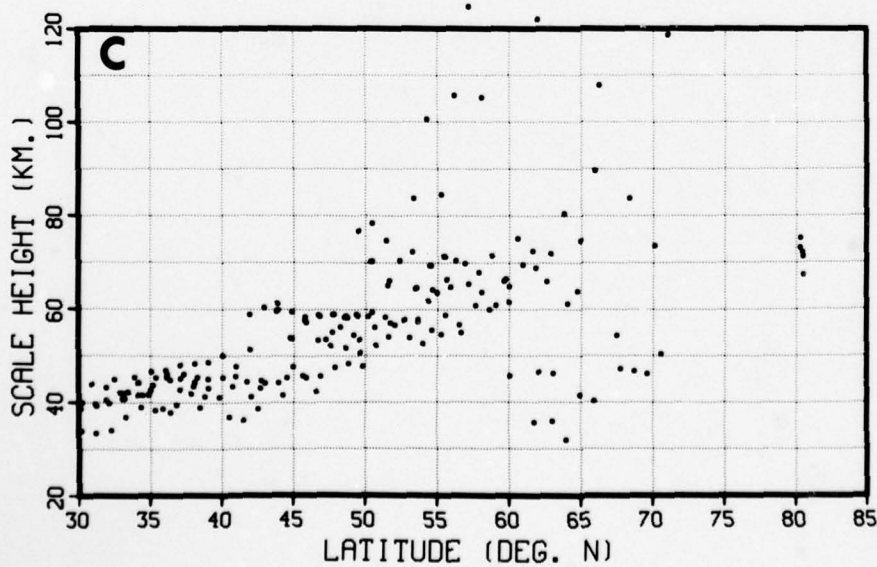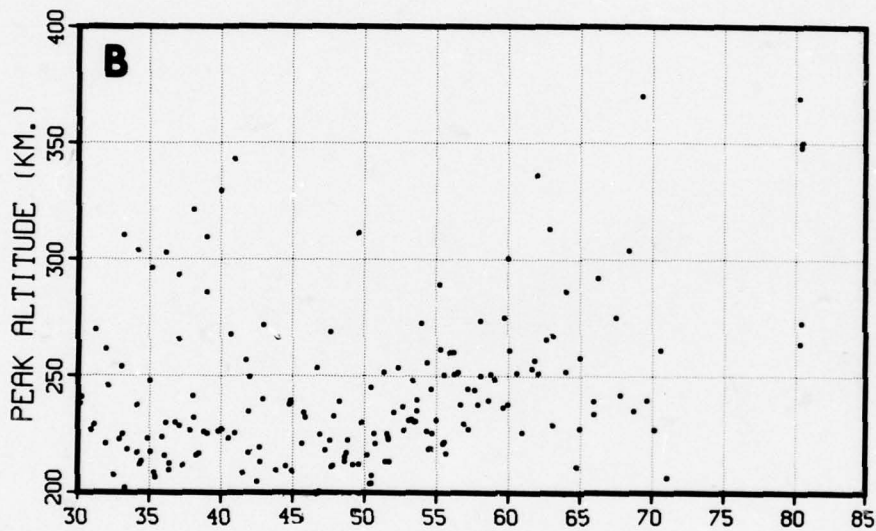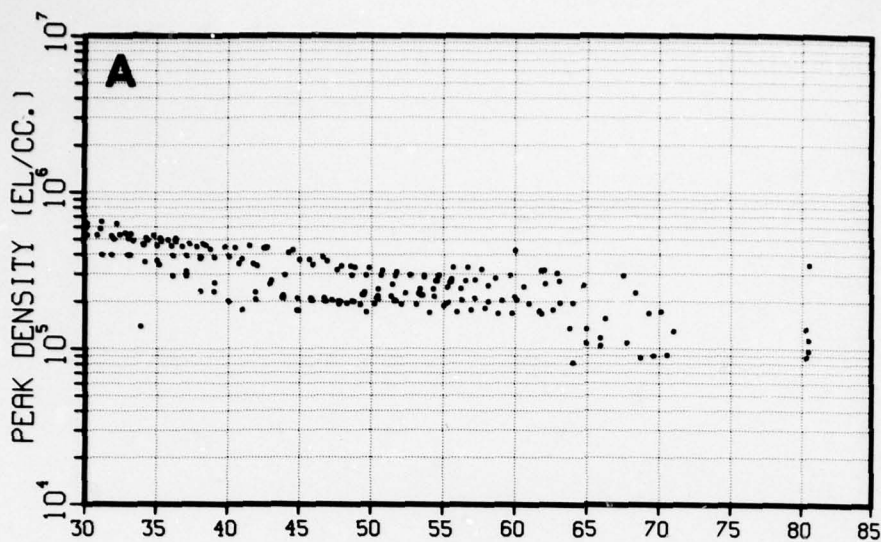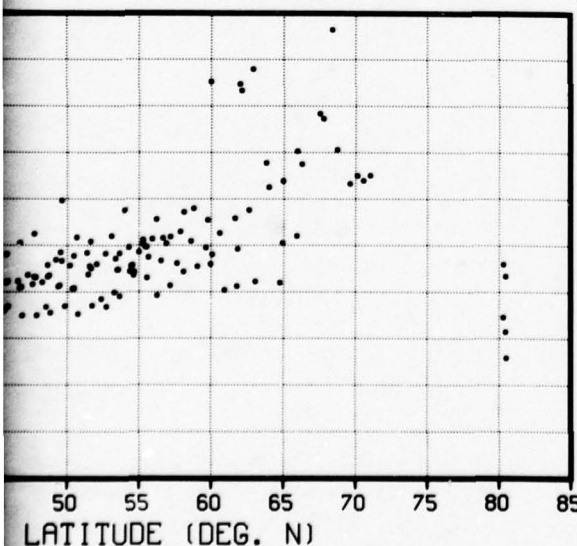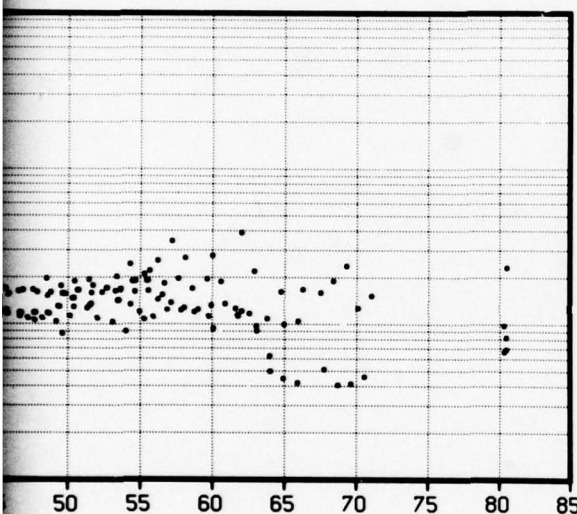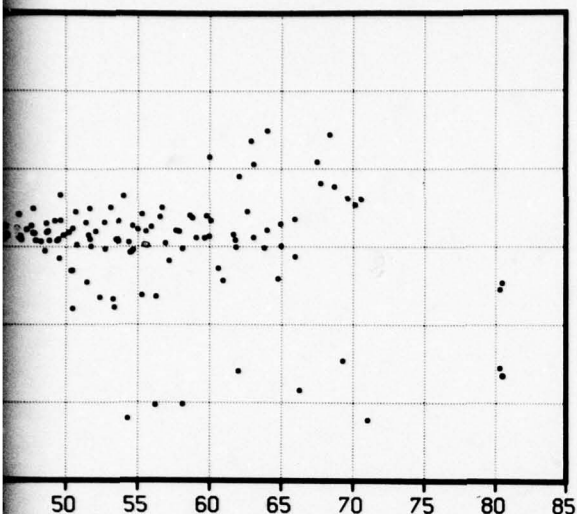
	Date	LMT	K_p	R_z	Longitude
Minimum	9/1	08:00	37	0	50°W
Maximum	11/30	12:00	57	50	150°W

A. Peak Density

B. Peak Altitude

C. Scale Height at the F2 Peak

D. Scale Height Gradient at the F2 Peak

E. Product of the Peak Density and Scale Height

F. Scale Height at 300 km Above the F2 Peak

Figure 2-10. Scatter Plots of Fits to Alouette I Data,
9/1 to 11/30, 08:00 to 12:00 LMT
(199 points are plotted)

LATITUDE (DEG. N)
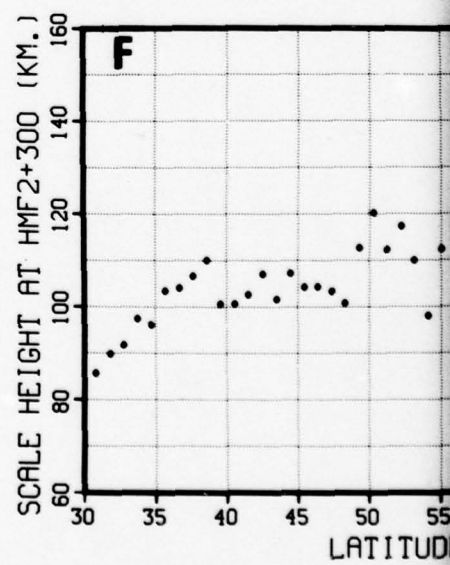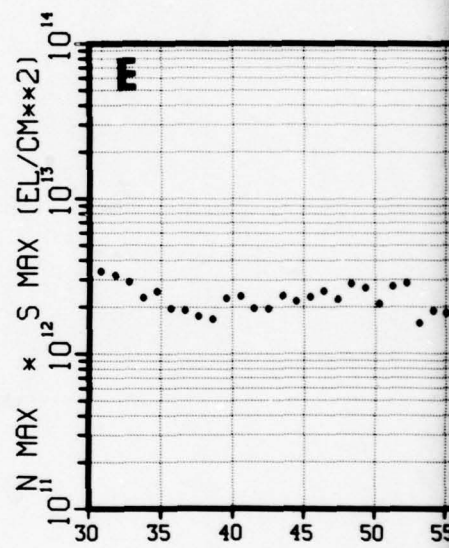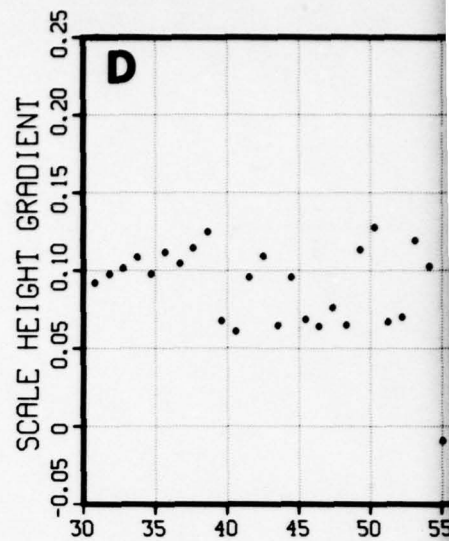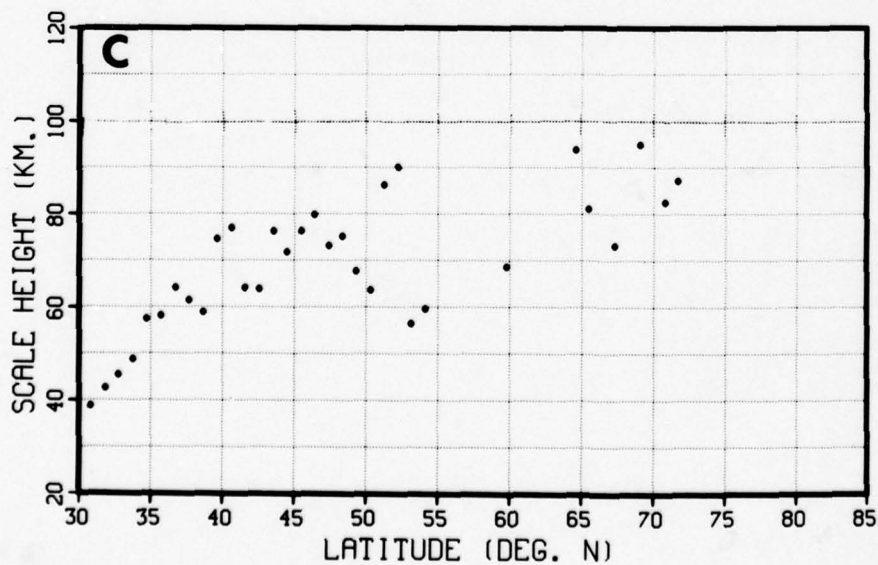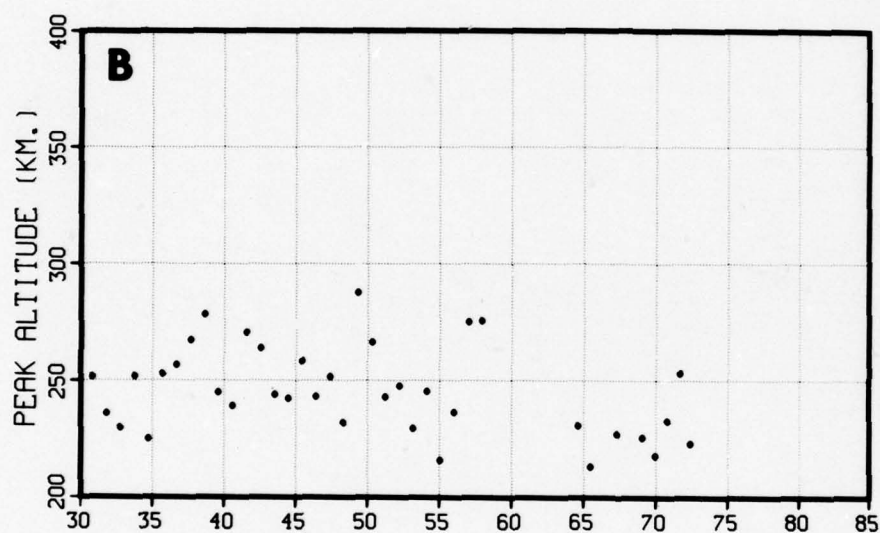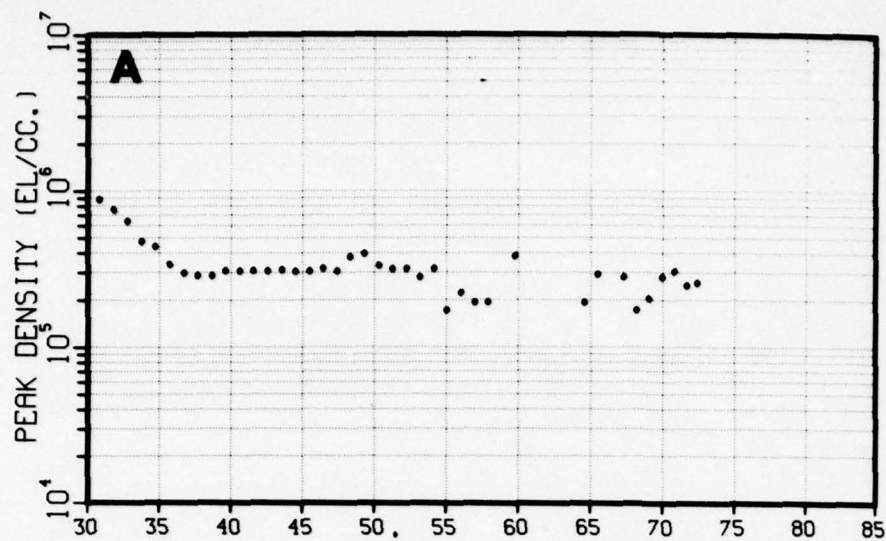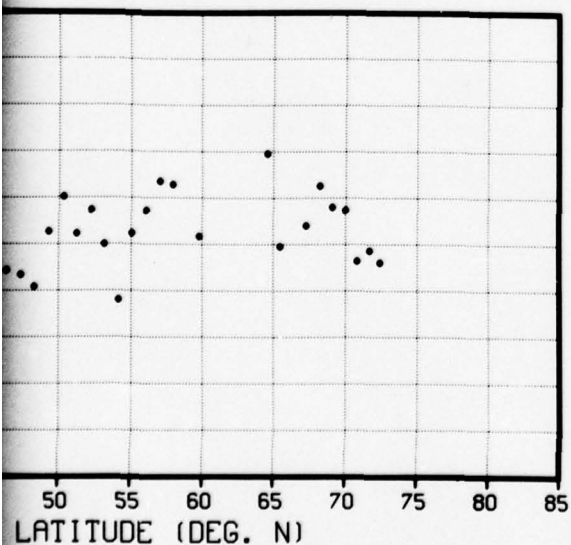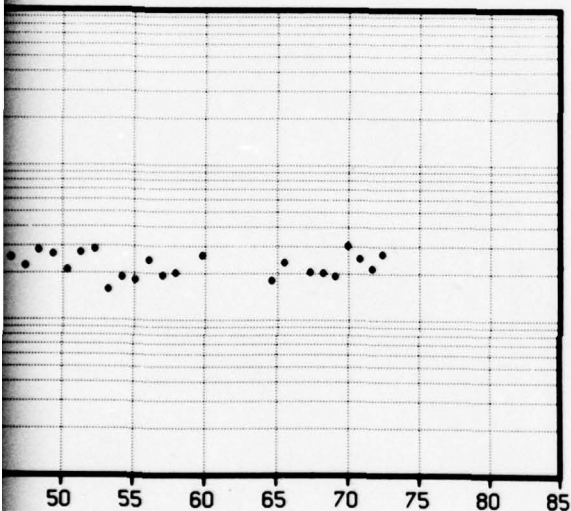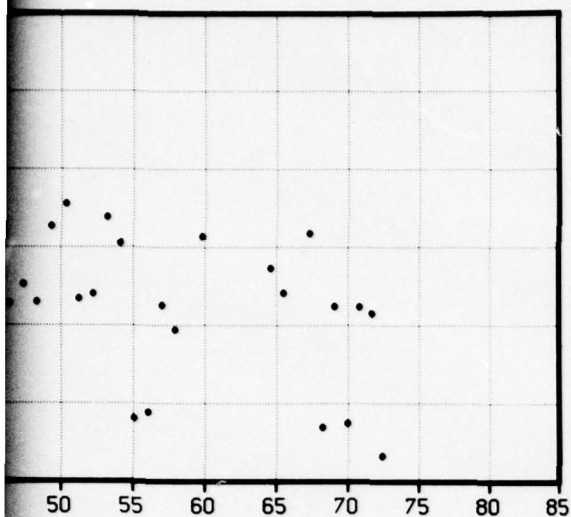
	Date	LMT	K_p	R_z	Longitude
Minimum	3/1	12:00	60	0	50°W
Maximum	5/31	16:00	90	50	150°W

A. Peak Density

B. Peak Altitude

C. Scale Height at the F2 Peak

D. Scale Height Gradient at the F2 Peak

E. Product of the Peak Density and Scale Height

F. Scale Height at 300 km Above the F2 Peak

Figure 2-11. Scatter Plots of Fits to Alouette I Data,
3/1 to 5/31, 12:00 to 16:00 LMT
(39 points are plotted)

LATITUDE (DEG. N)

A. Peak Density
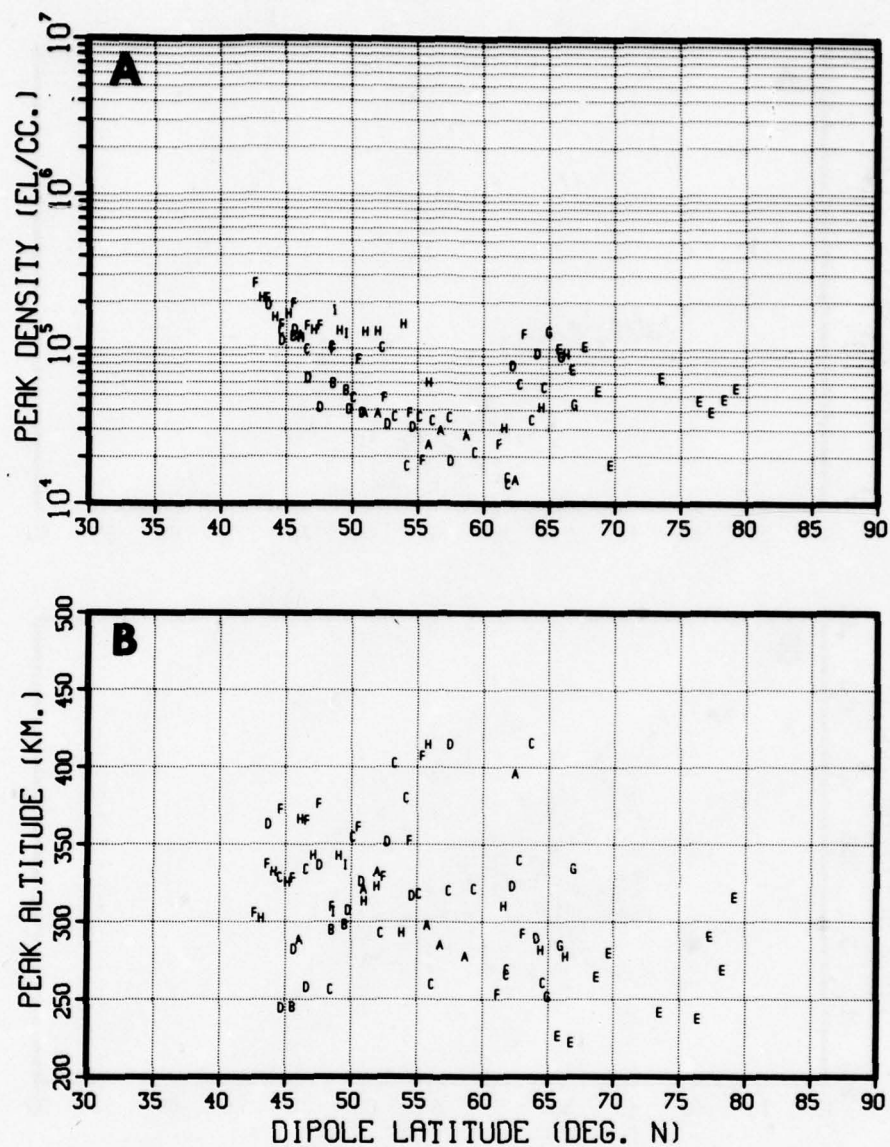
B. Peak Altitude

	Date	LMT	K_p	R_z	Dipole Longitude
Minimum	9/1	00:00	0	0	-100
Maximum	11/30	04:00	20	50	20

Figure 2-12. Scatter Plots of Fits to Alouette I Data,
9/1 to 11/30, 00:00 to 04:00 LMT
(10 satellite passes are plotted)
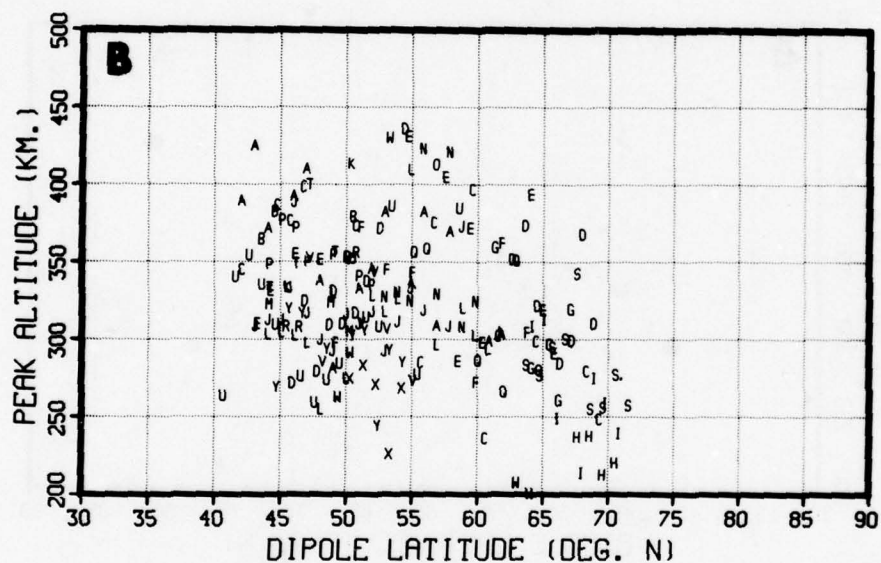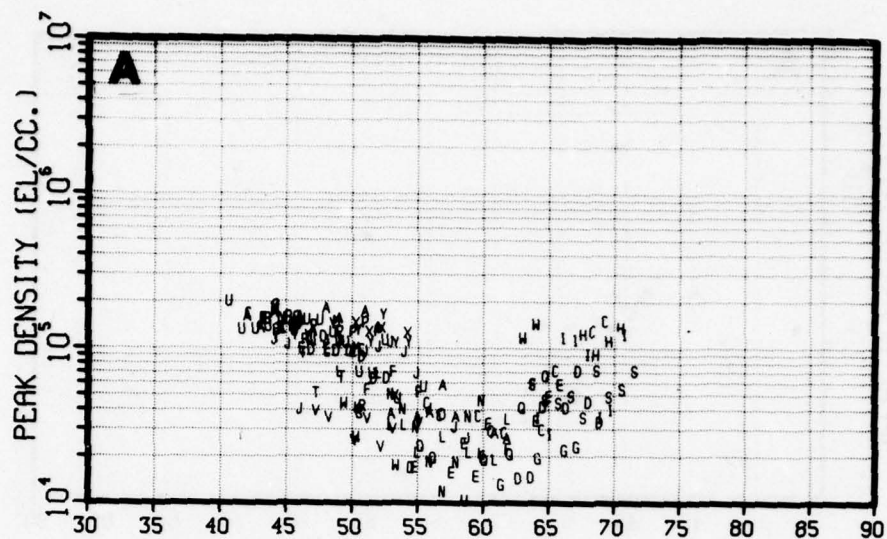
	Date	LMT	K_p	R_z	Dipole Longitude
Minimum	12/1	00:00	0	0	-100
Maximum	2/28	04:00	20	50	20

A. Peak Density

B. Peak Altitude

Figure 2-13. Scatter Plots of Fits to Alouette I Data,
12/1 to 2/28, 00:00 to 04:00 LMT
(25 satellite passes are plotted)

G

I

H

J

Rz

DIPOLE LATITUDE (DEG. N)

ZENITH ANGLE (DEG.) AND RZ

DIPOLE LONGITUDE (DEG. E)

DIPOLE LATITUDE (DEG. N)

31

		Date	LMT	K_p	R_Z	Dipole Longitude
A and B	Minimum	12/1	04:00	0	0	−100
	Maximum	2/28	08:00	20	50	20
	7 satellite passes are plotted					
C and D	Minimum	3/1	04:00	0	0	−100
	Maximum	5/31	08:00	20	50	20
	14 satellite passes are plotted					
E and F	Minimum	6/1	04:00	0	0	−100
	Maximum	8/31	08:00	20	50	20
	5 satellite passes are plotted					
G and H	Minimum	9/1	04:00	0	0	−100
	Maximum	11/30	08:00	20	50	20
	25 satellite passes are plotted					
I and J	Minimum	9/1	04:00	23	0	−100
	Maximum	11/30	08:00	34	50	20
	8 satellite passes are plotted					

A, C, E, G, and I illustrate changes in dipole longitude under various conditions

B, D, F, H, and J illustrate changes in zenith angle and R_Z under various conditions

Figure 2-14. Scatter Plots of Fits to Alouette I Data, Zenith Angle, R_Z and Dipole Longitude

		Date	LMT	K_p	R_z	Dipole Longitude
A and B	Minimum	12/1	04:00	0	0	-100
	Maximum	2/28	08:00	20	50	20
		7 satellite passes are plotted				
C and D	Minimum	6/1	04:00	0	0	-100
	Maximum	8/31	08:00	20	50	20
		5 satellite passes are plotted				

A and C. Peak Density

B and D. Peak Altitude

Figure 2-15. Scatter Plots of Fits to Alouette I Data,
12/1 to 2/28 and 6/1 to 8/31, 04:00 to 08:00 LMT

LATITUDE (DEG. N)
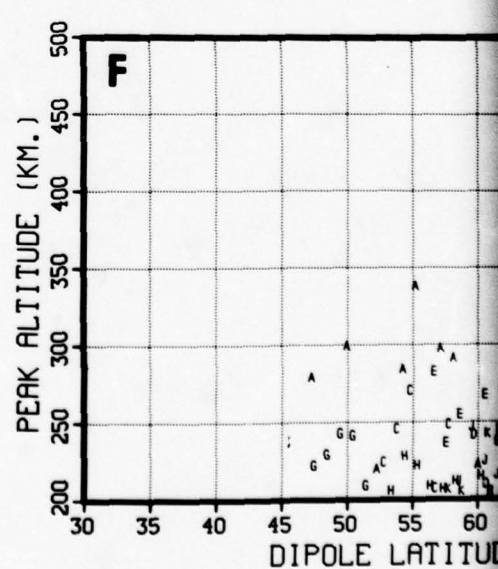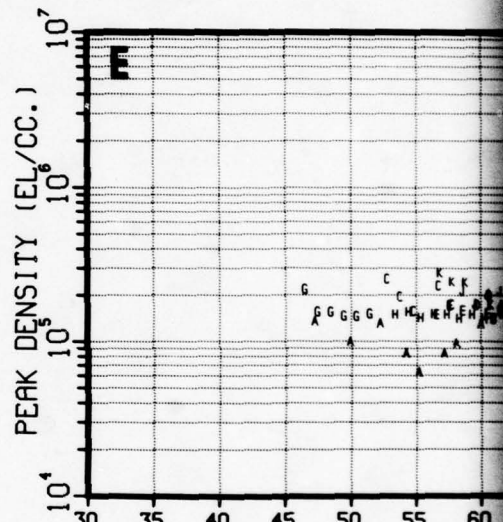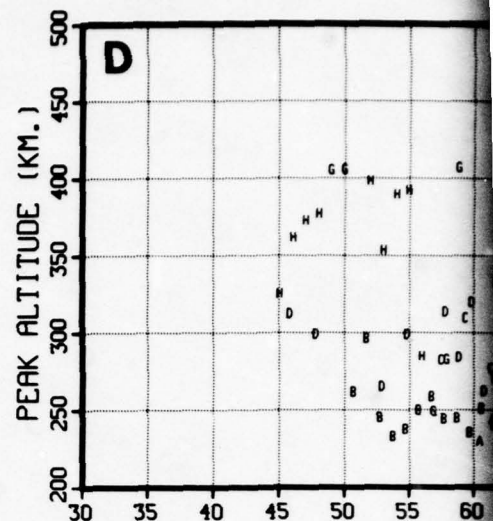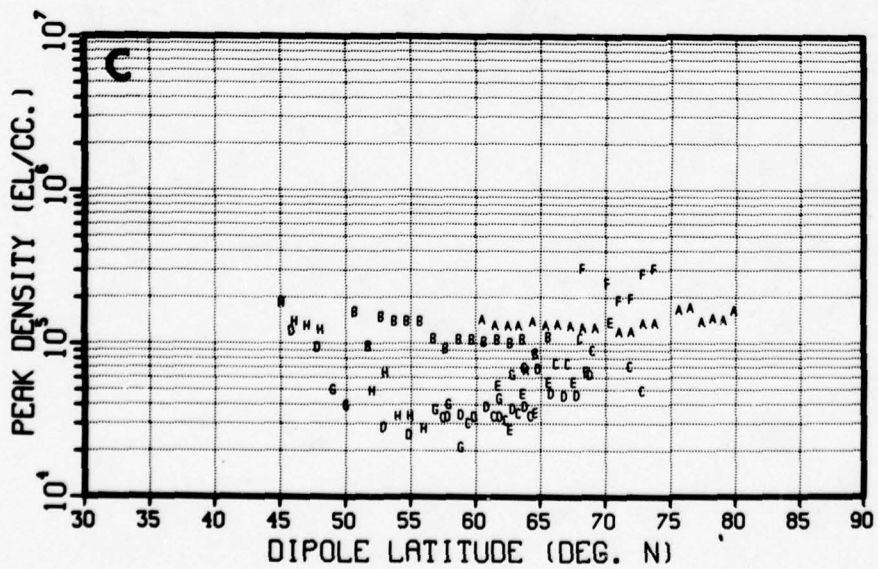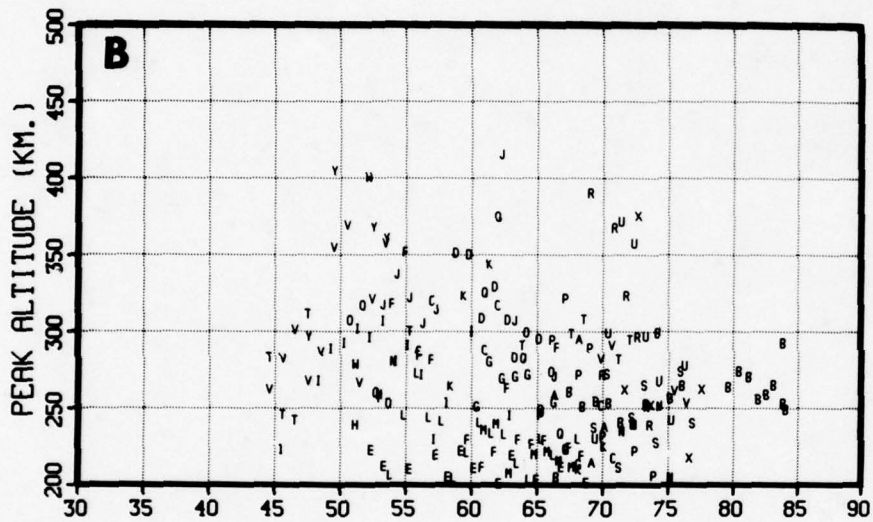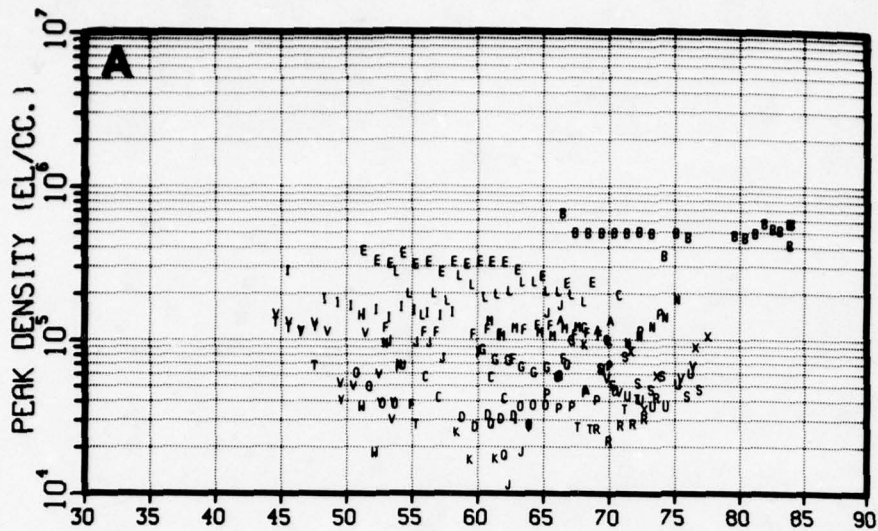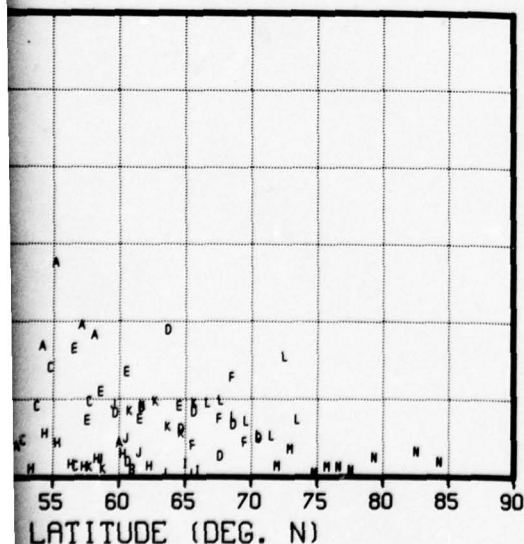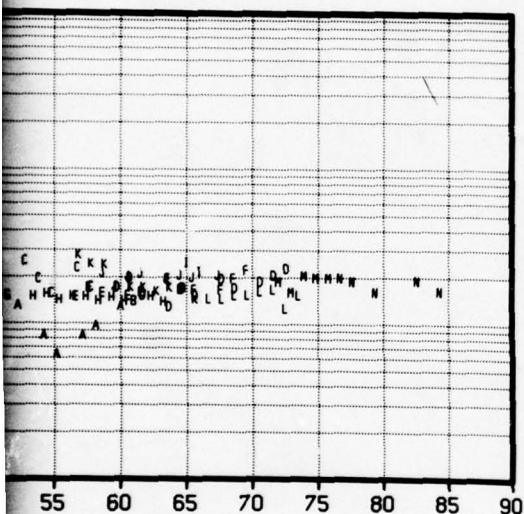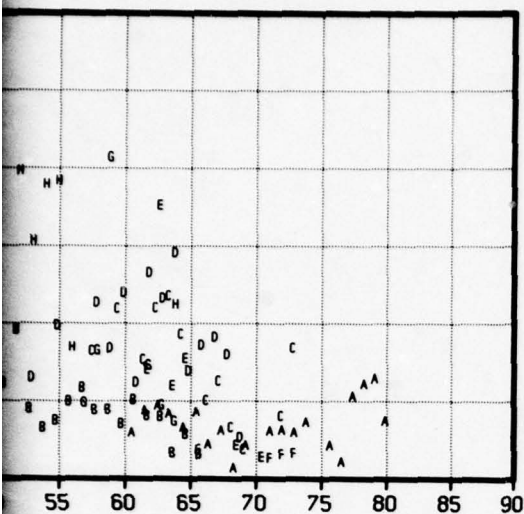
		Date	LMT	K_p	R_z	Dipole Longitude
A and B	Minimum	9/1	04:00	0	0	-100
	Maximum	11/30	08:00	20	50	20
	25 satellite passes are plotted					
C and D	Minimum	9/1	04:00	23	0	-100
	Maximum	11/30	08:00	34	50	20
	8 satellite passes are plotted					
E and F	Minimum	3/1	04:00	0	0	-100
	Maximum	5/31	08:00	20	50	20
	14 satellite passes are plotted					

A, C, E. Peak Density

B, D, F. Peak Altitude

Figure 2-16. Scatter Plots of Fits to Alouette I Data, 9/1 to 11/30, and 3/1 to 5/31, 04:00 to 08:00 LMT

LATITUDE (DEG. N)

2-41

satellite pass B occurs at ground-level dawn. There is a weak trough-like decrease in N_m at the proper latitude and no recovery to the north. It is not certain whether the decrease is due to the trough or to noise, but it is suggestive that this pass exhibits the trough just before it is totally filled in.

In the dusk (16 to 20 hr) fall bin, narrow troughs can be observed (Figure 2-17). However, they are only detectable by following the individual satellite passes because the trough widths (about two to three degrees) are smaller than the spread in latitude of the trough minimums; the minimum in pass B is at 10^4 el/cc, 66 degrees while the minimum pass D is at 1.5×10^5 el/cc, 73 degrees. A similar situation occurs in the winter 16 to 20 hr bin (Figure 2-18) except that the individual troughs are wider (about five degrees). The added width is part due to the fact that the zenith angles are larger in the winter than in the fall since the winter data is predominantly from December.

In spring and summer nighttime bins (20 to 24 and 0 to 4 hr) troughs are not as well defined as their fall and winter counterparts. In the 20 to 24 hr bin, the trough is shallower than in the fall and winter. It also seems more variable in location and the walls have smaller gradients. Data for the 0 to 4 hr bin are found for summer [Figure 2-19(A) and (B)] but not for spring. Even in the former season data are relatively scarce. Again, the gradients are smaller than in fall or winter. There appears to be a high-latitude trough observed during pass A, since it is about five degrees north of the next most northerly trough (pass D). The shallowness and smallness of the gradients of these trough cross sections probably account for the scarcity of troughs detected in these two seasons by Tulunay and Sayers [1971] since their detection algorithm required one sharp side and a reduction in peak electron density by a factor of two with respect to every other peak electron density between 30°N and 70°N geographic.

Examination of the scale-height plots shows that there is an enhancement of scale height at the peak in the trough region, although the largest scale height is not definitely attached to any specific trough feature. When a scale-height maximum is observed, there is a corresponding minimum in the scale height gradient (Figure 2-20), so the trough bottom is not indicated by any feature in a plot of the topside scale height [Figure 2-21(B)] at low K_p. This result is not very surprising, however. At low F-region altitudes the loss rates are proportional to N^2, while at higher altitudes the rate is more nearly proportional to N. This decreases the densities preferentially at or below the peak compared with the upper topside which increases the average topside scale height. There is a longer duration of solar illumination at the upper altitudes which also increases the scale height preferentially at high altitudes. The mechanism which produces the trough is likely to be insensitive to altitude and consequently the scale height need not increase particularly rapidly.

2-43

A

PEAK DENSITY (EL/CC.)

10^7

10^6

10^5

10^4

10^1

30 35 40 45 50 55 60 65 70 75 80 85 90

B

PEAK ALTITUDE (KM.)

500
450
400
350
300
250
200

30 35 40 45 50 55 60 65 70 75 80 85 90

DIPOLE LATITUDE (DEG. N)
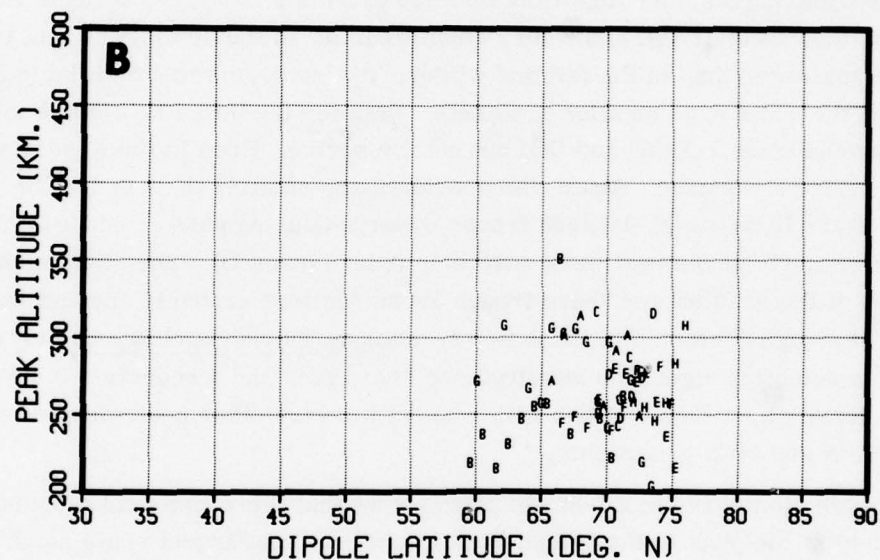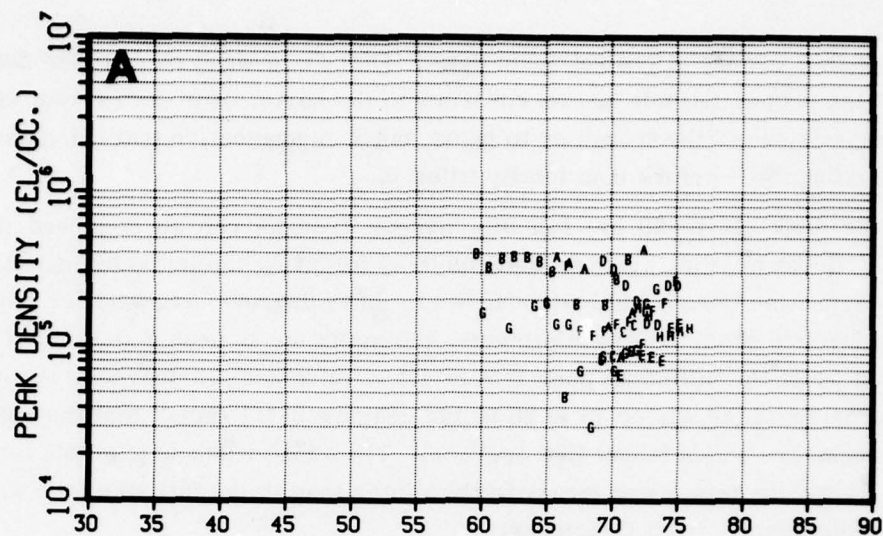
	Date	LMT	K_p	R_z	Dipole Longitude
Minimum	9/1	16:00	0	0	-100
Maximum	11/30	20:00	20	50	20

A. Peak Density

B. Peak Altitude

Figure 2-17. Scatter Plots of Fits to Alouette I Data,
9/1 to 11/30, 16:00 to 20:00 LMT
(8 satellite passes are plotted)

2-44
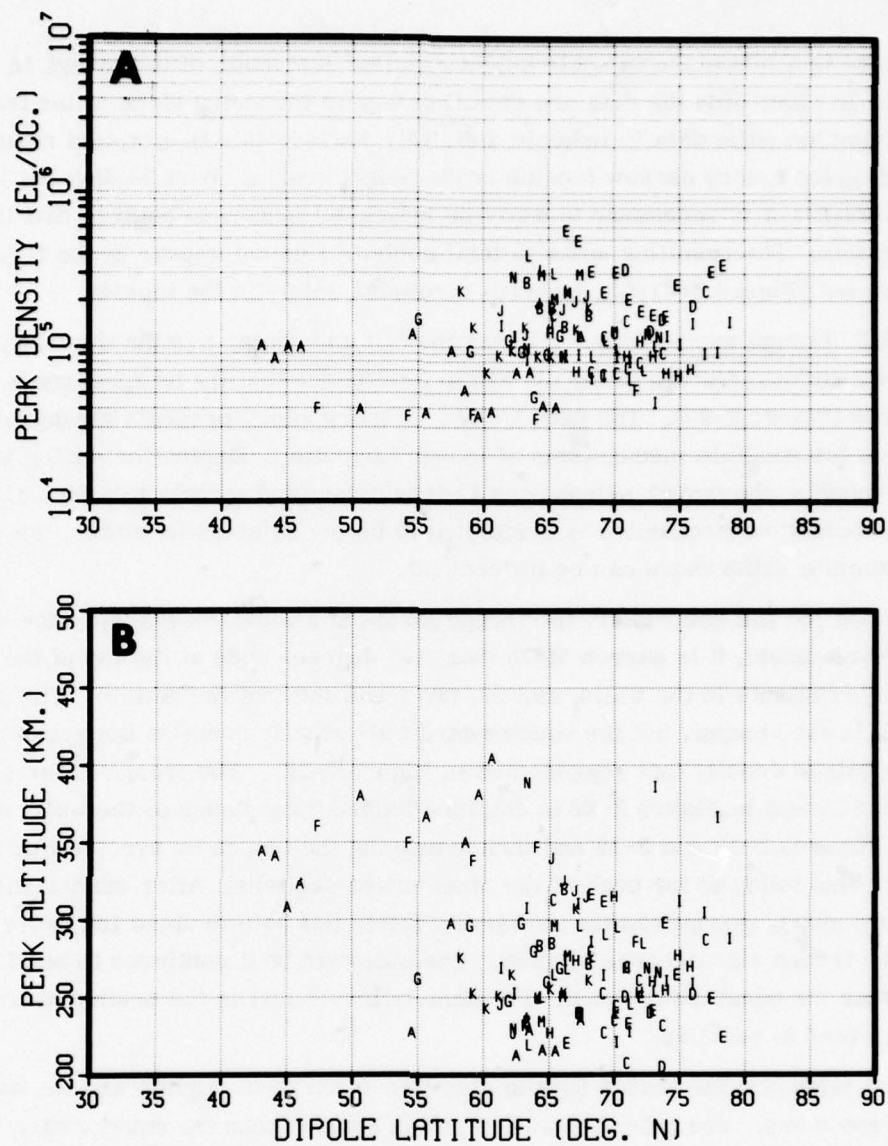
	Date	LMT	K_p	R_z	Dipole Longitude
Minimum	12/1	16:00	0	0	-100
Maximum	2/28	20:00	20	50	20
14 satellite passes are plotted					

A. Peak Density

B. Peak Altitude

Figure 2-18. Scatter Plots of Fits to Alouette I Data,
12/1 to 2/28, 16:00 to 20:00 LMT

There is a maximum in scale height gradient just south of the trough in Figure 2-20. In other bins the data are cut off closer to the sharp slope in the trough 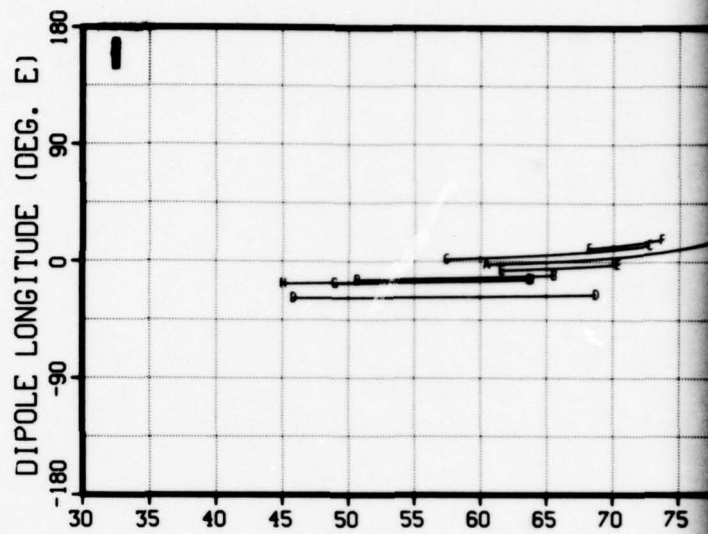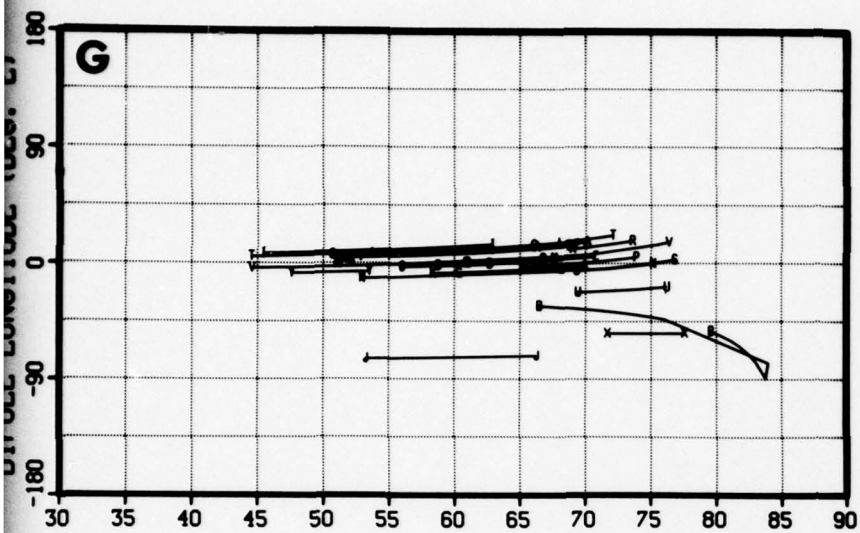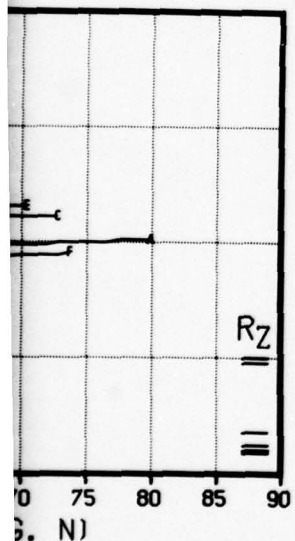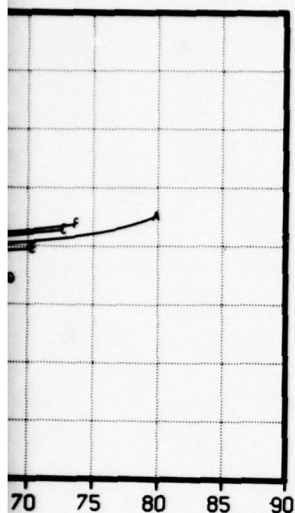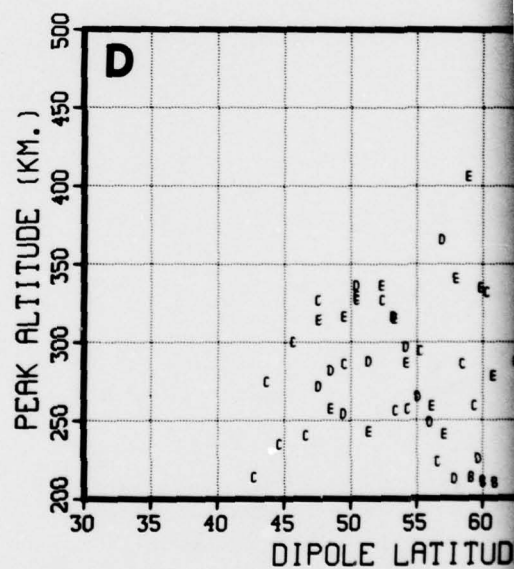wall, leaving too little data to indicate definitely whether this is a typical result. This peak gives a very narrow topside scale-height peak at about 54 degrees in Figure 2-21(B); it is necessary to examine individual passes to be sure that the feature exists. The resulting spike in total content does not appear in the $N_m s_m$ plot of the set [Figure 2-21(A)], because it resides solely in the topside.

2.3.3 Trough morphology.* During the fall and winter months the trough is such a well-defined feature of the nighttime ionosphere that its morphology is easy to describe (Figure 2-22). The detailed trough morphology presents strong constraints on the possible mechanisms of trough formation. During the spring and summer months, the trough morphology is less clear (due largely to a lack of data), but if the formation mechanism is postulated to be the same as in winter, the winter-summer differences can be understood.

During the fall and winter, the trough forms at a local geographic time near ground-level sunset. It is narrow (less than five degrees wide at the top of the walls), has strong gradients in the walls, and the two walls meet at the bottom. The poleward wall is the steeper, but the equatorward wall usually contains the greater total drop in electron density (not represented in Figure 2-22). The trough cross section shown near sunset in Figure 2-22 is obtained from fitting slopes to the walls depicted in Figures 2-17 and 2-18 and then averaging the slopes by eye. A similar procedure was followed for each of the other cross sections. After sunset, the walls move apart, leaving (on the average) a fairly flat bottom about ten degrees wide. The trough also deepens slightly. The poleward wall continues to be slightly steeper than the equatorward wall. The density levels just to the south and north of the trough tend to equalize.

Past midnight, the trough fills in slightly. It narrows slightly and the walls become less steep. The poleward wall remains steeper than the equatorward wall. As dawn approaches the trough fills in. It becomes narrower at the top, but it becomes shallow considerably more rapidly so that the width of the bottom is about five degrees just before complete fill in. The bottom of the trough becomes rougher and the poleward wall seems to become shallow more rapidly than the equatorward wall.

The trough morphology just described can be understood qualitatively by the following description (see Figure 2-23). For a first approximation, neglect the axial tilt of the earth. Then there is an almost-inertial coordinate system (it rotates once per year) formed by using local time as a longitudinal coordinate converted to degrees, if desired, by the usual factor of 15 degrees per hour. The

*This section has been refined and amplified in Section 2.6.
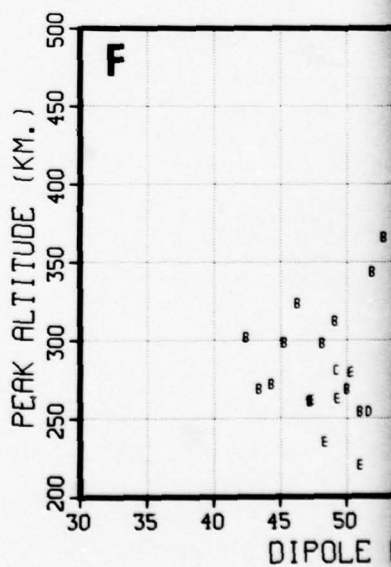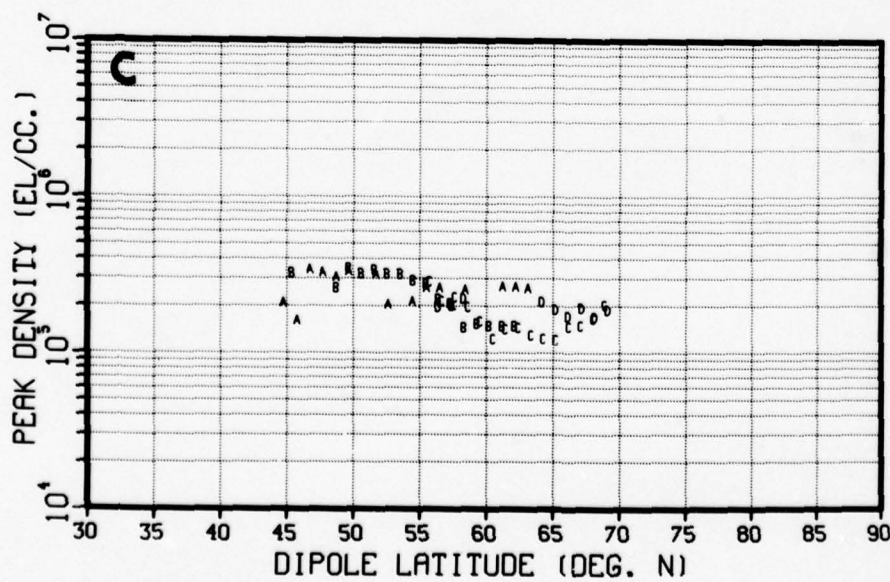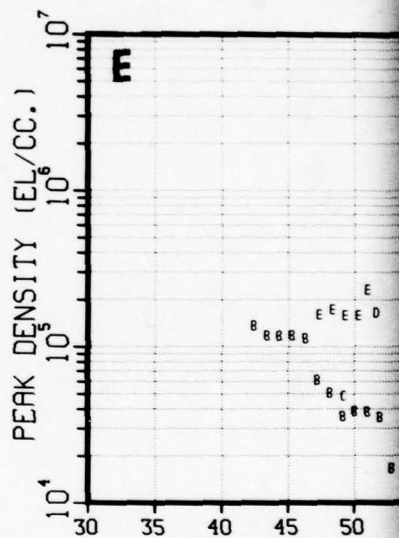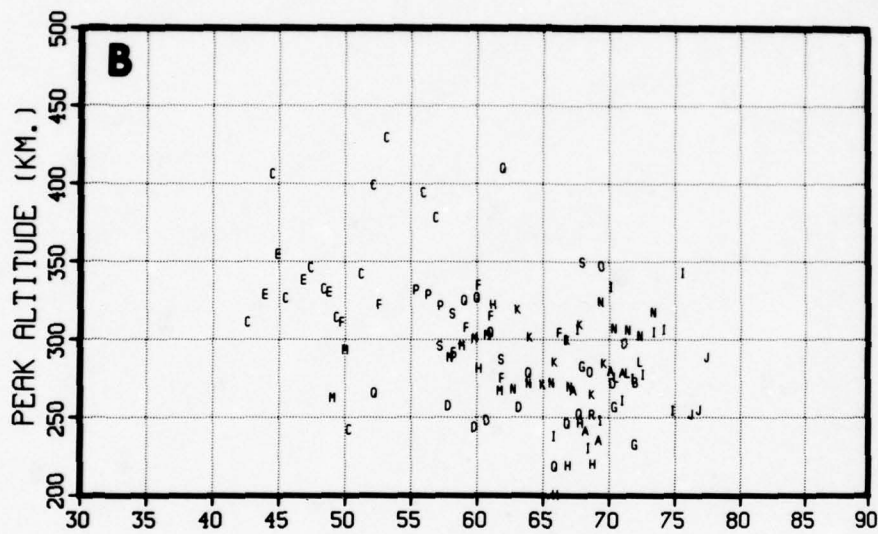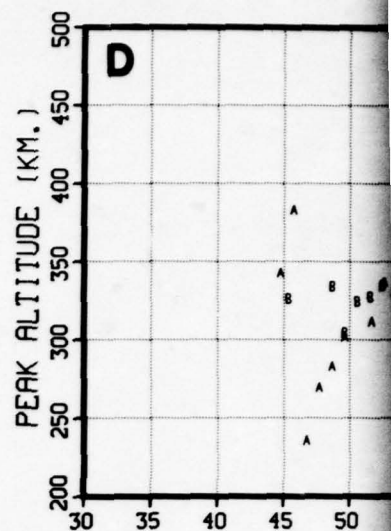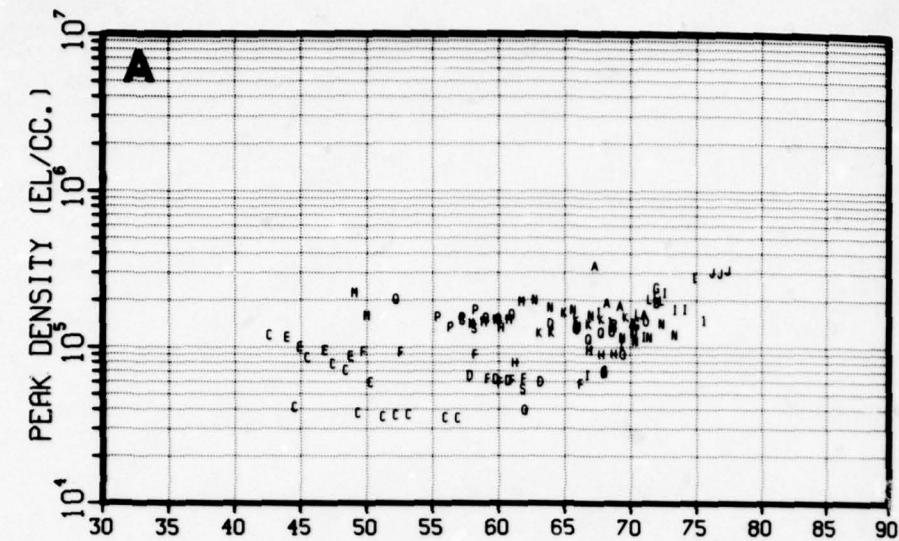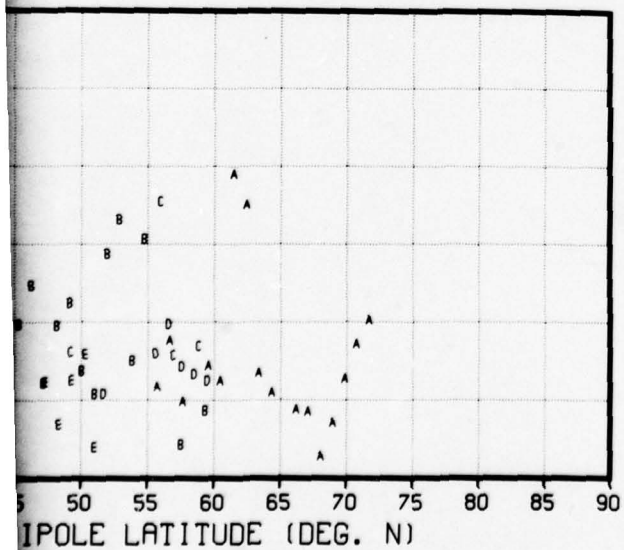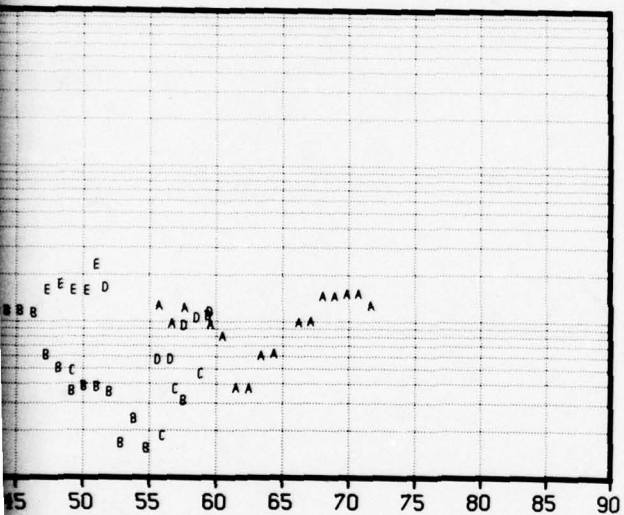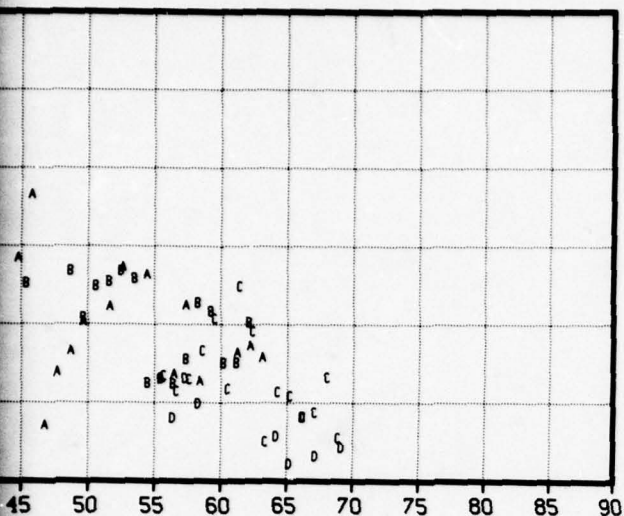
		Date	LMT	K_p	R_z	Dipole Longitude
A and B	Minimum	3/1	20:00	0	0	-100
	Maximum	5/31	24:00	20	50	20
	19 satellite passes are plotted					
C and D	Minimum	6/1	20:00	0	0	-100
	Maximum	8/31	24:00	20	50	20
	4 satellite passes are plotted					
E and F	Minimum	6/1	00:00	0	0	-100
	Maximum	8/31	04:00	20	50	20
	5 satellite passes are plotted					

A, C, E. Peak Density

B, D, F. Peak Altitude

Figure 2-19. Scatter Plots of Fits to Alouette I Data,
3/1 to 5/31 and 6/1 to 8/31 (20:00 to 24:00 LMT)
and 6/1 to 8/31 (00:00 to 04:00 LMT)

2-47

	Date	LMT	K_p	R_z	Dipole Longitude
Minimum	12/1	00:00	0	0	-100
Maximum	2/28	04:00	20	50	20
	25 satellite passes are plotted				

A. Peak Density

B. Peak Altitude

Figure 2-20. Scatter Plots of Fits to Alouette I Data,
12/1 to 2/28, 00:00 to 04:00 LMT

2-49

A. Scale Height at 300 km Above the F2 Peak

B. Product of the Peak Density and Scale Height

Figure 2-21. Scatter Plots of Fits to Alouette I Data,
12/1 to 2/28, 00:00 to 04:00 LMT

	Date	LMT	K_p	R_z	Dipole Longitude
Minimum	12/1	00:00	0	0	-100
Maximum	2/28	04:00	20	50	20
	25 satellite passes are plotted				
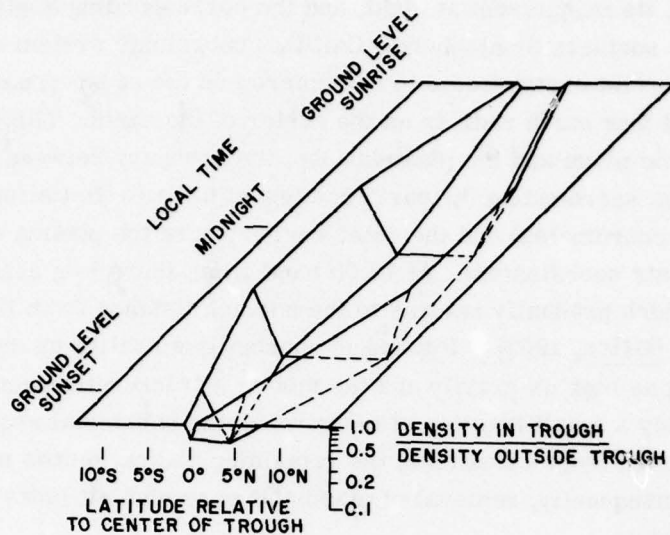
Figure 2-22. Morphology of the Main Electron
Density Trough During Fall and Winter
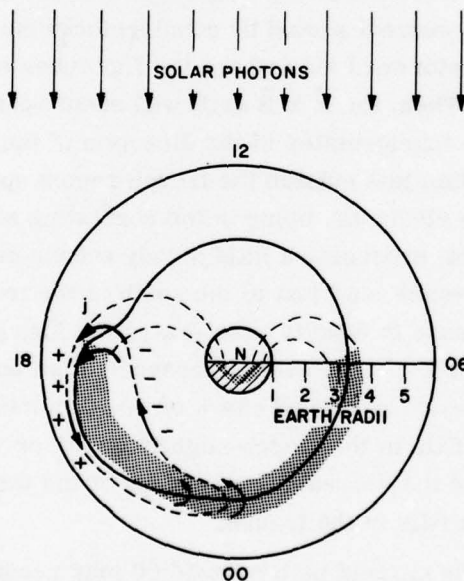
Figure 2-23. A Magnetospheric
Current System Which Could
Form the Main Trough

corresponding latitude is formed by the solar zenith angle for daytime in the northern hemisphere, its supplement at night, and the corresponding angles with a negative sign for the southern hemisphere. Call this coordinate system ecliptic coordinates. The important arena seems to be centered on the equator, i.e., the ecliptic plane — at about four earth radii from the center of the earth. This is the intersection of the ecliptic plane and the plasmapause, the boundary between the inner region where the plasma surrounding the earth rotates with the earth (is fixed in geographic or geomagnetic coordinates) and the outer region where the plasma does not rotate (is fixed in ecliptic coordinates). At 18:00 local time, there is a sharp bulge in the plasmapause, which gradually returns to the normal distance from the earth shortly before midnight [Brice, 1967]. Plasma is constantly spiraling up and down and the field lines going as high as gravity and the mutual attraction between electrons and ions permit. Only a small fraction of these reach the equatorial region. However, if they are removed from a flux tube, the remaining plasma moves up slightly and replaces it. Consequently, removal of plasma at very high altitudes tends to empty the entire flux tube.

It is proposed that the shear in the plasma interacts (perhaps via a flow instability) with the bulge in the magnetosphere so as to produce a current around the bulge. If the current is strongest near the sharp front at 18:00 and weak elsewhere, there will be a mechanism for removing electrons from the flux tubes entering the region. The sense of the current should be counterclockwise so electrons accumulate on the inside (equatorward side where the flux tubes enter the ionosphere) and ions on the outside. Then, the $\vec{E} \times \vec{B}$ drift will ensure that the plasma remaining within the trough flux tubes rotates in the direction of the earth. The electrons (and ions) which accumulate just outside the trough region spiral down the field line into the ionsophere. The electrons, being in the corotating zone, drift away from the region of enhancement, producing a mild steady enhancement of total electron content in the flux tubes which land just to the south of the trough. The ions tend to accumulate but the increase in density accelerates the loss processes and a steady state can be achieved. (A test to detect the presence of an enhancement in ion density north of the trough would be a good check of this picture.) Past 0:00 local time, the weak return current fills in the trough slightly and it or cross field diffusion in the ionosphere may cause the decreasing steepness of the walls. As ground-level sunrise nears, solar flux fills in the trough.

The curvature of the current path near 18:00 may account for the sharp minimum in the very early trough, for there is only one latitude where a flux tube meets the current first. It should be noted that the trough is formed inside the bulge and

thus it does not follow the plasmapause very closely in the 18:00 sector. This correlation failure has been noticed by Thomas and Andrews [1968].

To understand the winter-summer difference, it is necessary to take into account the tilt of the earth's axis. The ecliptic coordinate system is still the proper one to use, but the discrepancy between local ecliptic time and local geographic time is negligible. Near the summer solstice the sun is higher in the sky for any local time than it is in the winter. Consequently, near 18:00 ecliptic time as the overhead flux tubes enter the plasmasphere bulge, solar electron production is still taking place in the ionospheric part of the flux tube and conflicts with the proposed loss mechanism. The trough region is therefore not as strongly depleted and is shallower with less steep walls. It appears at a later local time and disappears at an earlier one.

2.4 Calculation of Invariant Latitude

L shells were defined by C. E. McIlwain [1960] as a particularly accurate coordinate system for trapped particle studies. An L shell is defined so that within the adiabatic approximation charged particles drift in a fashion which keeps them on a fixed L shell. These shells are however, fundamentally dissimilar from more usual coordinate systems. A latitude can, however, be defined by the following relation:

$$\cos \Lambda = \frac{1}{\sqrt{L}}$$

when L is specified in units of earth radii. The latitude so defined is the invariant latitude. For a point on the surface of the earth in a dipole field, the invariant latitude and the geomagnetic (centered dipole) latitude coincide. L is the distance in earth radii from the center of the earth to the intersection of the magnetic equatorial plane and the field line passing through the given point.

A program which computes the values of L from its definition is quite large and slow running. For practical use, it is possible to construct a large table of L or Λ as a function of geographic latitude and longitude. Alternatively, one can fit an analytically-defined coordinate transformation which approximates the results of the exact calculation over some latitude range. The latter is the procedure which is described here.

For modeling purposes an rms accuracy of ±1 degree would probably suffice since there are diurnal motions of such ionospheric features as the trough and the boundaries of the auroral oval which are large compared with one degree. However, it has proven quite feasible to reduce the errors to significantly below one degree. At such accuracies, it is necessary to specify the altitude of the point at which the

2-53

invariant latitude is to be obtained. (All points on an L shell have the same invariant latitude and field lines approximately follow L shells.) The altitude chosen is 300 km (the approximate altitude of the F2 peak). Auroral data are given by Feldstein, et al.[1963], in the corrected geomagnetic coordinates of Huldqvist [1958] and Hakura [1965] which corresponds within an estimated 0.5 degrees to 0 km invariant latitude). However, Bates, et al.[1973], assert that auroral ionization drifts up to the F region along field lines (as theoretically expected). This effect is properly taken into account by shifting the auroral oval models from 100 km (the height of aurora) to 300 km by keeping the invariant latitude fixed. At 65 to 70 degrees invariant latitude (L = 6 to 8) the location of the southern edge of the auroral zone in daytime, this displacement is about 0.5 degrees south from 100 to 300 km. At 77 degrees invariant latitude (L = 20), corresponding to the northern boundary of the auroral zone, the displacement is about 0.2 degrees from 100 to 300 km.

The fitting was done by considering graphical data giving L as a function of geographic coordinates presented in Dudziak, et al.[1963]. The reading accuracy is roughly ±0.2 degrees. The most severe limitation of this data source is that L values exceeding 6 are not plotted. The location of the L pole is known to be near the corrected geomagnetic pole (80°N, 80°W), and this fact was used to keep the polar region reasonable. Only the region of L ≥ 2.5 was considered. After the coefficients were determined, the fit was checked with the 0-km invariant latitude of north polar stations as presented in the World Data Center Catalogue of Date [1970]. In both the 2.5 ≤ L ≤ 6 regime and the L > 6 regime, the fit is quite good.

The calculation consists of two main steps:

A. A transformation is made to a centered-dipole coordinate system with the north pole at 73.6°N, 77.5°W. (This fits the European region within about 1 degree), and

B. A bulge is added to elongate the curves of constant invariant latitude at American longitudes.

The program is listed in Table 2-3. It is written in PL/I and includes a testing main program which is run from a time sharing terminal. The numbers on the left are line sequence numbers. The testing program occupies lines 10 through 80 and line 510. Line 100 corresponds to a SUBROUTINE statement in a FORTRAN program. Lines 100 through 130 declare that LAT and LONG are floating point variables and give initial values for the other variable. DR is the degree-to-radian conversion factor. COSCOLO and SINCOLO are the cosine and sine of COLATO (= 6.3 degrees) respectively, the geographic colatitude of the north pole of the intermediate coordinate system. Lines 210 through 290 calculate a standard transformation from one set of spherical coordinates to another, while lines 300 through 350 obtain the longitude from its sine and perform a check that the arcsine function has given the longitude itself and not the supplement of the longitude.

2-54

Table 2-3
INVARIANT LATITUDE PROGRAM

```
00010   TEST: PROC OPTIONS(MAIN);
00020       DCL (LAT,LONG,L) FLOAT;
00030    START: GET LIST(LAT,LONG,L);
00040       CALL INVAR(LAT,LONG);
00050       CINVLAT = 90 - ASIN(1/SQRT(L))/.017455;
00060       DLAT = CINVLAT-LAT;
00070       PUT SKIP DATA(DLAT,LAT,LONG);
00080       GO TO START;
00090    INVAR: PROC(LAT,LONG);
00100       DCL DR INIT(.017455), COLATO INIT(6.3), LONGO INIT(-77.5) FLOAT;
00110       DCL (LAT, LONG) FLOAT;
00120       DCL A INIT(1.9), B INIT(.061), PI INIT(3.14159);
00130       DCL COSCOLO INIT(.993961), SINCOLO INIT(.109734);
00140       /*   FOR LATER USE, REQUIRE -180 < LONG <= 180   */
00150       LONG = MOD(LONG,360);
00160       IF LONG > 180 THEN LONG = LONG-360;
00170       FACARG = (LONG+5)/70.7107;       /* FOR USE IN THE MODIFICATION */
00180
00190       /*   OBTAIN DIPOLE COORDINATES   */
00200
00210       COSLATG = COS(LAT*DR);
00220       SINLATG = SIN(LAT*DR);
00230       DLONG = (LONG-LONGO)*DR;
00240       SINLAT = SINLATG*COSCOLO + COSLATG*SINCOLO*COS(DLONG);
00250       COLAT = ACOS(SINLAT);
00260       SINCOL = SIN(COLAT);
00270       SINDLONG = SIN(DLONG);
00280       SINLONG = COSLATG*SINDLONG/SINCOL;
00290       COLAT = COLAT/DR;
00300       LONG = ASIN(SINLONG);
00310       /* CHECK THE QUADRANT */
00320       SINLATCH = COSCOLO*SINLAT - SINCOLO*SINCOL*COS(LONG);
00330       IF ABS(SINLATCH/SINLATG-1) > .0001 THEN
00340           LONG = PI - LONG;
00350       LONG = LONG/DR;
00360
00370       /*   MODIFY DIPOLE COORDINATES   */
00380
00390       BUMPLONG = (.22+.004*(COLAT-40))*(COLAT-40);
00400       DLONG = (LONG-BUMPLONG)*DR;
00410       ALONG = (MOD(LONG,360)-165)/30;
00420       COLAT = COLAT*(1-.03*EXP(-ALONG**2));
00430       COSDL = COS(DLONG);
00440       COS2DL = COS(2*DLONG);
00450       FAC = .3 + .582911*FACARG*EXP(-FACARG**2);
00460       BETA = (1-FAC)*COS2DL + FAC + COSDL;
00470       COLATINV = (COLAT - A*BETA)/(1+B*BETA);
00480       LAT = MIN(90 - COLATINV,90);
00490       RETURN;
00500       END INVAR;
00510    END TEST;
```

Lines 390 through 580 modify the dipole coordinates. BUMPLONG is the dipole longitude of the southernmost (geographic) extent of a given L shell. The relation of line 390 is an approximation; it is strictly valid for all longitudes only if rewritten in terms of invariant colatitude. However, to do that would require iteration and a significant slowdown of the program. The errors introduced by the approximation ultimately affect dipole longitudes ±90 degrees preferentially. This region has other possible error sources, all of which are dealt with together. The quality β (BETA in line 460) defines the bulge as a function of longitude. For all values of FAC (which is described below), β is 2 at BUMPLONG and 0 when 180 degrees away from it. At BUMPLONG, the bulge is 3.8 + 0.122 Λ' degrees, where Λ' is the invariant colatitude. From the estimate of the bulge, the invariant colatitude may be obtained (without further approximation) as in line 470. Note that A = 3.8/2 and B = 0.122/2. Λ' = 0 occurs at a geographic colatitude of 10.2 degrees, on the 81°W meridian, very close to the actual L pole.

FAC describes the relative proportions of two types of bulges. When FAC = 0, β = cos 2 DLONG - cos DLONG which is negative at DLONG = ±90 degrees, while FAC = 1 implies that β = 1 + cos DLONG which is positive at DLONG = ±90 degrees. It was found that no constant value for FAC gave sufficiently small residuals at all longitudes. The expression in line 450, with FAC ARG defined in line 170, gives significantly better results. A discontinuity in FAC occurs at ±180° geographic longitude, but it is totally insignificant in magnitude. However, it is important that the geographic longitude be in the range -180° < LONG ≤ 180°. This condition is ensured upon entry to the procedure (lines 150 and 160).

With the algorithm as described to this point, a good fit is achieved to the data used at all longitudes except 90° geographic and, to a lesser extent, at 45° geographic. It was discovered that these larger errors occur because a given L shell reaches its most southern latitude at 75° to 80°W, but its most northern latitude is reached at about 135°E, not at 95° to 100°E. This produced errors of up to 1.8 degrees at 90°E, L = 2.5. A correction of up to three percent in dipole colatitude (nearly equal to geographic colatitude in this region) is made (lines 410, 420).

The residuals at 90 degrees are reduced in this fashion to fully acceptable values and the residuals at 45 degrees are reduced slightly. These residuals are presented in Table 2-4(A). The differences between the calculated 300-km latitude and the actual 0-km invariant latitude for polar ionospheric research stations (World Data Center Catalogue of Data) are given in Table 2-4(B). To obtain the 300-km latitude errors it is necessary to add a magnetic field model dependent quantity which is roughly 0.7 degrees at L = 6 to 8, 0.3 degrees at L = 20, 0.1 degrees at L = 100, and 0 degrees at the invariant pole.

Table 2-4
INVARIANT LATITUDE CALCULATIONS

Part A. Error in Calculating 300-km Invariant Latitude

L	Geographic Longitude (degrees)							
	-180	-130	-75	-45	0	45	90	135
6	-0.5	-0.2	0.1	0.8	-0.1	0.1	-0.3	-0.3
5	-0.3	-0.4	-0.1	-0.4	-0.	0.6	0.2	-0.3
4	-0.4	-0.3	-0.1	-0.1	-0.3	-0.6	0.1	-0.1
3	-0.1	0.1	0.1	-0.1	-1.0	0.9	0.5	-0.2
2.5	0.1	-0.2	0.1	-0.4	0.3	0.7	0.6	-0.1

Part B. Difference between 0-km Invariant Latitude and Calculated 300-km Invariant Latitude for Polar Stations, and Approximate 300-km Invariant Latitude Errors

Station	Geographic		0-km L Value	Invariant Latitude Difference	Approx 300-km Error
	Latitude	Longitude			
Alert	82.60	297.40	311.26	-0.6	-0.6
Barrow	71.30	203.20	8.02	-0.6	0.1
Bar I	69.60	219.80	9.16	-0.5	0.0
Bear Island	74.50	19.20	9.54	-0.7	-0.2
Churchill	58.80	265.80	8.59	-0.3	0.3
Eureka	80.00	274.10	3373.	-0.5	-0.5
Fletchers Ice Island	75.90	235.70	29.60	0.1	0.3
Frobisher Bay	63.80	291.40	14.58	-0.4	0.0
Godhavn	69.30	306.50	20.62	-0.6	-0.3
Heiss Island	80.60	58.00	14.10	-1.0	-0.6
Julianehaab	60.80	314.00	7.22	-0.8	-0.1
Kap Tobin	70.42	338.03	10.85	0.1	0.6
Kiruna	67.80	20.40	5.44	-0.7	0.0
Mould Bay	76.20	240.60	38.05	-0.1	0.2
Murmansk	68.95	33.05	5.56	-0.6	0.1
Narssarssuaq	61.20	314.60	7.38	-0.8	-0.1
Nord	81.67	343.33	38.17	-1.1	-0.8
Ny-Alesund	79.00	12.00	16.52	-0.7	-0.3
Preobrazhenie	74.70	112.90	7.30	-0.5	0.2
Pyramida	78.20	15.20	14.54	-0.8	-0.4
Resolute Bay	74.70	265.10	93.98	-0.0	-0.3
Sandur	65.00	353.80	6.88	-0.3	0.4
Sukkertoppen	65.42	307.10	12.79	-0.6	-0.2
Thule/Camp Tuto	76.40	291.30	169.92	-0.7	-0.6
Thule/Camp Quanaq	77.50	290.80	264.41	-0.8	-0.7
Tromso	69.70	19.00	6.32	-0.6	0.1
Uedinenie Island	77.50	82.30	9.68	-0.7	-0.2
Uranium City	59.50	251.40	7.26	-0.6	0.1
Yellowknife	62.40	245.60	8.33	-0.5	0.0

Near the invariant pole, there is a singularity in the coordinate system computed by the program in Table 2-3(A). It occurs because of type of perturbation used. At 0° dipole longitude, 90° dipole latitude, the perturbation is 3.8 degrees, while at 180° longitude the perturbation is zero. The Alouette data used in the HILION study does not go north of 80.5° geographic latitude and consequently does not approach the singular region except near 80°W. Fortunately, near this longitude it is possible to approach the singularity very closely without ill effect, e.g., at Eureka (L = 3373) the fitting error is 0.5 degrees in magnitude. For this reason, although it should not be hard to eliminate the singularity, no attempt has been made to do so.

The coefficients used in the program have been chosen by fitting individual parts of the algorithm by hand. It is very likely that an optimization of coefficients using a nonlinear least squares fitter could improve the residuals. However, the residuals are already negligible as far as modeling is concerned.

2.5 Trough Detection by Satellite Tracking

There is one effective technique for locating the trough which has not been used in the HILION modeling effort. This is the use of a two-frequency tracking of a beacon satellite. Presuming an instrument which receives at a UHF frequency (u) and a VHF frequency (v), it is known that the phase rate ($\dot{\phi}$) difference

$$\dot{\phi}_{VHF} - \frac{v}{u} \, \dot{\phi}_{UHF}$$

is proportional to the (time) rate of change of total electron density along the ray path. Presuming that the ionosphere does not change significantly as the ray path passes through the region of interest — an assumption that is good for a ten-degree wide trough in the presence of a short period medium scale TID ($\tau \gtrsim 10$ min) — the time derivative of total content may be converted to a latitude derivative. The relationship between time and latitude depends on the apparent motion of the satellite, which is a very smooth function.

There is a major difference between trough detection by monitoring phase rate data and trough detection by monitoring N_m data from a topside sounder. The N_m data shows the deepest point in the trough directly, and the trough walls indirectly (by differentiation of N_m with respect to latitude). The phase rate data, however, shows the trough walls directly and the trough bottom is found by integration.

Since the walls of the trough are narrow and steep, the center of the trough wall is easy to detect. Figure 2-24(A) depicts the range error rate (which is proportional to the VHF-UHF phase rate) as obtained from a ray tracing calculation by

2-58

B. Range Error

A. Range Error Rate
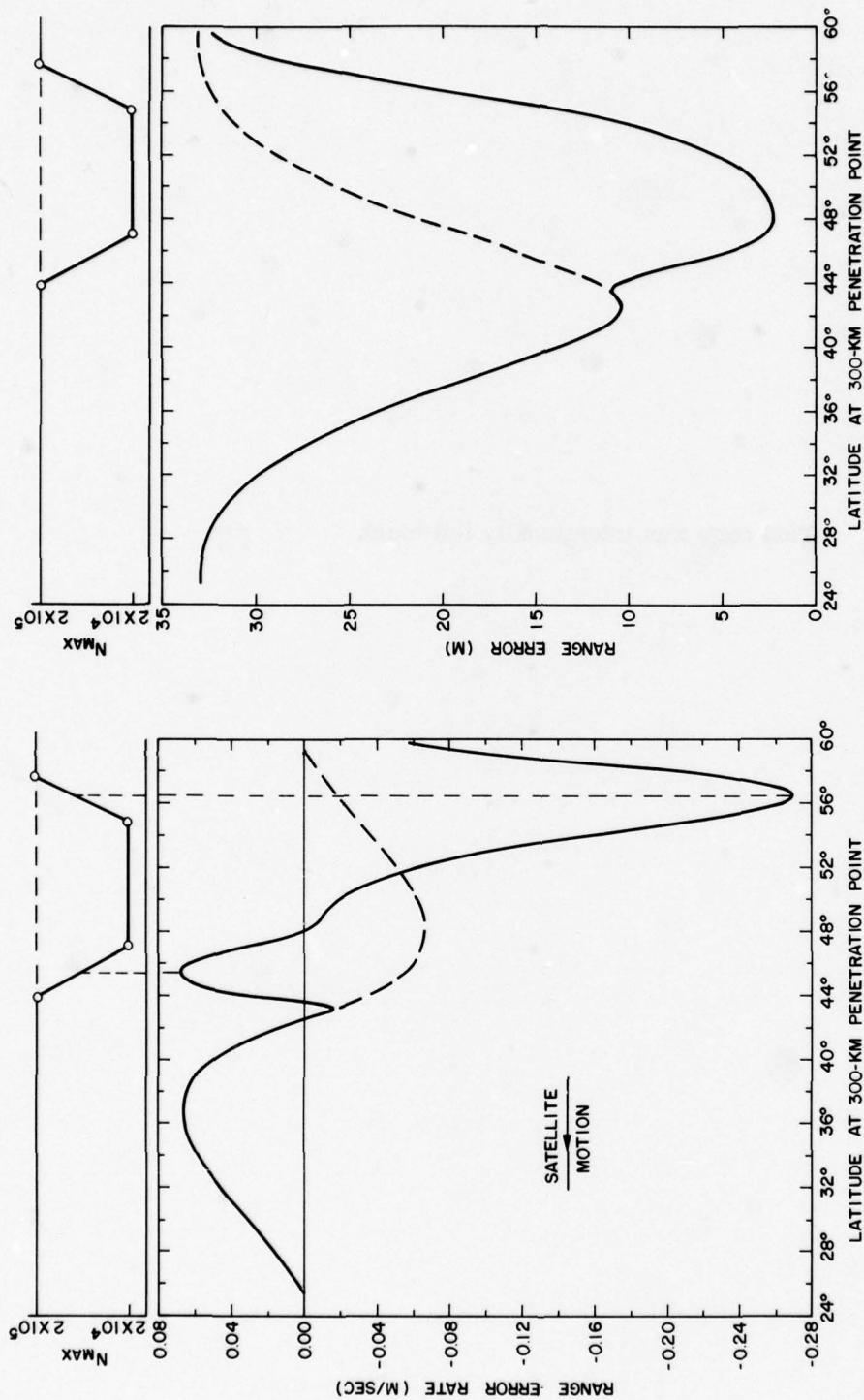
Figure 2-24. Numerical Simulation of Errors in Tracking a Southbound Satellite in an Overhead Trajectory for a Spherically Stratified Ionosphere (Dashed Curves) and for an Ionosphere With a Trough (Solid Curves)

This page was intentionally left blank.

D. C. Badura. The dashed range error curve (which coincides with the solid curve south of 42 degrees) is the range error rate for a spherically stratified 50-km scale height Chapman layer. The non-constancy of the error rate is due to the varying elevation angle of the radar beam. The solid curve is the range error rate in the presence of the trough illustrated in the figure. The extrema of the curve are the extrema of the combination of the range error rate due to a spherically-stratified ionosphere (the "ambient" ionosphere) and the range error rate due to the gradients of N_m in the walls. The latter effect is so much sharper than the former, that the extrema created by the trough walls may be considered (to a good enough approximation) to be due only to the trough walls and not to the ambient ionosphere.

The deepest part of the trough is harder to obtain. It is possible to integrate the phase rate curve, but the width of the trough bottom (in contrast to the width of the trough walls) is large enough that a detailed subtraction of the ambient effects is necessitated [Figure 2-24(B)]. Alternatively, the trough may be assumed to be symmetric and the point midway between the walls determined.

The above considerations are complicated by the presence of noise in real data. For best results, a smoothing of the data to remove variations over a scale of less than one degree is probably necessary.

2.6 Model of the High-Latitude Trough*

2.6.1 Introduction. A trough (region of sharply decreased electron densities) has been found to exist on the night side of the earth at invariant latitudes of roughly 60°N. Another trough exists in the southern hemisphere, but it will not be discussed further here. The trough was discussed extensively by Muldrew [1965] after an investigation of critical frequency data taken from the ionosonde (topside sounder) aboard the Alouette I satellite. Sudden depressions in electron density have been observed from the ground; nevertheless, the latitudinal scans available only from mobile ionosondes seem essential to an understanding of the trough. Muldrew [1965] and Thomas and Andrews [1968] point out the correlation of the position of the trough with the footprint in the F region of the plasmapause (Carpenter's [1963] 'knee'). By restricting themselves to deep, sharply-defined trough observations, Tulanay and Sayers [1971] have compiled a wealth of statistics on the trough (in both hemispheres).

The present investigation is based on data obtained from the Alouette I and II satellites. It differs from other studies by using full electron-density profiles to find correlations between other F layer features and the trough. It also differs in

*This section describes work performed during the editing of the previous part of this document. Some of the points made in Section 2.3.3 have been refined. In particular Figure 2-22 has been extended in Figure 2-25 and Figure 2-23 has been extended and modified in Figure 2-29.

that it seeks the trough even when it is weak or ill-defined. Thus, in contrast to the Tulanay and Sayers [1971] study, a large percentage of the satellite passes produced data interpreted as trough cross sections; indeed, it is believed that under certain easily defined conditions a satellite will observe the trough with essentially 100 percent probability (if these conditions are not met, the trough will not be observed).

In slightly simplified form, the rule for determining whether a given sounding of the ionosphere (i.e., above a point p on the earth's surface at time t) observes the trough is as follows. Let χ_h be the solar zenith angle measured at p at time t - h hrs (called the lagged zenith angle). There are then 300-km invariant latitudes Λ_A and Λ_D and critical lagged zenith angles χ_c and χ_d such that

if:

    A.   The 300-km invariant latitude of p is between Λ_A and Λ_D.

    B.   t is before local midnight (at p) and $\chi_1 > \chi_c$, or t is at or after local midnight and $\chi_2 > \chi_d$

    then: the trough will be above p (or within the ±2 degrees residual scatter of being directly above p); otherwise, it will not.

Here "trough" is understood to mean the entire region of depressed electron densities including the trough walls.

The quantities Λ_A and Λ_D are functions of local time and magnetic activity (as measured, e.g., by the index K_p). χ_c depends on K_p only and χ_d is a constant. To a good approximation, none of the four quantities depends on season.

2.6.2 <u>Data base</u>. Alouette I and II N(h) (real height) data was modeled into vertical electron-density profiles. A total of almost 34,000 profiles could be modeled and were in the geographic region of interest (north of 30°N geographic latitude). The following parameters derived from these profiles were scatter plotted against 300-km invariant latitude: the F2 peak electron density, the altitude of the F2 peak, the (Chapman) scale height and its gradient at the F2 peak, and the (Chapman) scale height 300 km above the F2 peak. The following quantities describing the geographical environment were similarly plotted: the local time, the geographic longitude, the daily Zurich sunspot number (R_z), the solar zenith angle at the place and time of each ionospheric sounding, and the solar zenith angle at the place of each sounding 2.1 hours prior to the sounding. The 2.1-hour lag was taken from a preliminary study of the location of the trough. Near dawn and dusk, the lagged zenith angle was studied for amounts of lag varying from 0.5 to 3 hours in steps of 0.5 hr.

The data were partitioned simultaneously into ten local time bins, four season bins, two sunspot number bins, and seven bins of the three-hourly magnetic activity index (K_p) pertaining to the time of the ionospheric sounding or seven bins

of lagged K_p ($\overline{K}_p$, the value of K_p at the immediately-preceding four o'clock). Thus, $10 \times 4 \times 2 \times (7 + 7) = 1120$ data bins were examined, and — for the non-empty bins — plotted. The lagged-K_p binning was done in an attempt to reduce the scatter of the data. It appears to have helped for low K_p, but other factors are more important. (More often than not, the sorting by lagged or by unlagged K_p values both put an item of data in the same bin.)

2.6.3 <u>Nighttime peak electron densities</u>. There are two classes of observed data relevant to the study of the trough. One class is the behavior of the peak density and its correlation with the geophysical environment. The other class is the set of cross correlations between the trough as observed in the peak density data and the other parameters of the electron-density profiles.

During the fall and winter night, the trough is very pronounced and very well resolved in invariant latitude from 22:00 to 06:00. Indeed, for $K_p < 2$, there is a region near 60° invariant latitude not less than 5 degrees wide in which the electron densities are smaller than the typical values just to the south (about 1.4×10^5 e/cc) by a factor of 2 or more. However, this is not to suggest that the trough is only 5 degrees wide. From the southern edge of the south wall to the northern edge of the north wall the trough region is about 14 to 18 degrees wide (see Table 2-5), and has a depth such that trough densities are equal to the midlatitude densities divided by a factor of about 5 to 10. (The trough depth will always be specified in terms of this factor.) For $\overline{K}_p < 1$, the southern wall consumes about 7 or 8 degrees of the total width, while for $1 \le \overline{K}_p < 2$ this width drops to 3 to 5 degrees. Sorting by real time K_p does not show this steepening effect. The north wall is about 2 to 4 degrees for both K_p ranges. The southern boundary of the south wall moves from 47 ± 2 degrees at midnight to 53 ± 2 degrees at 09:00. Figures 2-25 and 2-26 summarize the winter trough morphology.

For spring and summer months, the trough is never so clearly defined. Even in the 00:00 to 04:00 time period, there are satellite passes which exhibit no recognizable trough. These extreme passes occur for longitudes near 0° where the invariant latitude is approximately equal to the geographic latitude. Most of the data comes from longitudes between 45°W and 90°W where the invariant latitude is 13 to 15 degrees greater than the geographic latitude. Consequently, the satellite passes exhibiting the trough observed locations which left the sunlit hemisphere at an earlier local time than the few which exhibit no trough. The trough may be about as deep as it is in the fall and winter at its most pronounced, but any shallower amount is also possible. The electron densities north of the trough (and therefore the height of the north wall as well) are larger in these months than in the winter. The trough region is slightly farther south than it is in the winter. The southern wall is not displaced at midnight, but is 1 ± 2 degrees to the south of its wintertime position

Table 2-5

TROUGH WALL LOCATIONS FOR LONGITUDES BETWEEN 45°W AND 90°W

Season	Wall	Quantity*	04:00	06:00	10:00 to 14:00	18:00	18:30	20:00	24:00
Spring	North	Λ	63 ± 1	ABSENT	ABSENT	ABSENT	(ABSENT)	64.5 ± 1†‡	66 ± 2†
		s	NO DATA					-0.6 ± 1.8	NO DATA
	South	Λ	51 ± 2†	ABSENT	ABSENT	ABSENT	(ABSENT)	[interpretation unclear]	48 ± 1† [2 +0 / -2]
		s	NO DATA						
Summer	North	Λ	(<63)	ABSENT	ABSENT	ABSENT	ABSENT	(ABSENT)	65 ± 1¶
		s	0 ± 1						-0.8 ± 0.8
	South	Λ	52 ± 2†	ABSENT	ABSENT	ABSENT	ABSENT	(ABSENT)	48 ± 2
		s	-1.2 ± 0.8						(0)
Fall	North	Λ	67 ± 3	70 ± 3‡	ABSENT	75 ± 1	(71)	68 ± 2	67 ± 1
		s	-1.1 ± 0.4	0 ± 0.5		-1 ± 1	[-1.2 ± 0.7]	[-2 ± 1]	[-1 ± 0.6]
	South	Λ	52 ± 2	52 ± 3	ABSENT	71 ± 1†‡	<58‡	(47)	47 ± 2
		s	-1 ± 0.6	0.9 ± 0.9		-4 ± 2§	NO DATA	(0)	(0)
Winter	North	Λ	67 ± 1	72 ± 2	ABSENT	74 ± 1	71 ± 2	67.5 ± 1	67 ± 1
		s	-1.7 ± 0.7	-1.9 ± 0.5		-2.5 ± 0.5	-0.9 ± 0.6	[-2 ± 1]	-0.8 ± 0.5
	South	Λ	54 ± 2	53 ± 3‡	ABSENT	68 ± 1‡	58 ± 3‡	47 ± 3	47 ± 2
		s	-1.3 ± 0.7	0 ± 0.5		NO DATA	-4.2 ± 0.6	0 ± 0.5	0 ± 0.5

* Λ is tabulated at $0 \leq \overline{K}_p < 1$ except if marked with an †. Lagged K_p is used for low K_p; real time K_p is used if it exceeds 3.

† At $1 < \overline{K}_p < 2$.

‡ Limited by χ.

§ Appears to increase in value markedly for large K_p.

¶ Limited by χ for high K_p (3 to 4) but not for low $\overline{K}_p$ (0 to 2).

( ) Model interpolation used.

[ ] Uncertain due to little or variable data.
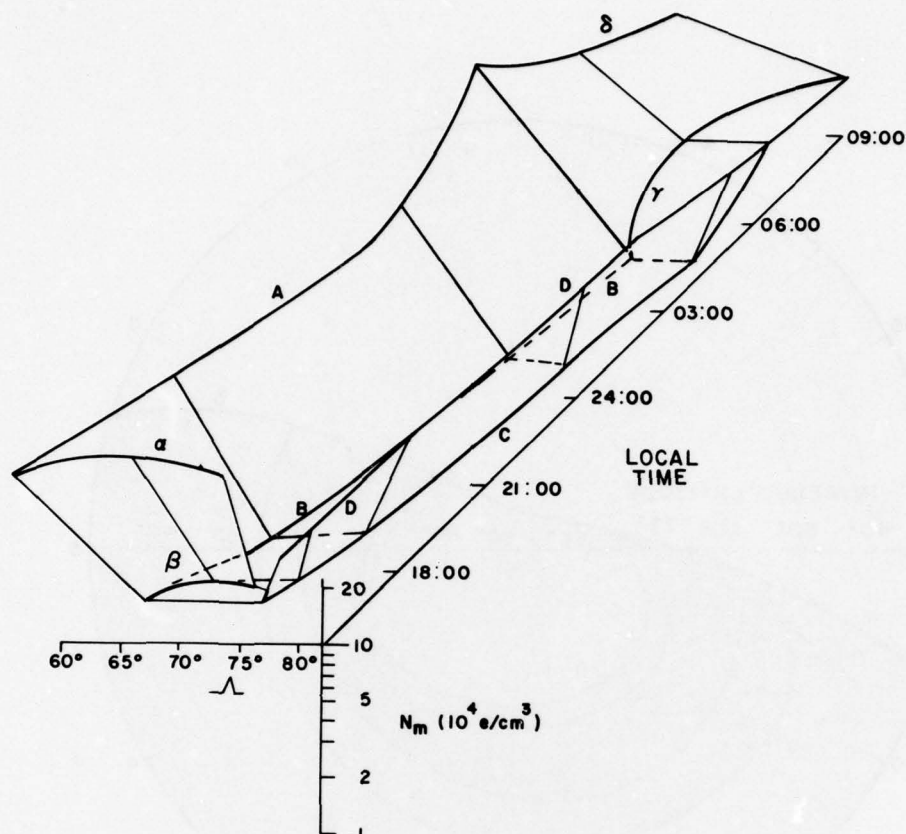
The curves labeled A, B, C, and D represent:

    A. The southern edge of the south wall

    B. The southern edge of the bottom

    C. The northern edge of the bottom

    D. The northern edge of the north wall.

Curves L and β are boundaries of the trough wall and bottom, respectively, due to solar illumination at dusk. Curves γ and δ are the similar boundaries which occur at dawn. The cross sections illustrated correspond to local times of 18:00, 18:30, 20:00, 22:00, 06:00, just before 08:00, 08:45, and 09:30.

Figure 2-25. Winter Trough

2-65

The curve labels are the same as those used in Figure 2-25. Curves α and β use the model critical zenith angles for a day (January 30) and longitude (70°W) that best represents the actual data. Curves γ and δ are similarly selected. They apply to January 20 and 70°W. The lightest shaded area satisfies the zenith angle criteria. The next darker area corresponds to the trough walls. The darkest area corresponds to the trough bottom.

Figure 2-26. Trough Boundary Data For Winter

at 04:00. The north wall is similarly displaced by an amount which varies from 0 at midnight to 4 ± 3 degrees at 04:00 also to the south. The slope of the walls is more gradual than in winter and a clearly-defined bottom is not observed for $\overline{K}_p < 1$. For $1 \le \overline{K}_p < 2$, the trough seems to be more clearly defined and the walls typically meet at the bottom of the trough.

2.6.4 Dusk. Near dawn and dusk, none of the scatter plots obtained is meaningful unless the individual satellite passes are examined. The grouping of the seasons into "fall through winter" and "spring through summer" still holds at dusk. In the winter, the trough forms at about 17:00 with its deepest point at 73 to 75 degrees invariant latitude. The entire trough region when first observed is less than 5 degrees wide; the depth is a factor of 1.5 to 2. It is V-shaped (the two walls meet and there is no bottom region) and symmetric. At 18:00 it has moved to 68 to 74 degrees depending strongly on $\overline{K}_p$ [cf. Thomas and Andrews, 1968] and has deepened to a factor of 5. The width has increased to roughly 6 degrees, and a bottom of about 2 degrees width has developed. At 19:00 a pass is observed with the trough bottom extending from 65 to 68.5 degrees; the full extents of the trough region are not definitely observed, but are south of 62 degrees for the southern-most latitude and probably about 71 degrees for the northernmost. By 20:00 the trough is well developed. The southern end of the south wall is at 47 ± 3 degrees, about as far south as it ever gets. The width of the south wall is about 5 degrees. The trough bottom extends north to 63 to 65 degrees and the north wall extends to 67 to 68 degrees.

The fall dusk period is generally similar to winter dusk, but there are some differences. On several passes between 14:00 and 16:00, the trough was observed with characteristics typical (in both fall and winter data) of the 17:00-to-18:00-period. The longitudes were between 10°E and 45°W. The geographic latitudes were higher than for most of the data (generally over Eastern U.S. longitudes). One satellite pass was in particularly flagrant disagreement with the others. The local time on the pass varied from 17:00 (south) to 16:30 (north), yet it observed the trough to extend from 60 degrees to north of 68 degrees (where the pass ended). However, the longitude of the pass varied from 165°W (south) to 180° (north); the geographic latitudes were thus well to the north of the other passes. Except for these few differences, the fall and winter dusk data agree within the indicated un-certainties.

During the spring, the trough is first observed at 20:00, at least for $1 \le \overline{K}_p < 2$. The single pass at that local time with $\overline{K}_p < 1$ suggests that a weak trough is observed at that level of magnetic activity, but this is inconclusive. At 21:00, the north wall is only 1 to 2 degrees wide. The observed minimum is at $63 \pm 1/2$ degrees (for longitudes from 50 to 90°W). The depth varies between

2-67

factors of 1.5 and 10 and seems to depend as strongly on longitude as local time (or is simply very variable). The south wall was definitely observed on only one pass; it was at 61 degrees. This pass is not understood and is inconsistant with all the data from higher K_p bins. The electron densities to the south of the trough tend to be about twice as high as those to the immediate north (this is not true for $\overline{K}_p < 1$). The depth is highly variable, but is seldom greater than a factor of about 2 for $\overline{K}_p < 1$. Between 21:00 and 22:00 the trough appears from 58 degrees or farther south to 72 ± 2 degrees. The south wall has such a gradual slope that its southern edge is ill-defined. The data is too sparse for a determination of the north wall thickness. Thus, at or very near to its earliest time of observation the trough has essentially its full width and has its north wall about 3 degrees north of its late-night position. Presumably, from 22:00 and 24:00 the trough simply moves south, but no data were available for this time, season, and magnetic activity to permit a check.

Summer data for this local time period is very sparse. The southern edge of the south wall is at 52 to 54 degrees between 21:00 and 22:00. The wall is about 5 degrees wide. The northern edge of the bottom is north of 67 degrees by 22:00.

2.6.5 Dawn. During the dawn, a marked difference between fall and winter occurs. In the winter, the trough is observed at more northern latitudes as the sun rises. At 06:00 the southernmost boundary of the trough region is near 53 degrees, having moved very slowly north during the night. The northernmost boundary of the trough is at about 72 degrees. The southern trough wall is about 5 degrees wide, which makes it a little less steep than it is during the night since the trough depth is a factor of 4 to 5. The southern boundary of the north wall occurs in a region where no data were taken. As the sun rises, the electron density just to the south of the trough rises from 1.5×10^5 e/cm^3 (the nighttime value) to 3×10^5 e/cm^3 at 08:00. The southernmost trough boundary does not move between 06:00 and almost 08:00, but the electron density there rises with the values to the immediate south. The southern end of the trough bottom moves from 57 ± 2 degrees at 06:00 to 65 ± 2 degrees at 08:00. The northern end of the trough bottom occurs in a region of little data, but is at approximately 71 degrees and shows little or no change with time. The northern boundary of the north wall remains essentially fixed at 74 ± 2 degrees. The trough bottom is not filled in during this period; consequently, the trough depth increases. It should be noted that the southern wall becomes very wide during this period. One satellite pass at 08:00 observed the southern wall to extend from 53 degrees (3×10^5 e/cm^3) to about 68 degrees (2.2×10^4 e/cm^3) (interpolation was used to estimate the values for a missing data point).

Between 08:00 and 10:00 the trough becomes filled in. In the latitude region from 65 to 70 degrees (just south of the trough north wall), there is no satellite pass

with a local time between 07:15 and 08:00. It appears that during this time period the trough south wall reaches the north wall and the trough depth begins to decrease rapidly. By 08:00 the trough south wall has a very weak slope; this makes its southern edge difficult to identify. The positions chosen were obtained with the aid of the critical zenith angle χ_c defined in Section 2.6.1 in selecting which break in the general slope (typically from two choices) to accept as the actual edge. At 08:30 the southern edge of the trough is at 64 ± 3 degrees. The trough bottom is about 1 degree wide and is near 72 degrees (i.e., essentially where the north edge of the bottom had been for an hour or more). The northern edge of the north wall is at 75 ± 1 degree, essentially unmoved. The electron densities at the bottom of the trough are near 10^5 e/cm^3, while the auroral region densities range from 10^5 to 2×10^5 e/cm^3. By 09:00 all that remains of the trough is a weak decline in electron density in the region from about 67 to 70 degrees followed by a more or less constant density of about 1.5×10^5 e/cm^3. At 75 degrees, where the north wall had been, the electron densities may increase, decrease, or remain the same on entry into the auroral region.

One atypical satellite pass occurred. The data from this pass was sparse, but it corresponded more with the data in the 04:00 to 06:00 time bin than with other data taken at 08:00, the approximate time of the pass. This pass occurred at 180 degrees longitude where, as has already been noted, a given invariant latitude implies a higher geographic latitude than it does in the more plentiful data from 45°W to 90°W.

The fall data is completely different from the winter data at dawn. Before 06:00, the trough is observed to be rather typical of both fall and winter night in position and depth. The southern edge of the equatorward wall has migrated north slightly, to 52 ± 3 degrees. The northern edge of the north wall is at 71 ± 2 degrees. However, during the period from about 06:30 to 07:15, the trough is filled in uniformly and vanishes. There is no evidence of motion of the trough walls during this period. During the same period, the electron density level to the south of the trough increases from about 1.5×10^5 e/cm^3 to 3.4×10^5 e/cm^3.

During the spring dawn, the trough moves to the south, in total contrast to the general motion which causes the trough to appear at higher latitudes during the daytime than it does during the night. It appears that spring dawn conditions for the trough begin between 02:00 and 06:00, depending strongly on the month. For those months (between March 1 and May 31) for which the Alouette satellites were orbiting near local dawn, dawn conditions appear to start shortly before 03:00 during a time period for which no data was taken. At 03:00 the trough region extends from 48 ± 2 degrees to 66 ± 1 degrees. The southern boundary of the trough bottom is at 50 ± 1 degrees. The trough depth is variable between a factor of 3 and 6. By 04:00

the northern edge of the north wall has moved south to 63 ± 1 degrees. The trough is V-shaped and has a minimum density at 58 ± 1 degrees. The depth is very variable; factors of 2 and 6 have both been observed. The southern edge of the south wall has migrated north slightly to 51 ± 2 degrees. From 04:00 until shortly after 05:00 the trough is filled in with, perhaps, a small (~1 degree) southward motion of the north edge of the north wall. After 05:00 there is no sign of the trough.

Summer dawn data is very sparse. The few passes yielding data in this bin give peak density curves which could be merged indistinguishably with the spring-time data. However, the times are confused. One pass at 01:00 (at 160°W longitude) exhibited no indication of the trough. Another pass at 04:30 (and 100°W longitude) found the trough to be well developed, to have a 5-degree wide bottm, and to be a factor of 3 deep. A third pass, at 05:30 (at 95°W longitude) observes what seems to be a virtually filled trough or (except for the trough-like latitude range) a very minor depression caused by the noise in the data all tending to have one sign over an interval.

2.6.6 <u>Solar zenith angle</u>. The data are much better organized if one considers the solar position. Preliminary studies of the data suggested a solar involvement at both dawn and dusk. It also appeared likely that the solar zenith angle was relevant, but not the zenith angle pertaining to the instant of ionospheric sounding. Rather, the zenith angle at the location of the sounding but some hours earlier seemed most relevant. Consequently, plots were made of the lagged zenith angle for the dawn and dusk periods. Examination of the lagged zenith angle shows that for the dawn period, the trough is only found where the 2-hr lagged zenith angle exceeds $\chi_d = 104 \pm 0.5$ degrees. No evidence was found for a dependence of χ_d on K_p. For χ_d to decrease by more than about 0.3 degrees per unit K_p would be inconsistant with the data. The 2-hr lag is chosen because it minimizes the uncertainty in χ_d. Almost equally small uncertainties were obtained with lags of 1.5 and 2.5 hr (but with differing values for χ_d). A change of more than 1/2 hr in the lag causes marked increase in the uncertainty. The zenith-angle criterion, together with the geometry of the seasonal motions of the earth's axis explain why the trough has an apparent motion at dawn to the north in the late fall and winter (see Figures 2-25 and 2-26), to the south in the middle or late spring, and none in the early or middle fall. It also predicts that the summer trough apparent motions should be essentially the same as the spring ones.

The concept of a critical lagged zenith angle also applies to the dusk period. One hr (again $\pm 1/2$ hr) is the optimal amount of lag. The critical one-hour lagged zenith angle χ_c is 97 ± 2 degrees for $\overline{K}_p < 1$. Unlike the dawn critical zenith angle, there is a significant magnetic activity sensitivity. For high K_p, the real-time

value appears to be more significant than the lagged value. Consequently, when the real-time K_p exceeds a value (arbitrarily chosen to be 3), it is used. With this definition, χ_c decreases by 3.7 ± 0.4 degrees per unit K_p. This sensitivity is large enough to account for virtually all of the variability observed in the dusk critical zenith angle.

2.6.7 <u>Trough boundaries.</u> The satisfaction of the two zenith angle criteria of the previous section form necessary but not sufficient conditions for the trough to lie over a given location (at a given time). Two other conditions are that the 300-km invariant latitude exceed a value Λ_A and be less than another value Λ_D. With the exception of a period surrounding the summer solstice (and it is suspected a local time period near noon, near the winter solstice, over the eastern hemisphere) these four conditions are sufficient for the presence of the trough. Discussion of the exceptional periods is deferred until a later section.

For very low K_p (0+, the center of the $0 \leq \overline{K}_p < 1$ bin) the dependence of Λ_A and Λ_D on local time is depicted by curves A and D respectively in Figure 2-27. These curves do not depend on season. The sensitivity to magnetic activity is listed for certain time in Table 2-5. The sensitivity used in the table is defined as $\delta\Lambda/\delta K_p$, where Λ denotes Λ_A or Λ_D as appropriate, and σK_p is calculated presuming that differences of the form $K_p - \overline{K}_p$ are valid (i.e., it is presumed that the average of $\overline{K}_p$ over many years for all prriods during which $K_p = k$ is also k and that the converse, with K_p and $\overline{K}_p$ interchanged, is true). Only those entires where the trough wall is not located by solar position are relevant here.

It was found that Λ_A is independent of K_p from about 20:00 until some time between 00:00 and 04:00. Prior to 20:00 and during the early morning there is a weak dependence on K_p. In contrast, Λ_D does exhibit a K_p dependence throughout the night, averaging just under 1.5 degrees per unit K_p. The sensitivity to K_p is not uniform, but is greater near 18:00 and after about 04:00 than in the middle of the night. A corresponding K_p study of Λ_B and Λ_C was not done, but it has been determined that the trough bottom moves southward relative to the average of Λ_A and Λ_D. This shift is approximately 1/2 degree per unit K_p. Such an effect is not unexpected because the electron densities in the auroral zone are greater at high K_p than at low K_p while the trough bottom densities do not rise. For a given latitudinal gradient of peak electron density, the north wall width must increase. During most of the night the trough bottom moves approximately $1/2 + 1/2 (0 + 1.5) = 1.2°$ per unit K_p.

This figure is smaller than the 2 degree per unit K_p obtained from Muldrew's [1965] data (after correcting an error in the fitting procedure) which seems to be generally accepted. It is decreased somewhat further by the dawn insensitivity of

2-71

LOCAL TIME
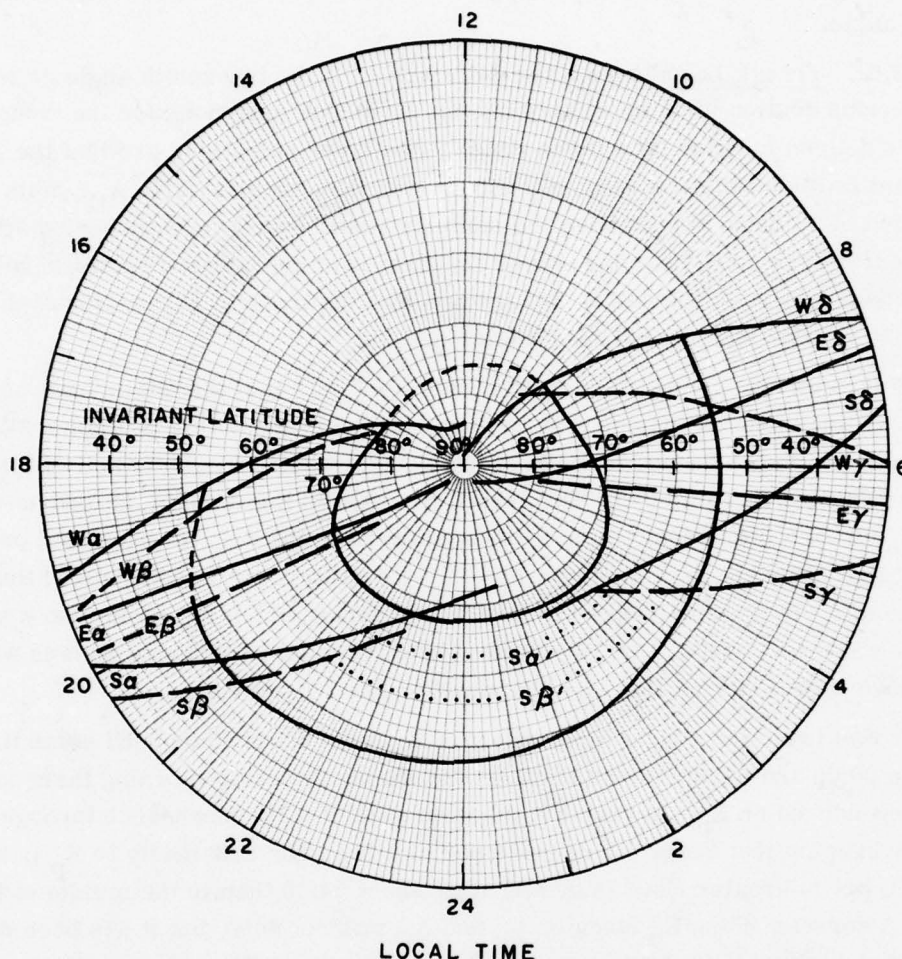
The letters α, β, γ, δ, A, and D have the same significance as in Figures 2-25 and 2-26. The letters W, E, S denote the season: W — winter solstice, E — equinox (vernal or autumnal), and S — summer solstice. The curves Sα' and Sβ' denote the effect of the requirement that the trough (bottom) must be formed by 22:00 (21:40) if it is to be formed at all. Curves A and D are independent of season. Curves B and C are omitted for clarity but are located as in Figure 2-26.

Figure 2-27. Model Predictions of Trough Boundaries
for all Seasons at 77°W Longitude

one trough wall to K_p due to the lack of dependence of χ_d on K_p. However, it is increased markedly by the high sensitivity (3.7 degrees per unit K_p) of χ_c to K_p. Since a change of more than 1 degree in latitude (2 degrees is fairly typical) is required to change the solar zenith angle by 1 degree, there is very high sensitivity of one trough wall to K_p during a period which is of the order of two hours long (depending on season). This period can easily increase the average sensitivity over the whole night by 1/2 degree or more (depending strongly on the distribution of the data in both local time and season), eliminating the discrepancy.

2.6.8 <u>Other trough-related ionospheric features.</u> There are trough-related features in each of the following parameters: altitude of the F2 peak, scale height at the peak, scale height gradient at the peak, and scale height 300 km above the peak. Specifically seasonal effects were noticed only in the topside scale height data, but it is very important whether or not a given trough wall was caused by the sun being at a critical zenith angle. When a trough wall is the result of solar illumination, the only parameter which exhibits trough-related values is the peak density itself. All other parameters assume values typical of the mid latitude region (at the south wall) or the auroral region (at the north wall).

Since two sets of data (each with noise) are being compared, there is somewhat more uncertainty in locating features than there is in the peak-density data. The altitude of the peak is the most scattered of all of the parameters studies. A lot of the scatter may be due to interactions of winds with the longitudinal variation of the declination of magnitude field lines, thus driving plasma up the field lines at some longitudes and down the field lines at others [Nisbet, 1973*]. However, there are also fluctuations of approximately ±15 km which appear to be noise, and real structure which can change the peak altitude by ±100 km or more from its average for a given pass. Variations in the latitude of these features enhance the scatter in the data. There is an increase in the height of the F2 peak of 50 to 100 km centered on the southern trough wall. The southern end of the altitude enhancement is roughly coincident with the southern end of the south wall (±3 degrees). The northern end of the enhanced altitudes is in the region of the trough bottom and has been observed at both extremes of the trough bottom. It moves to the north (relative to the trough) with increasing K_p.

The scale height at the peak exhibits an increase at the trough. South of the trough region, 37 ± 7 km is a typical scale height. Toward the center of the trough bottom, scale heights of 60 ± 8 km are found. Immediately to the north of the trough (from 0 to 3 degrees north of the northern end of the trough wall) the scale heights drop to about 40 ± 10 km and then begin an increase into the auroral zone. The

---

*Private communication.

southern boundary of the scale-height enhancement is 0 to 2 degrees north of the southern edge of the south wall. On the average (but not for any single satellite pass) the scale-height enhancement has a shape similar to a Gaussian function. The enhanced scale heights are found even when the solar illumination is forming one of the trough walls, but it is compressed in latitude to avoid the illuminated region.

2.6.9 <u>Scale-height gradient</u>. At night, the scale height gradient is nearly constant at 0.12 ± 0.015 km/km at night south of the trough. About 3 or 4 degrees north of the southern edge of the south wall this near constancy breaks up into an irregular variation. There is some tendency for the scale-height gradient to increase in the south wall and decrease in the trough bottom, but there are numerous exceptions. North of the trough, the gradient is quite irregular, with an average value of about 0.08 ± 0.09 km/km. In the afternoon and early evening in the mid-latitude region (including the trough south wall if illuminated) the scale-height gradient is even more constant than during the night; its value is then 0.10 ± 0.01 km/km. During the day, the indicated uncertainty is almost entirely due to variations between passes while at night there are fluctuations within the data from each pass of comparable magnitude to the variations between passes.

2.6.10 <u>Topside scale height</u>. The scale height 300 km above the F2 peak (topside scale height) is not a simple extrapolation of the scale height and scale-height gradient at the peak. Just south of the trough region the topside scale height exhibits a marked seasonal dependence. In the fall and winter it is about 130 ± 10 km at night, while during the spring and summer 90 ± 20 km is more typical. At the southern edge of the south wall (± 2 degrees) the topside scale height increases its value by about 30 km in fall and winter; somewhat less in spring and summer. The variability increases to at least ± 30 km. Data from a typical satellite pass shows a modest (10 to 20 km) enhancement in scale height with one or two spikes of 40 to 50 km amplitude and 1 to 4 degrees width. The spikes are variable in latitude from 2 degrees south of the southern edge to about 8 degrees north of the southern edge of the south wall. On the average the topside scale height climbs about 30 km in 3 to 5 degrees near the southern boundary of the trough region. Proceeding north, the topside scale height drops throughout the trough region, becoming 80 ± 20 km at the northern edge of the north wall. A very meager amount of spring and summer data indicates a more gradual decrease so that, at the northern edge of the north wall, the scale height averages about 90 km in these seasons. The spring and summer auroral-zone topside scale heights are larger than the corresponding winter ones. Increasing magnetic activity tends to decrease the magnitude of the topside scale-height enhancement.

2.6.11 <u>Miscellaneous data</u>. Several miscellaneous observations (not all of which are new) are needed for an understanding of the trough. The trough is found

in the intersection of two regions: (1) the region where the solar zenith angle (lagged as appropriate) exceeds the critical lagged zenith angle appropriate to the local time sector (i.e., dawn or dusk), and (2) a region which is approximately at the foot of the magnetic field lines forming the plasmapause (biased slightly to the south). The position of the latter region is a function of local time but not (with one possible exception) of season. The possible exception is for $1 \leq \overline{K}_p < 2$ in the time period from 20:00 to 20:30 during the spring, as described in a previous section.

There are two other critical zenith-angle conditions which delimit the boundaries of the trough bottom as χ_c and χ_d delimit the extremities of the walls: (1) during the dawn period, a given location cannot be under the trough bottom unless the (real time) zenith angle ($\chi \equiv \chi_o$) exceeds $\chi_e = 95 \pm 2$ degrees and (2) during the dusk period, it takes about 20 minutes at any latitude for the electron densities to drop from mid-latitude or auroral values (depending on season) to trough-bottom densities. In the notation used for the other critical zenith angles, the condition is that $\chi_{1.33} > \chi_c$ for trough bottom densities to be observed.

It is important to note that the correlation of the trough position with the plasmapause breaks down during the period from 19:00 to 21:00. The plasmapause moves out about 1 earth radius at moderate K_p (2-4) [Carpenter, 1966] which corresponds to a northward motion of its footprint by about 5 degrees compared with the preceding and following periods. The trough motion in that time period corresponds only roughly to this pattern. The plasmapause bulge does correspond with the time that the trough is formed. The local time at which the bulge is encountered is 16:30 to 17:00 at moderate K_p; allowing for a width of $\pm 1/2$ earth radius, the effects of the bulge can first be encountered at about 16:00 to 16:30 (note that the leading edge of the bulge is nearly radial [Carpenter, 1966, Brice, 1967].

It is also apparent from the data that the trough does not continue to grow deeper and more pronounced throughout the night. Rather, within about two hours of creation, the trough seems to have become as pronounced as it ever will (over a given location and for a given night).

It is worth recalling that there is another similar phenomenon at approximately the same latitudes but at higher altitudes — the light ion trough. This is a region where H^+ and H_e^+ ions are depleted and, consequently, above about 1000 km (where H^+ is the dominant ion) there is also an electron depletion. Unlike the electron-density trough which is the subject of this investigation, the light ion trough is found in the daytime as well as the nighttime.

2-75

2.6.12 <u>Model of trough formation.</u> With the information now available, it is possible to describe a trough formation mechanism which is based on plausible physical processes and which seems to describe the data quite well.

It seems clear, and has been suggested by many authors from <u>Muldrew</u> [1965] on, that the trough is connected in some fashion with the plasmapause. One way in which this could occur is by provocation of an instability due to the shear in the plasma velocity at the plasmapause. When it occurs, such an instability can evacuate electrons and ions from the shear region. The evacuation of the high-altitude portion of a flux tube leads to evacuation at lower altitudes, because plasma at lower altitudes will rise with the reduction of the pressure above it. This simple mechanism can explain the light ion trough, but it is not adequate to explain the evacuation of flux tubes down to the F2 peak.

At the very high altitudes (several earth radii) where there is a high shear velocity, the only ions present in quantity are H^+ and He^+. However, at F region heights O^+ is dominant, indeed, below 600 km or so the amount of H^+ and He^+ is negligible. Thus the equilibrium configuration consists of a light ion layer "floating" on top of the O^+ layer. Evacuation of the flux tubes at their greatest altitude will not alter this configuration. Consequently, such an evacuation will not affect any significant number of O^+ ions.

It is therefore necessary to trigger an instability at altitudes where a significant amount of O^+ is present. It is also necessary that the triggering occur at a time when the solar zenith angle is sufficiently large, for otherwise solar ionization could compete successfully with the combined depletion mechanisms of the instability and recombination. It is probably not necessary to trigger an instability at altitudes where there is much O^+ because once the O^+ ions begin to migrate upward they must be replaced at the bottom of the layer by something else. Because of the slowness of cross-field diffusion for charged particles it will be neutrals (probably O) which do the migration. This addition of O under the O^+ helps an upward flow of O^+ to develop. Such an upward motion lifts the F2 layer and should also increase the scale height at the F2 peak (both of these effects were observed). These effects increase the amount of O^+ at high altitudes and therefore increase the rate of removal of the electrons and ions from the flux tubes.

Since the local times at which the trough can first be observed (17:00-22:00 at low $\overline{K}_p$ over the Western Hemisphere — see Figure 2-26) corresponds to the local time period during which the plasmapause is found at the largest L-shells (the evening bulge — see Figure 2-29), the most plausible initial hypothesis is that both phenomena are manifestations of the same physical processes. The evening bulge results from the interaction of sunward-flowing plasma from the tail of the magnetosphere with the corotating plasma, which at 18:00 is flowing directly away from the

2-76

sun [Brice, 1967]. The motion of the sunward-flowing plasma causes the velocity shear across the plasmapause to be greatest, for any fixed altitude, during this period.

There is another effect which helps to destabilize the plasmapause. If one envisions, as a gedanken experiment, the tail plasma velocity to be increased from zero to the actual value, the first observable effect would be the creation of a small bulge in the plasmapause near the magnetic equator at a local time of about 17:00 by the mechanism discussed above. This breaks the azimuthal symmetry of the plasma-pause and reduces the critical velocity needed to provoke the Kelvin-Helmholtz in-stability. Since the amplitude of the oscillations caused by the instability in the plasmapause are limited mainly by the conductivity in the ionosphere at the ends of the flux tubes forming the plasmapause (see Figure 2-29), the bulge and instability ex-tend along the flux tubes to the top of the F2 layer. The effect of the plasmapause oscillation is to cause a fairly smooth decrease in electron density across the insta-bility with a smaller step in electron density occurring at the outer boundary of the instability. This outward displacement of the electron density step produces the ob-served form of the evening bulge in the plasmapause as indicated by the high L por-tion of the (dashed) envelope surrounding the unstable region in Figure 2-29. The plasmapause locus indicated in Figure 2-29 has been taken from Carpenter [1966] and applies to moderate magnetic activity ($2 \leq K_p \leq 4$). If one interpolates between the position of the plasmapause at 16:00 and at 23:00 (chain dotted line in Fig-ure 2-29) and then assumes that the plasmapause oscillations are radially sym-metric, an estimate can be constructed for the location of the inner boundary of the unstable region (low L dashed line in Figure 2-29). Between 18:00 and 20:00 this crude estimate of the inner boundary location agrees (after conversion to invariant latitude) with Λ_A to within 1 degree for $2 \leq \overline{K}_p \leq 3$. Consequently, it is possible to infer that the same instability is responsible for the trough and the observed large plasmapause bulge.

In order to obtain the very low electron densities observed in the trough, plasma leaves the unstable region. When it does so, most of the plasma should be deposited at the inner boundary of the instability because the plasma density is much higher inside the plasmapause than outside it. The observational evidence supports this suggestion, since there are very high scale heights at the southern edge of the south wall of the trough (Λ_A). These scale heights indicate a relatively high electron density at these latitudes (L shells) at the top of the F2 layer.

In the fall and winter (when the bulge region is entered at about the same time as the solar zenith angle criterion $X_1 > X_c$ is first satisfied) then trough appears early and becomes well defined and deep. In the spring and summer months, when $X_1 > X_c$ only after the bulge region has been entered, the trough is considerably

2-77

weaker and more poorly defined. Near the summer solstice (especially over Europe and Asia) the sun can remain sufficiently high that $X_1 > X_c$ at trough latitudes until after 22:00. Under these conditions no trough forms.

This picture of trough formation suggests that the trough parameters are determined by the conditions prevailing in the plasmapause bulge. Whenever solar effects do not interfere, the trough bottom occupies the full latitudinal extent of the unstable region and extends outward. In the ionosphere the northern trough wall is provided by particle precipitation into the auroral oval followed by diffusion up field lines from the E layer to the F2 layer, as described by Bates, et al. [1973]. Once the evacuation of ionization from the trough region is completed, the trough should propagate in local time by following L-shells. However, the L-shells which the trough follows do not correspond precisely to circles of invariant latitude. The real ionosphere, in contrast to the generally used models, is subject to a diurnal compression and nocturnal expansion. This effect accounts for the (non-solar zenith angle related) motion southward of the trough between 18:00 and 20:00, and northward after about midnight. Thus, it can be seen that there is no direct correlation between the trough latitude and plasmapause latitude after 21:00 or 22:00; the approximate correspondence between the two occurs because the plasmapause lies approximately along an L-shell.

Since the trough is caused by conditions in the plasmapause bulge, it is clear that if the trough has not begun to form over a given location by some time (before midnight) it will not form that night even if all of the conditions described thus far are satisfied at some later time. Taking the abovementioned time as 22:00 (the approximate time of the decay of the evening plasmapause instability) places an additional restriction on the possible extent of the trough region to the north which corresponds to just north of 62° N (invariant) at 77° W for the summer solstice. This brings a few summertime passes which had been inconsistent with the model into approximate agreement with it. (The exact day of the year for individual satellite passes was not preserved; consequently, a more precise determination of this cutoff time is not possible.) In Figures 2-27 and 2-28 the cutoff is depicted by the dotted curve labeled $S\alpha'$. A similar condition applies to the completion of trough formation. Placing the cutoff time for the satisfaction of $X_{1.33} > X_c$ 20 minutes earlier (i.e., at 21:40) gives the north wall of the abovementioned summer passes the correct width. In Figures 2-27 and 2-28, this limit is denoted by the dotted curve S_β'. In the eastern hemisphere, the cutoff latitudes are so far south that examination of data from a summer solstice pass at these longitudes is predicted not to show any noticeable trough, although the prediction indicates a very small dip about 3 degrees wide near 50 degrees. Considering the slopes of the trough walls, the indicated depth should be comparable with the noise in the data. Two satellite

2-78

passes were found at about 0° longitude. Neither pass exhibited a clear trough. One had a small dip at the prediction location; the other pass was missing a few data points at the predicted dip.

Examination of Figure 2-28 shows that very near the winter solstice in the eastern hemisphere there is no condition yet discussed which prevents a new trough from developing as soon as the trough from the previous night is filled in. The asymmetry between the dawn and dusk periods is, however, presumed to be due to the evening plasmapause instability (bulge). Therefore some other condition (which is normally automatically satisfied when the dusk solar zenith angle criterion is met) must exist which prohibits the trough from forming before the evening instability is encountered. Heuristically, this condition could be taken as a local time restriction such as $T > 15$, but none of the data which was examined occurred at the relevant local time, longitude and season.

The critical lagged solar zenith angles χ_c and χ_d do not have any direct physical significance. Rather, they summarize the effect of solar irradiation and perhaps other effects over a finite time. They measure the net excess of photoionization over all loss processes (including the trough-creating processes in the case of χ_c) integrated over a time period comparable with the amount of lag used. Since the various time derivatives of solar zenith angle vary with season and geographic latitude (and consequently with longitude for a fixed invariant latitude range), it is clear that there is no unique value for either χ_c or χ_d which can work perfectly. The effect of the first time derivative of solar zenith angle can be balanced by appropriate choice of lag; the presence of other terms gives rise to uncertainties in the critical angles.

2.6.13 <u>Summary and conclusions</u>. Examination of many electron-density profiles suggests that the trough is evacuated by a plasma instability related to the evening bulge in the plasmasphere. The evacuation process competes with solar photoionization. Around dawn, the trough is filled in by solar photoionization. If one regards a "day" as the time period from noon to noon, then by adding 24 hrs to all morning times, the trough may be located as follows.

The trough is found above a location at 300 km invariant latitude Λ, geographic longitude φ, and (geographic) local time T if and only if:

A. $\Lambda_A < \Lambda < \Lambda_D$ (see Figure 2-26 and Table 2-3);
B. $\chi[\Lambda, \varphi, \min (T,22) - 1 \text{ hr}] \geq 97 \pm 2° - (3.7 \pm 0.4°) (K_p - 1/3)$;
    if $T > 24:00$
    $\chi(\Lambda, \varphi, T - 2 \text{ hrs}) > 104 \pm 0.5°$.

LOCAL TIME
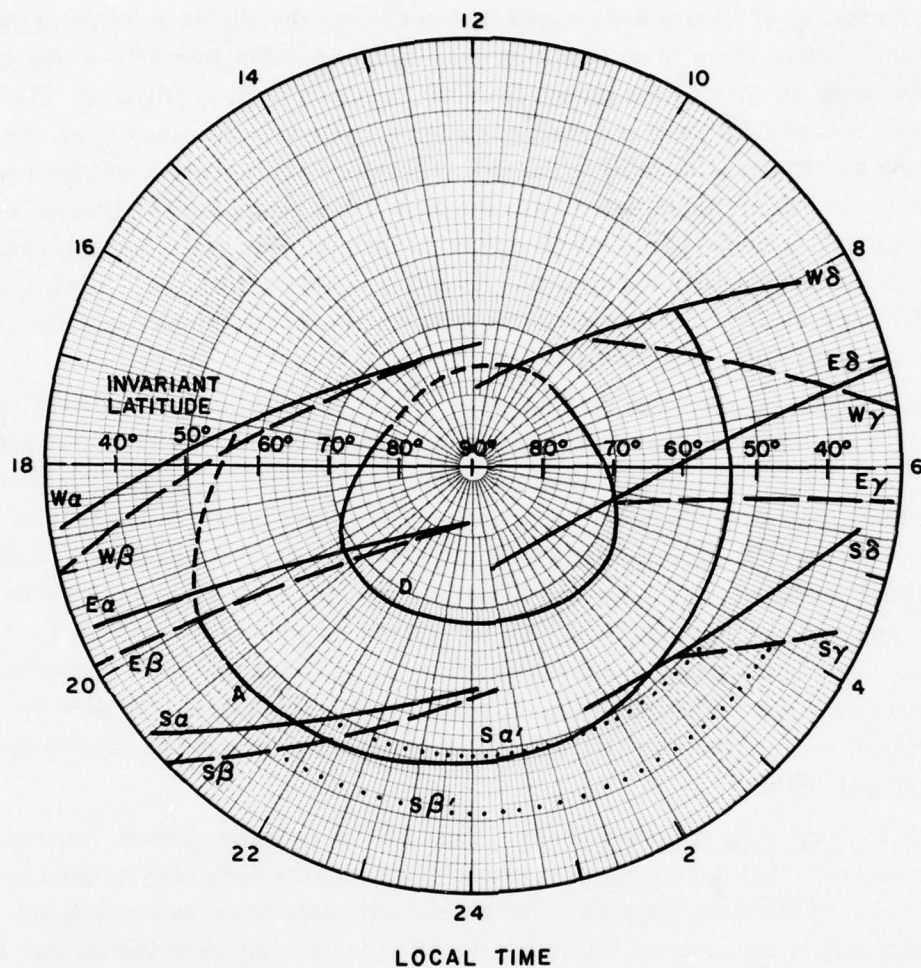
This figure is similar to Figure 2-27 except that the longitude is defined by the condition that the invariant and geographic latitudes be equal. This corresponds approximately to longitudes 150°W to 155°W and 5°W to 0°.

Figure 2-28. Model Predictions of Trough Boundaries for all Seasons at the Longitudes for which the Invariant and Geographic Latitudes are Equal
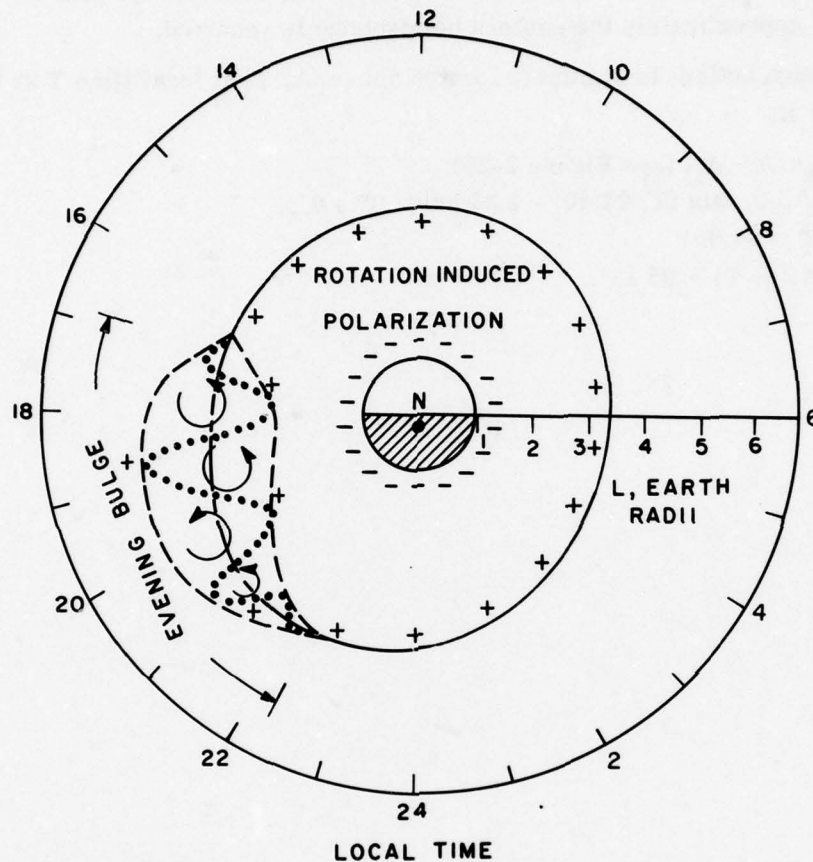
The outermost curve (solid and dashed) gives the position of the plasmapause for moderate K_p following <u>Carpenter</u> [1966]. The chain dotted curve is a graphic estimate of the position the plasmapause would have in the absence of an instability. The inner dashed curve locates the inner boundary of the unstable region. The dotted curve indicates schematically the appearance of the plasmapause at one instant in the presence of the instability. The plasma flow in the characteristic vortex street is also indicated. Ionized particles entering the evening bulge are believed to be redeposited on the inner boundary of the unstable region.

Figure 2-29. The Kelvin-Helmholtz Instability as the Cause of Both the Trough and the Evening Bulge in the Plasmapause

Note that the time at which the solar zenith angle is to be calculated is indicated explicitly as an argument in condition B. The use of the minimum function requires that the trough have been formed by 22:00 at the latest. It appears likely that a third condition, which would automatically be satisfied except near the winter solstice over approximately the eastern hemisphere is required.

The trough bottom is similarly located above (Λ, φ) at local time T at $\overline{K}_p = 0+$ if and only if:

A. $\Lambda_B < \Lambda < \Lambda_C$ (see Figure 2-26);
B. $\chi[\Lambda, \varphi, \min (T, 21:40) - 1.33 \text{ hr}] > 97 \pm 2°$;
   if $T > 24:00$
   $\chi(\Lambda, \varphi, T) > 95 \pm 2°$.

3. STATISTICS OF REGULAR IONOSPHERIC EFFECTS AT FT. CHURCHILL, 1968

3.1 Discussion

An investigation of the ordinary critical frequency (foF2) of the ionospheric F2-layer peak was completed using Ft. Churchill, Manitoba, ground-based ionosonde data for the year 1968, obtained from Canadian Ionospheric Data Churchill [1968]. The methods of observing the ionosphere by such equipment are described in a general review by K. Rawer and K. Suchy [1967]. The parameter foF2 is a measure of the peak electron density of the ionospheric F2-layer which determines ionospheric refraction effects. An analysis of this data therefore provides useful information for studies on ionospheric effects.

The following sections show some ionospheric group delay and refraction effects, the diurnal and seasonal variations of foF2, and the variations of the F2-layer peak electron densities for Ft. Churchill. A correlation study of foF2 with other geophysical parameters was also done to obtain a clearer determination of foF2 at least for this one location and year. As a result of that analysis some unusual behavior of foF2 was detected in relation to the planetary magnetic index, K_p. To study this an investigation was made of foF2 versus a "lagged K_p," i.e., versus K_p values obtained at times different from those of foF2.

3.2 Diurnal Variations

3.2.1 Background. D. C. Badura [1971] had made studies to determine the dependence of ionospheric range and elevation errors on elevation angle and target height. He assumed that the height (h) dependence of the ionospheric electron density over a spherical earth was represented by a single Chapman F2 layer (see Figure 3-1):

$$N = N_m \exp \left\{ \frac{1}{2} \left[1 - z - \exp (-z) \right] \right\} , \qquad (3-1)$$

where the normalized height parameter is

$$z = (h - h_m)/S .$$

He performed ray tracing through this model ionosphere for the case where

$$\text{maximum electron density} = N_m = 1.9 \times 10^6 \left(\frac{el}{cm^3} \right)$$

$$\text{height of the maximum} = h_m = 306 \text{ km, and}$$

$$\text{scale height} = S = 54 \text{ km,} \qquad (3-2)$$

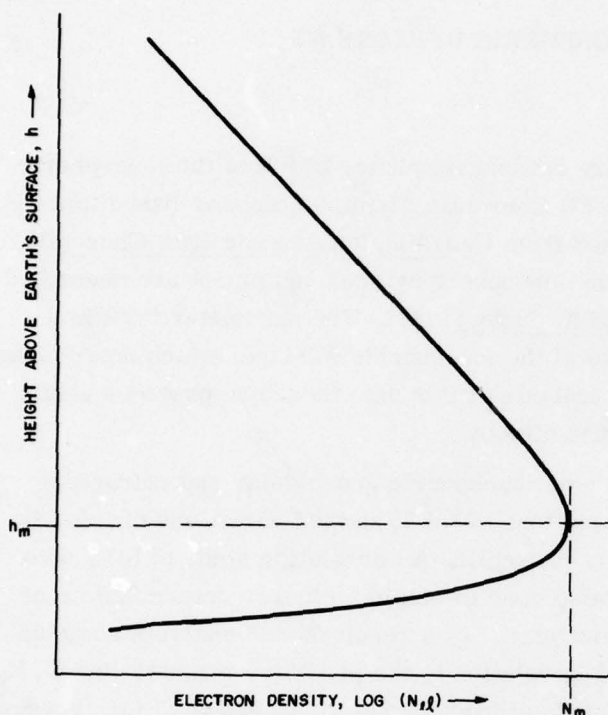and calculated the ionospheric refraction errors in range (DI) and in elevation (EI)

Figure 3-1. Chapman Function Describing a Single Ionospheric Electron-Density Layer

at a radar frequency of 435 MHz. The peak F2-layer electron density is related to foF2 by the equation

$$N_m = 1.242 \times 10^4 \left(\frac{\mathrm{foF2}}{\mathrm{MHz}}\right)^2 \left(\frac{\mathrm{el}}{\mathrm{cm}^3}\right) \qquad (3\text{-}3)$$

so that $\mathrm{foF2}^2 = 155 \ (\mathrm{MHz})^2$ for this case. J. H. W. Unger recognized that in this radar frequency region (f) the ionospheric errors are proportional to the peak electron density. The ionospheric errors DI and EI therefore can be normalized to this value of $\mathrm{foF2}^2$ producing the relations

$$K_D = \frac{DI}{\mathrm{foF2}^2} \quad \text{and} \qquad (3\text{-}4)$$

$$K_E = \frac{EI}{\mathrm{foF2}^2} \qquad (3\text{-}5)$$

These coefficients and their ratio K_E/K_D vary with both apparent elevation and target height (H_T) as shown in Figure 3-2. These relations may be used to estimate the ionospheric refraction effects of the assumed two-dimensional Chapman layer.

3.2.2 <u>Results</u>. Assuming the ionosphere (3-2) described above and that relation (3-4) would hold true for other ionospheres, an investigation was made of the

3-2

1.0
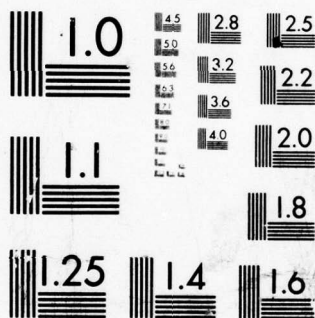
4.5
50
56
63

2.8

2.5

3.2

2.2

3.6

1.1

4.0

2.0

1.8

1.25

1.4

1.6
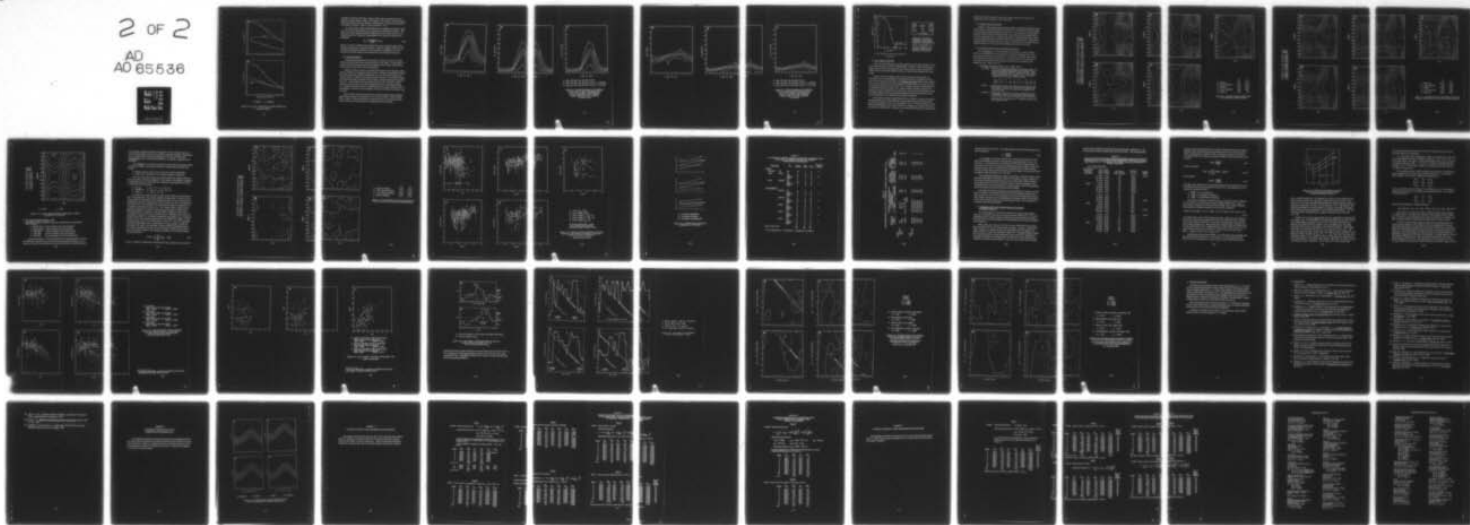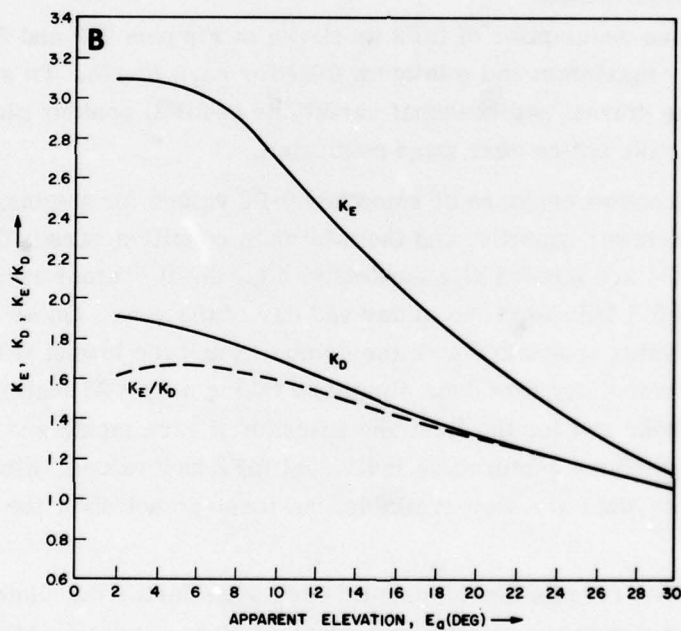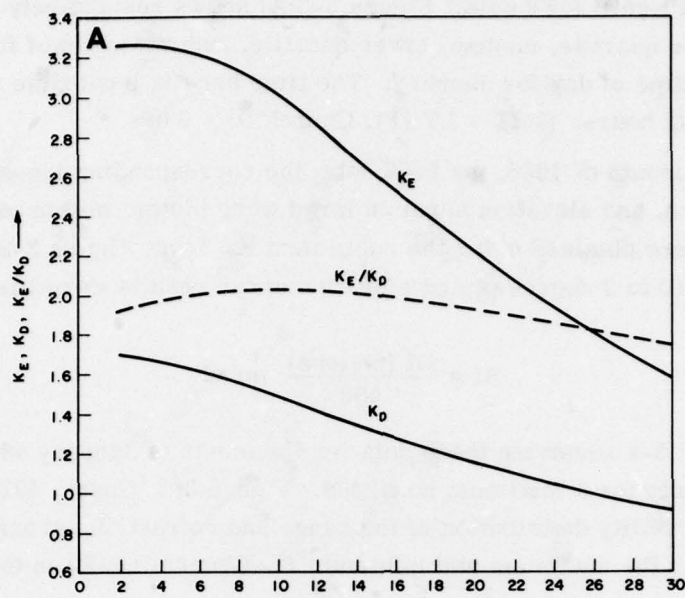
MICROCOPY RESOLUTION TEST CHART
NATIONAL BUREAU OF STANDARDS-1963-A

A. 500 km   B. 1000 km

Figure 3-2. K_D, K_E, and K_E/K_D for Target Heights (H_T)
of 500 and 1000 km

available Ft. Churchill foF2 data. Figure 3-3(A) shows respectively curves of maximum, upper quartile, median, lower quartile, and minimum of foF2 values observed versus time of day for January. The time here is local time which differs from GMT by six hours: GMT = LT (Ft. Churchill) + 6 hrs.

For each month of 1968, the foF2 data, the corresponding ionospheric range errors in meters, and elevation error in mrad were plotted in this manner. The range errors were obtained using the coefficient K_D from Figure 3-2(A) for low elevation angle (0 to 2 degrees), and elevation error results were based on the assumption

$$EI = \frac{DI \text{ (meters)}}{500} \text{ mrad .} \qquad (3-6)$$

Figures 3-3 and 3-4 illustrate these data for the month of January when foF2 is maximum and July for a minimum condition. Figure 3-5 [Unger, 1973] shows the cumulative probability distribution of the range and refraction errors for low elevation and for the maximum and minimum Ft. Churchill foF2 in that year.

3.3 Seasonal Variations

The previous description of foF2 as shown in Figures 3-3 and 3-4 reveals centers of hourly maximum and minimum foF2 for each month. To summarize in compact form the diurnal and seasonal variations of foF2, contour plots of these hourly values for the entire year were generated.

Figure 3-6 shows contours of smoothed foF2 values for the maximum, upper quartile, median, lower quartile, and the minimum condition versus GMT and month. The contour levels are labeled alphabetically, e.g., the H contour locates occurrences of foF2 = 5.5 MHz for time of day and day of the year. On all contour plots, the highest data value is marked with the symbol Δ and the lowest value is marked with a $\square$. The smoothing was done simply by taking a 27 × 27 matrix of foF2 values for each hour and for the first and fifteenth of each month and averaging 3 × 3 sequential sections centered on individual foF2 raw values. Similar plots of unsmoothed or raw data are also available, but these do not show the contour levels as clearly.

Figure 3-6(A) reveals a peak density occurring during the winter months of January and February in the afternoon — from 12:00 to 16:00 LT (18:00 to 22:00 GMT). Figure 3-6(E) shows periods of minimum foF2 for this location and year, during the fall and winter through local midnight until early morning.
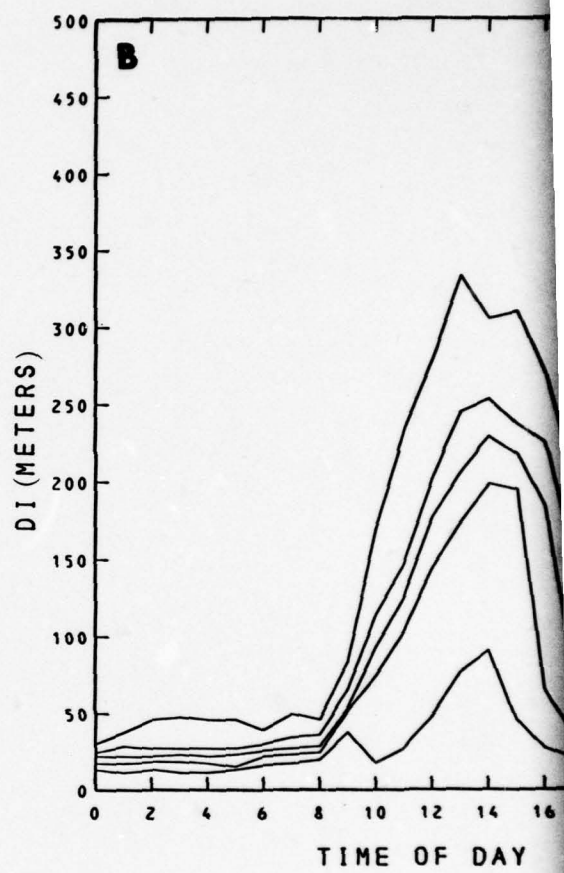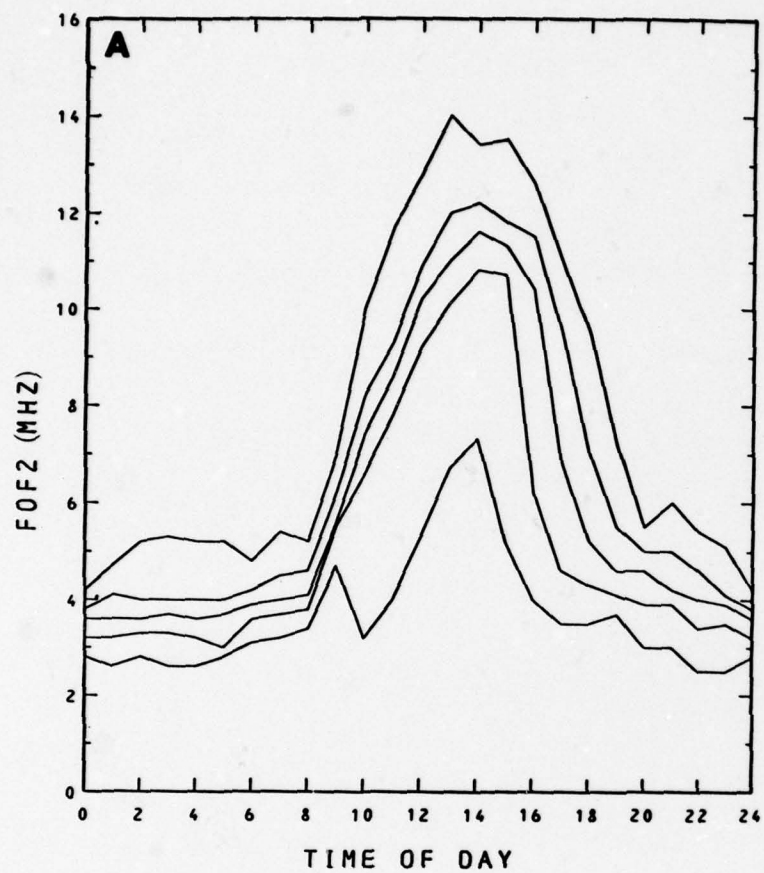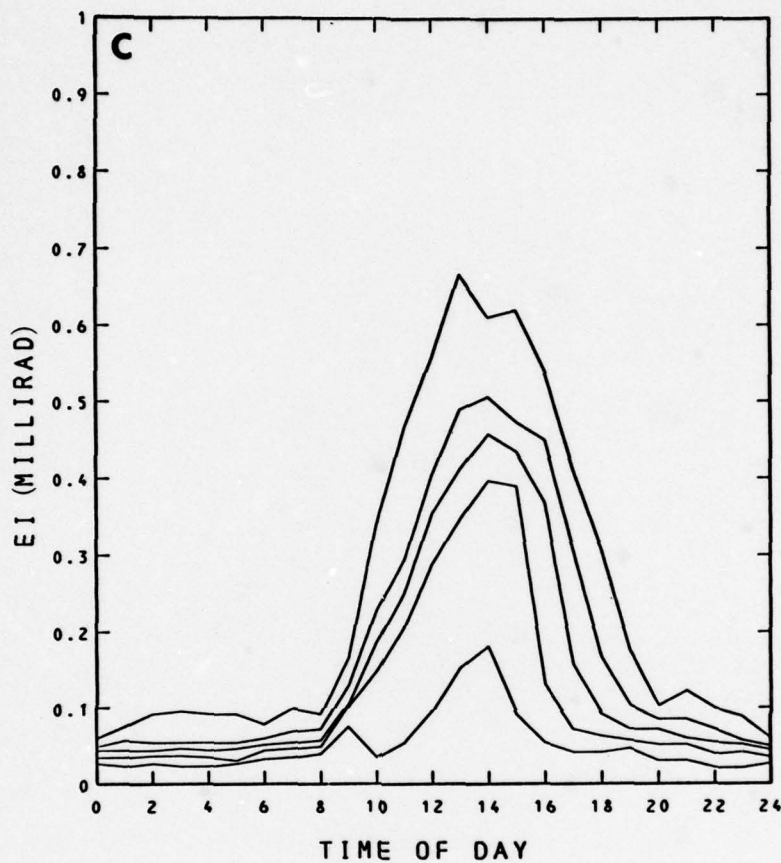
A. Max, UQ, Med, LQ, and Min of foF2

B. Max, UQ, Med, LQ, and Min of DI for F = 448 MHz

C. Max, UQ, Med, LQ, and Min of EI for F = 448 MHz

Figure 3-3. Critical Frequency of the Ordinary
F2 Wave (foF2 in MHz), Ionospheric Range
Error (DI in meters), and Ionospheric
Elevation Angle Error (EI in millirad)
versus Local Time at Ft. Churchill
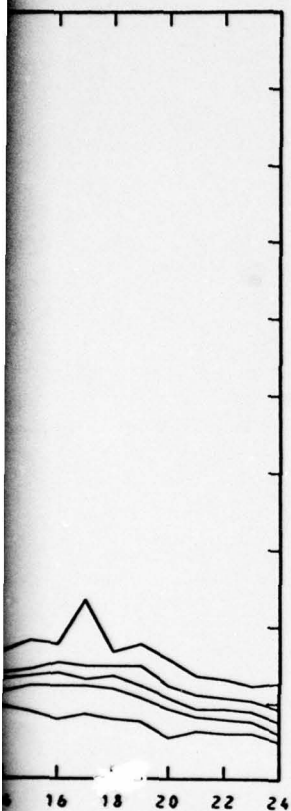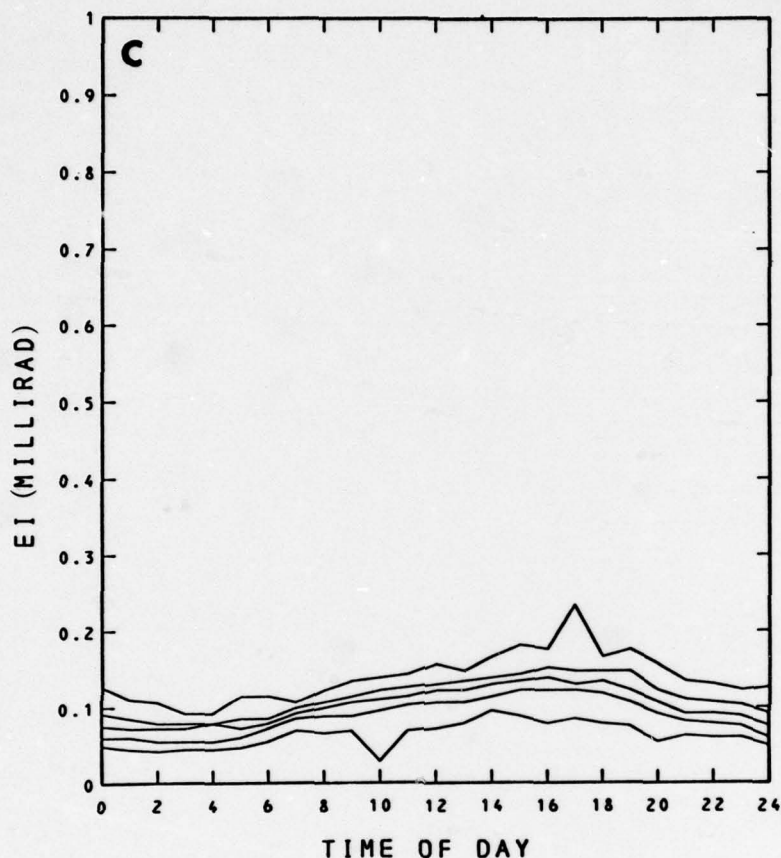in January 1968.
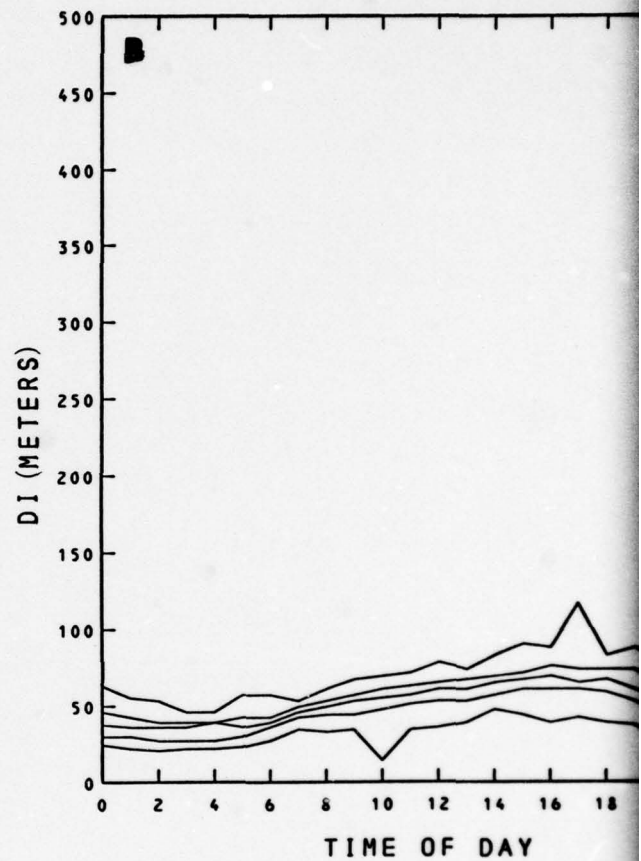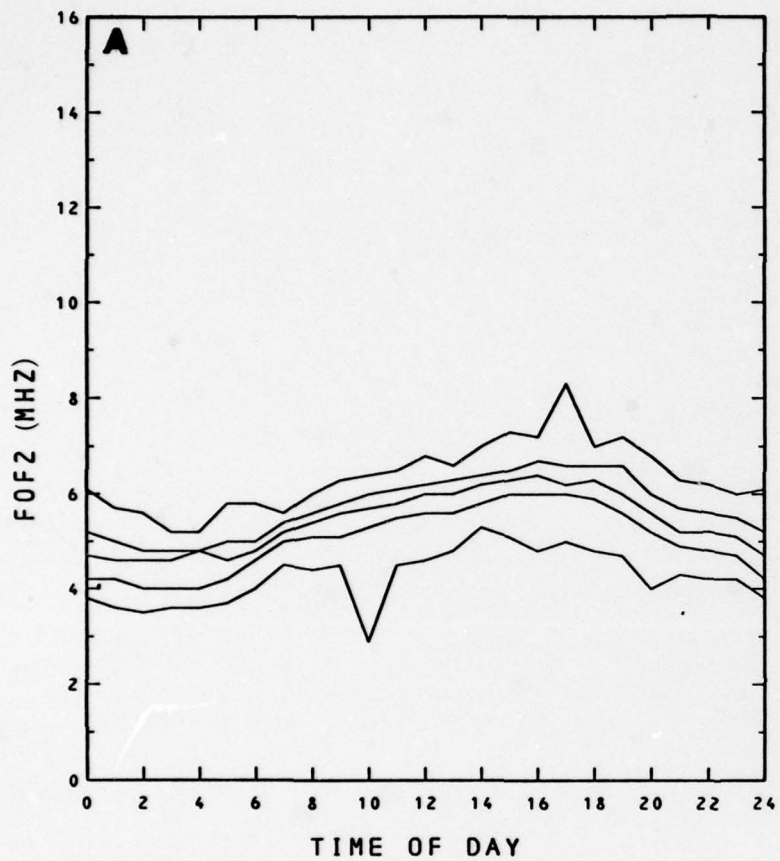
3-5

A. Max, UQ, Med, LQ, and Min of foF2

B. Max, UQ, Med, LQ, and Min of DI for F = 448 MHz

C. Max, UQ, Med, LQ, and Min of EI for F = 448 MHz

Figure 3-4. Critical Frequency of the Ordinary
F2 Wave (foF2 in MHz), Ionospheric Range
Error (DI in meters), and Ionospheric
Elevation Angle Error (EI in millirad)
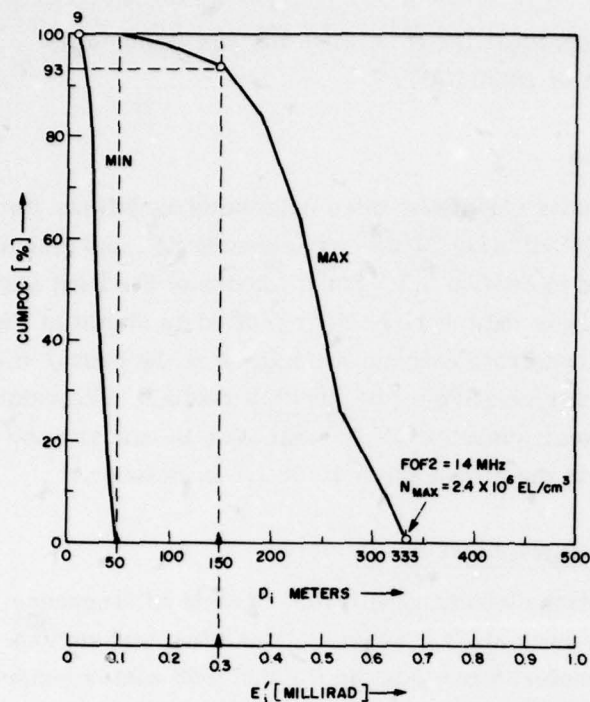versus Local Time at Ft. Churchill
in July 1968

3-7

9

100

93

80

60

CUMPOC [%]

40

MIN

MAX

20

FOF2 = 14 MHz
N_{MAX} = 2.4 X 10^6 EL/cm^3

0

0   50   100   150   200   300 333   400   500

D_i METERS ⟶

0   0.1   0.2   0.3   0.4   0.5   0.6   0.7   0.8   0.9   1.0

E_i' [MILLIRAD] ⟶

Ioniz. Level	Month	~ LT 90°W
Min.	Sep	04:00
Max.	Jan	15:00
F = 448 MHz		

Figure 3-5. Cumulative Probability of Occurrence (CUMPOC) of Ionospheric Range (D_i) and Angle Errors (E_i') for Long-Range Low-Elevation Targets for Ft. Churchill, 1968, Min and Max Hours of Ionization

3.4 Solar Influence and foF2

Figure 3-6 illustrates that a specific maximum for each foF2 condition occurs in the early afternoon at 14:00 (LT) (20:00 GMT). Figure 3-7 shows the maximum, upper quartile, median, lower quartile, and minimum ratios of the smoothed foF2 values to the value at 20:00 GMT for all hours of the first and fifteenth day of each month.

Figure 3-8 shows contours of the cosine of the solar zenith angle at Ft. Churchill for the first and fifteenth of each month which are computed from Equations (2-6 through 2-8) in Section 2.1.4 (Feinblum and Horan [1973]). These contours more closely resemble those of the relative foF2 values plotted in Figure 3-7 than the absolute foF2 values of Figure 3-6. The F contour of Figure 3-8 represents the Ft. Churchill sunrise or sunset. The J contour outlines the period when the sun reaches its annual culmination at Ft. Churchill. As can be seen from Figure 3-7(C), the median relative foF2 occurs during the beginning of July at 22:00 GMT, while the sun culminates at Ft. Churchill in mid June at 18:00 GMT.

This alternate method of describing foF2 (i.e., Figure 3-7) serves to diminish seasonal effects and to demonstrate the correspondence between the foF2 diurnal variations and changes in the solar zenith angle. A two- to three-hour delay in solar effects influencing parameters such as foF2 is not unusual and a similar time lag of four hours is exhibited here. Likewise, for the absolute foF2 values, the median total

3-9

[see Figure 3-6(C)] peaks two hours after the time when the sun reaches its highest point at Ft. Churchill, that is 18:00 GMT.

3.5 Electron Density Variations

Relative hourly electron density variations were calculated as follows for each foF2 condition: $(Max/Med)^2$, $(UQ/Med)^2$, $(LQ/Med)^2$, and $(Min/Med)^2$, and smoothed by the averaging method described in Section 3.3. For all hours of the first and fifteenth day of each month in 1968 these data were contour plotted as shown in Figure 3-9. These plots serve to demonstrate extreme variations of the hourly values of the F2-layer peak electron density relative to the monthly median. The relative maximum value of 2.7 was found near sunset at 18:00 local time in January and the relative minimum 0.25 was found in the afternoon at 15:00 LT in October.

3.6 Correlation of foF2 with Geographical Parameters

3.6.1 Background. Correlations between the ordinary critical frequency (foF2) of the ionospheric F2-layer peak at Ft. Churchill, Manitoba, and various local and global geophysical parameters were studied for the 1968 winter season when foF2 reaches a seasonal maximum. It was the purpose of this analysis to investigate the possibility of determining foF2 indirectly by measuring other geophysical data. These data were:

A. The Global Parameters [Essa 1969 , Valley 1965]
1. KP (K_p) — Three-hour planetary geomagnetic disturbance index. KP is the mean standardized K-index from 12 observatories between geomagnetic latitudes 47 and 63 degrees. This index of magnetic activity is scaled from 0 (very quiet) to 9 (extremely disturbed) in thirds of a unit. The usual ± nomenclature for K_p was coded as follows:

K_p	0	0^+	1^-	1	1^+	2^-	...	8^+	9^-	9
KP	0	3	7	10	13	17	...	83	87	90

2. DSSN — Daily Sunspot Number also known as Zurich Relative Sunspot Number. Index of the visible activity of the sun determined by the number and clusters of sunspots as observed each day.

3. DORFO — Daily Observed Radio Flux at Ottawa radiated by the sun at 2800 MHz. Numerical entries refer to a single measurement made near local noon at 17:00 GMT. The unit of measurement for the flux is 10^{-22} watts per square meter per cycle per second.

3-10

Contour
Levels

A = 2.0
B = 2.5
C = 3.0
D = 3.5
E = 4.0

F = 4.5
G = 5.0
H = 5.5
I = 6.0
J = 6.5

K = 7.0
L = 7.5
M = 8.0
N = 8.5
O = 9.0

P = 9.5
Q = 10.0
R = 10.5
S = 11.0
T = 11.5

U = 12.0
V = 12.5
W = 13.0
X = 13.5
Y = 14.0
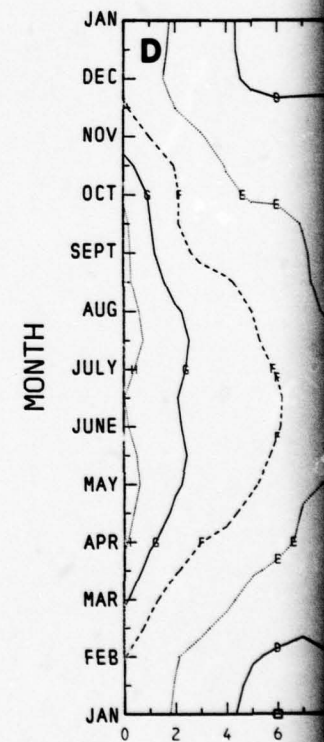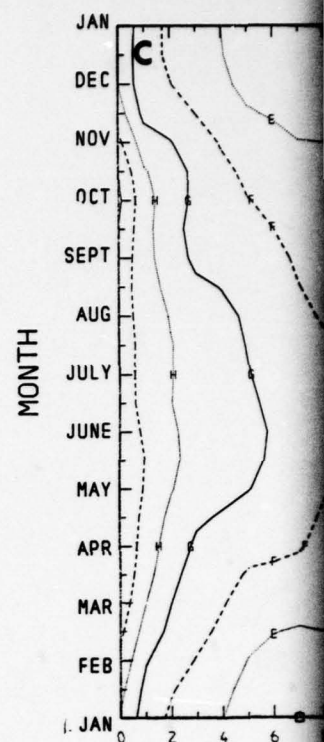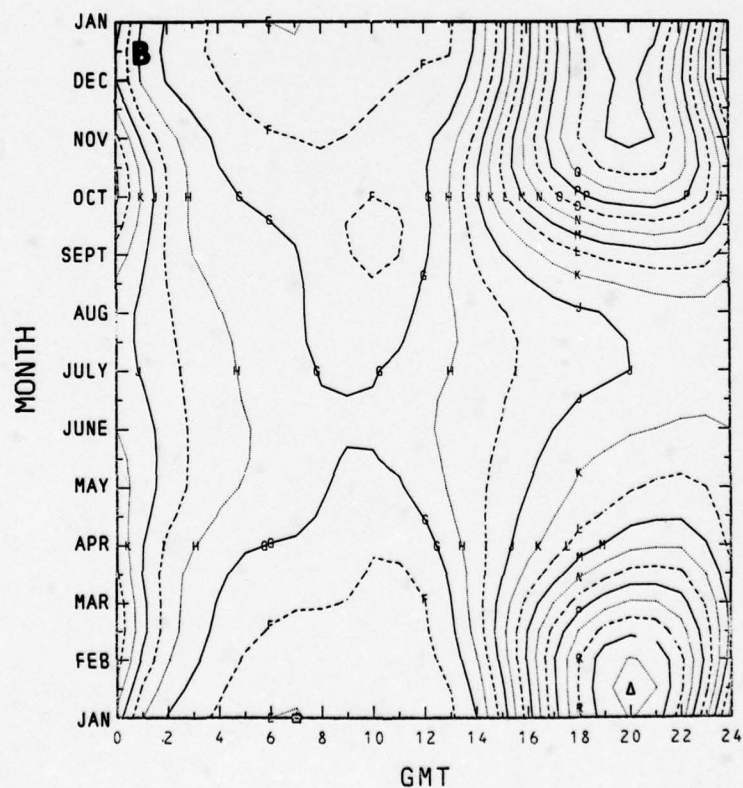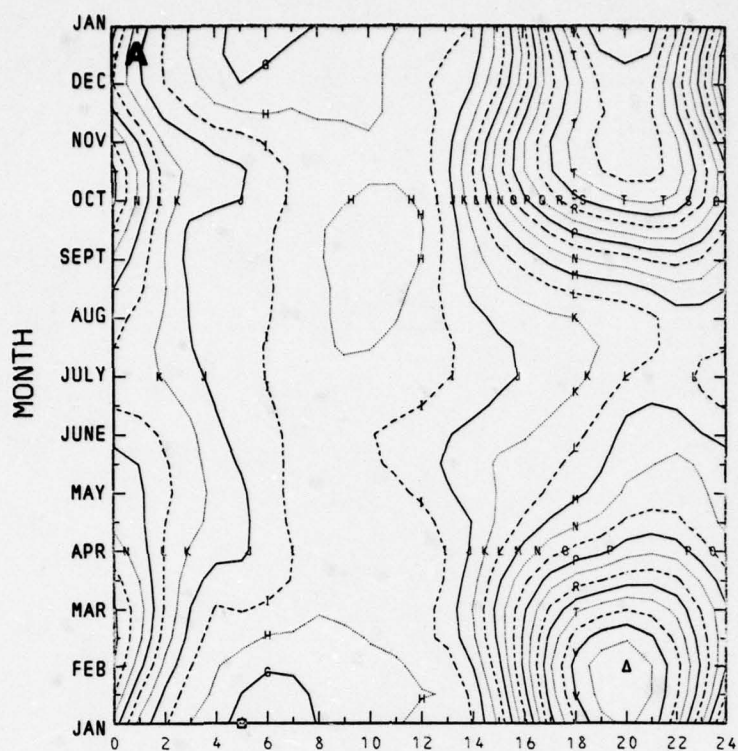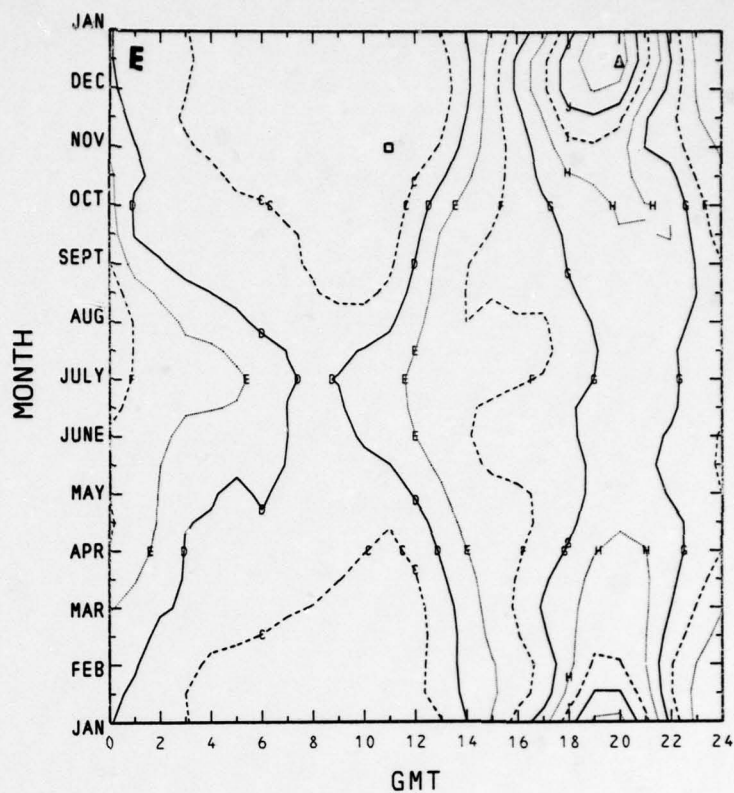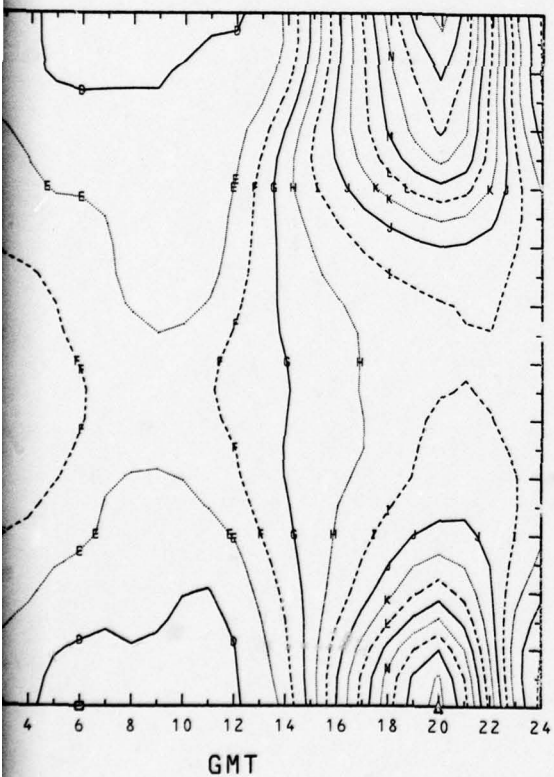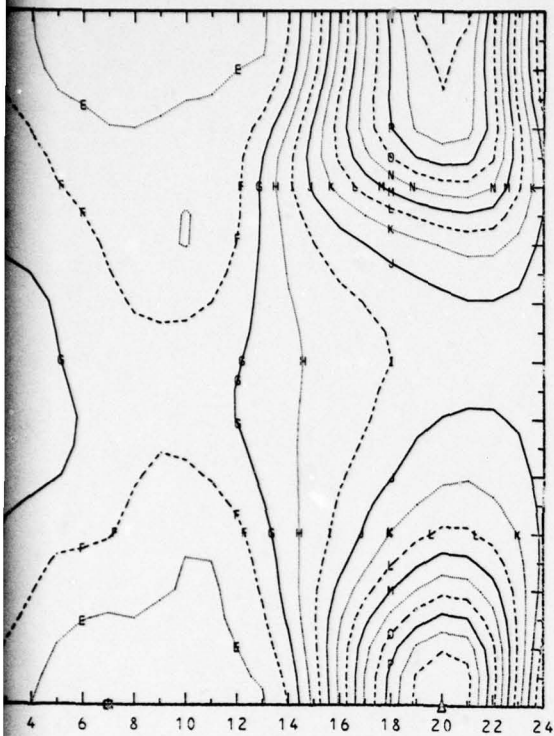
	□	△
A. Maxima	4.77	13.48
B. Upper Quartiles	3.98	11.69
C. Medians	3.62	10.95
D. Lower Quartiles	3.23	10.18
E. Minima	2.50	7.34

Figure 3-6. Smoothed Values of foF2 in MHz at Ft. Churchill vs GMT and Month
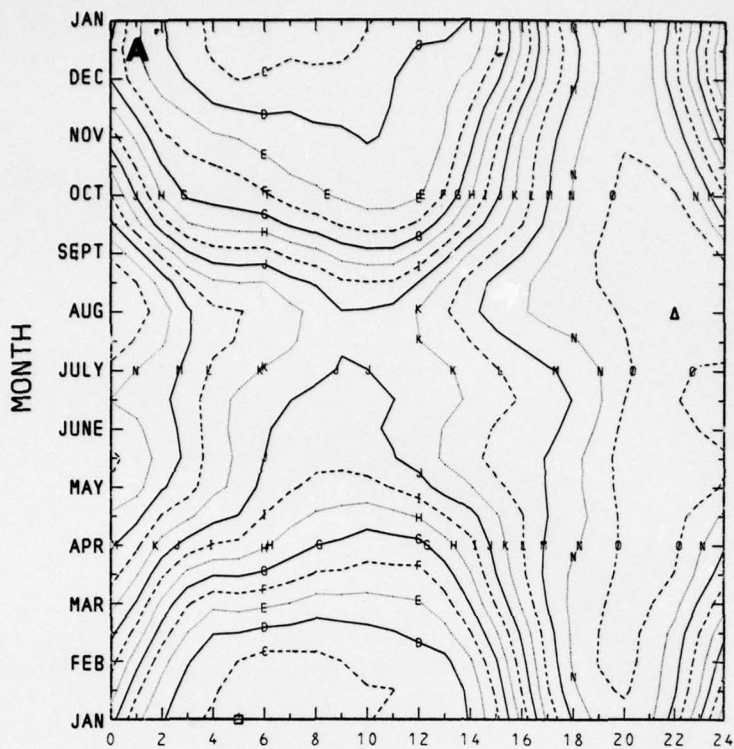
Contour
Levels

A = 0.30
B = 0.35
C = 0.40
D = 0.45
E = 0.50

F = 0.55
G = 0.60
H = 0.65
I = 0.70
J = 0.75

K = 0.80
L = 0.85
M = 0.90
N = 0.95
O = 1.00
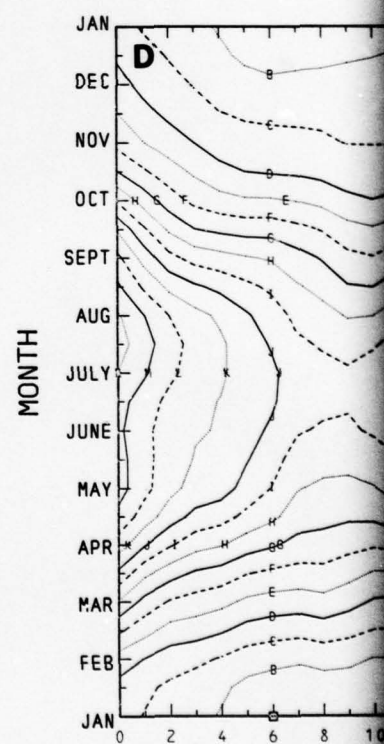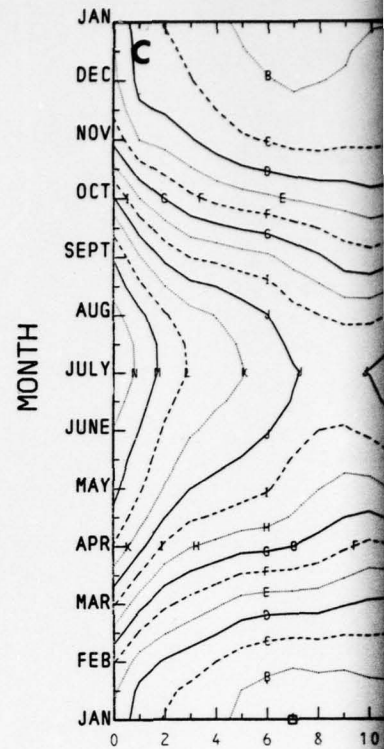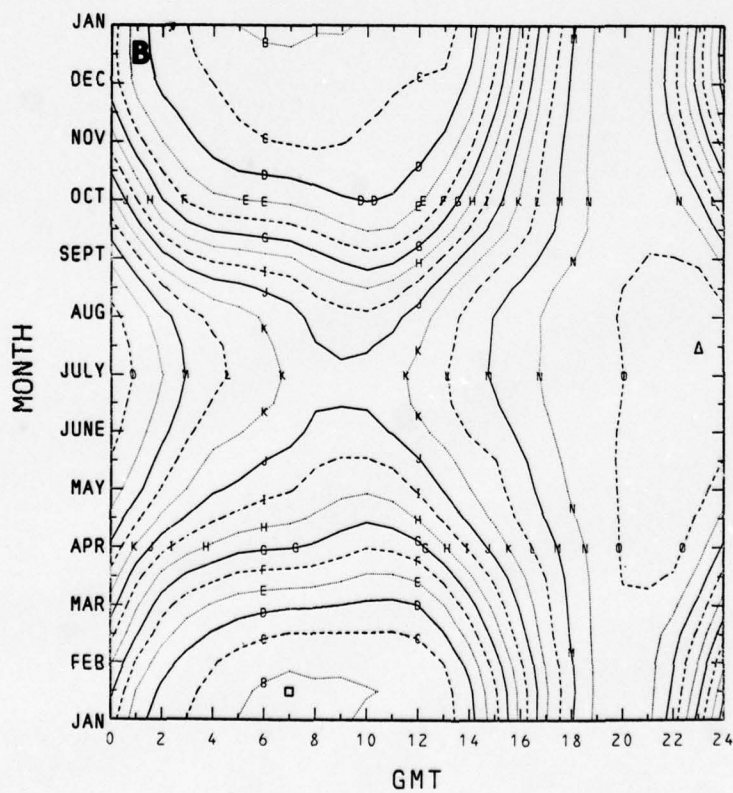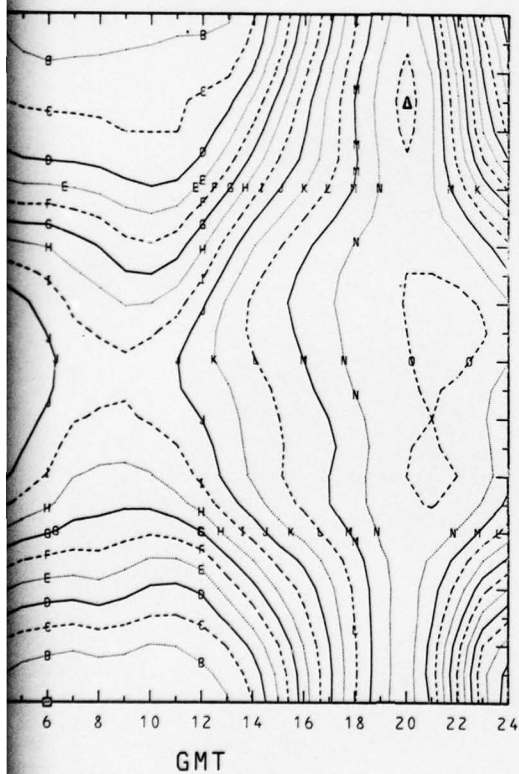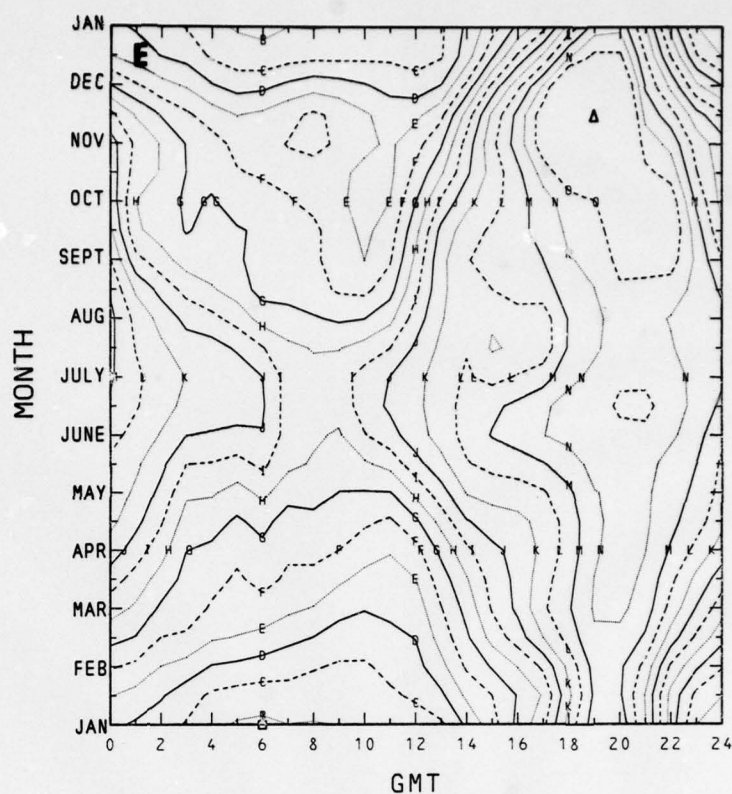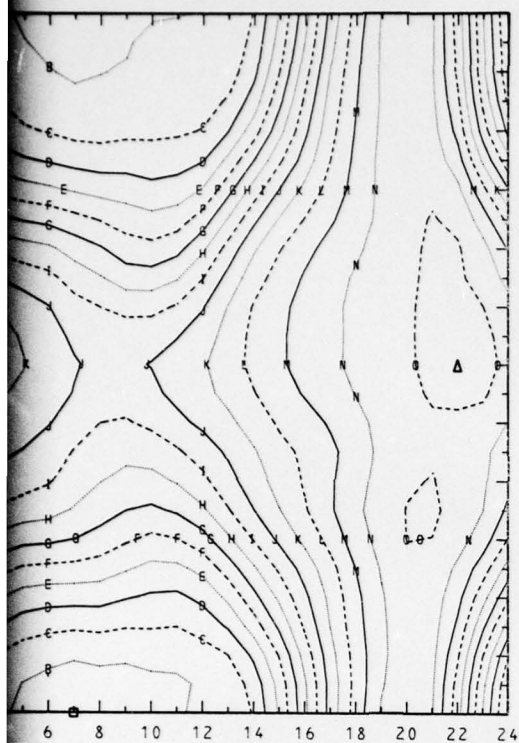
		□	△
A.	Maximum	0.358	1.086
B.	Upper Quartile	0.340	1.034
C.	Median	0.325	1.019
D.	Lower Quartile	0.311	1.025
E.	Minimum	0.339	1.207

Figure 3-7. Smoothed Values of foF2 Relative to the foF2
Values of 20:00 GMT at Ft. Churchill vs GMT and Month

3-13

Contour
Levels

A = -1.0
B = -0.8
C = -0.6
D = -0.4
E = -0.2

F = 0.0
G = 0.2
H = 0.4
I = 0.6
J = 0.8
K = 1.0

□ = -0.814   △ = 0.814
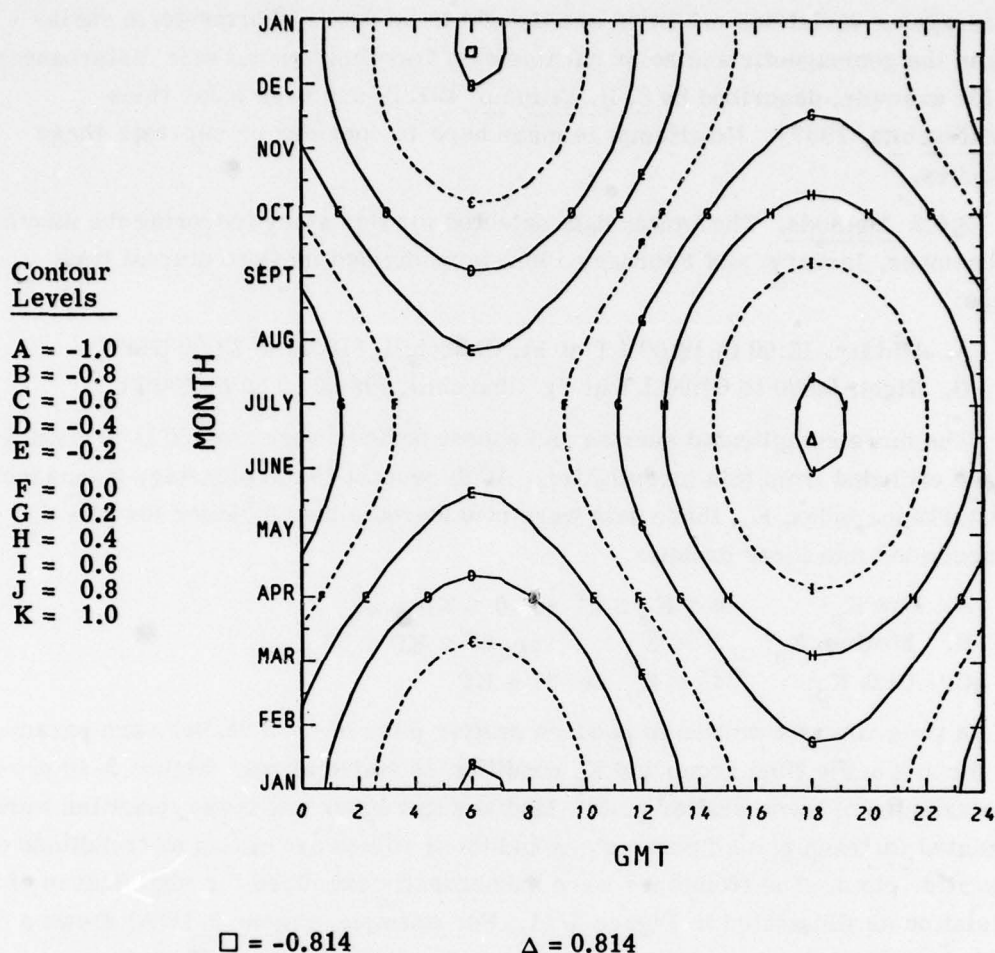
Figure 3-8. Contours of the COS (Solar Zenith Angle) vs Month
and GMT for Ft. Churchill

B. The Local Parameters [Serson, 1968]

Geomagnetic Field Components in gammas, magnetometer measurements
at Ft. Churchill

    1. DELHN (δH_N) — Hourly ranges in the north direction.

    2. DELHE (δH_E) — Hourly ranges in the east direction.

    3. AVHN ($\overline{H}_N$) — Hourly averages in the north direction.

    4. AVHE ($\overline{H}_E$) — Hourly averages in the east direction.

    5. AVHV ($\overline{H}_V$) — Hourly averages in the vertical direction.

An initial examination of the data showed that the relations between foF2 and
the geophysical parameters were not well-determined smooth functions. The re-
lations are rather noisy and therefore can only be described in a statistical sense.

3-15

The irregular variations exhibited are thought to be due to shorter-term variations in the geomagnetic and solar parameters, traveling ionospheric disturbances (as, for example, described by S. H. Francis [1973]), and even lunar tides [S. Matsushita, 1967]. No attempt is made here to consider or separate these influences.

3.6.2 Methods. The winter data selected for this study (covering the months of December, January, and February 1968) were divided into two diurnal time groups:

A. Midday, 12:00 to 16:00 LT at Ft. Churchill, (18:00 to 22:00 GMT)
B. Night, 00:00 to 04:00 LT at Ft. Churchill, (06:00 to 10:00 GMT).

The more complicated sunrise and sunset periods were treated in Section 2 and are excluded from this investigation. With respect to the planetary geomagnetic disturbance index, K_p, these data were considered either together for "all K_p" or subdivided into three groups:

A. Low K_p: $0 \leq K_p \leq 2^+$ or $0 \leq KP \leq 23$
B. Medium K_p: $3^- \leq K_p \leq 3^+$ or $27 \leq KP \leq 33$
C. High K_p: $4^- \leq K_p$ or $37 \leq KP$

A program was written to produce scatter plots of foF2 versus each parameter for a specific time group and K_p condition as stated above. Figure 3-10 provides samples of these scatter plots. Medians and upper and lower quartiles were calculated for each pair of parameters and these values are shown as trendlines on the scatter plots. The trendlines were subsequently examined for significance of correlation as illustrated in Figure 3-11. For example, Figure 3-10(A) shows a significant (negative) correlation of foF2 and K_p, while Figure 3-10(B) shows a significant (positive) correlation of foF2 with DSSN. Qualitative results on the correlation for all parameters and conditions were so obtained and the results are summarized in Table 3-1. In addition, quantitative descriptions of the correlations of foF2 with the other geophysical parameters were obtained for midday, "all K_p" conditions; these results are summarized in Table 3-2. Here, the sensitivity of the foF2 determination from measurements of each parameter (PAR) was described by the range of the parameter variation (ΔPAR) as measured between the trendline extremes and by the concurrent variation (ΔfoF2) of foF2 as measured on the median trendline. The absolute uncertainty in the foF2 determination was calculated from

$$UfoF2 = \frac{1}{2n} \sum_{m=1}^{n} \left(UQ_m - LQ_m \right) \tag{3-7}$$

where n = number of PAR groups, and the UQ and LQ are upper and lower quartile

Contour
Levels

A = 0.2
B = 0.3
C = 0.4
D = 0.5
E = 0.6

F = 0.7
G = 0.8
H = 0.9
I = 1.0
J = 1.1

K = 1.2
L = 1.3
M = 1.4
N = 1.5
O = 1.6
P = 1.7

Q = 1.8
R = 2.0
S = 2.2
T = 2.4
U = 2.6
V = 2.8

MONTH

GMT
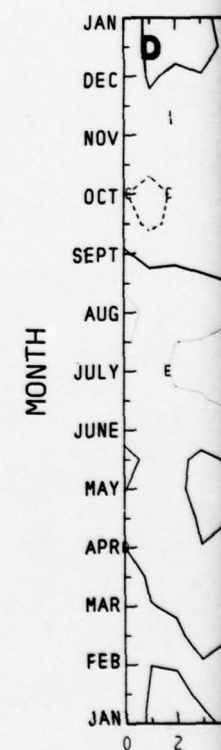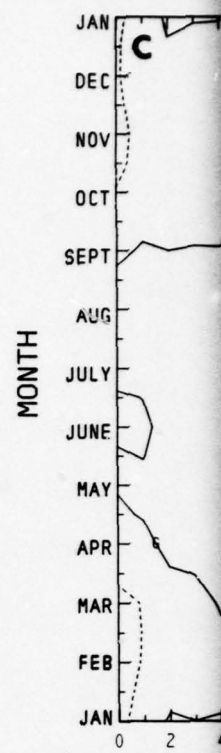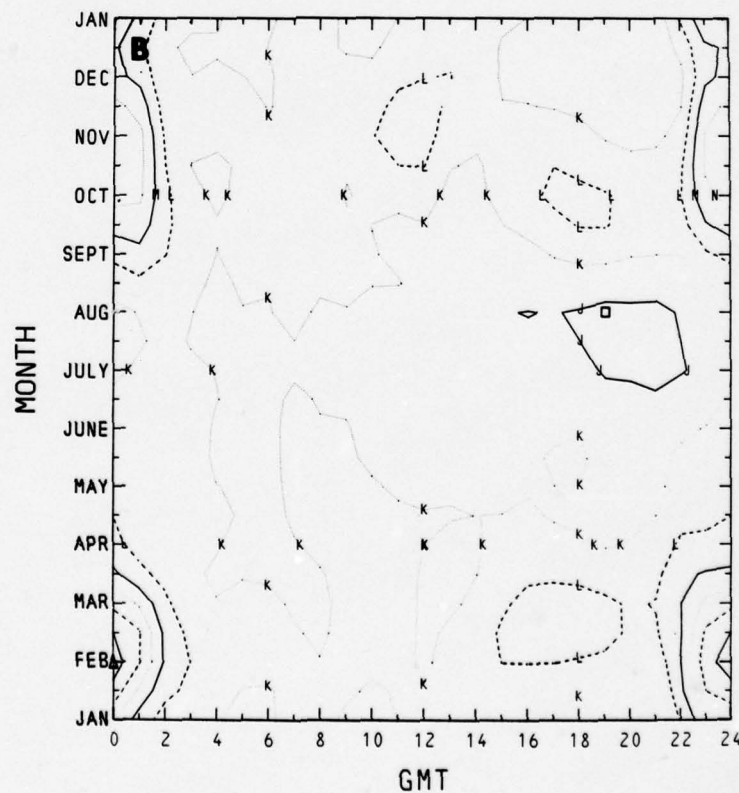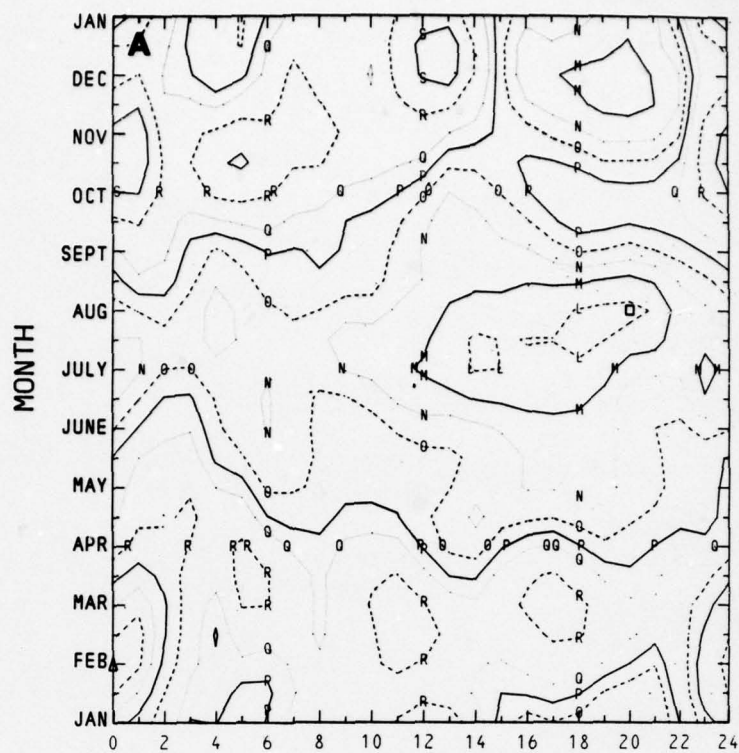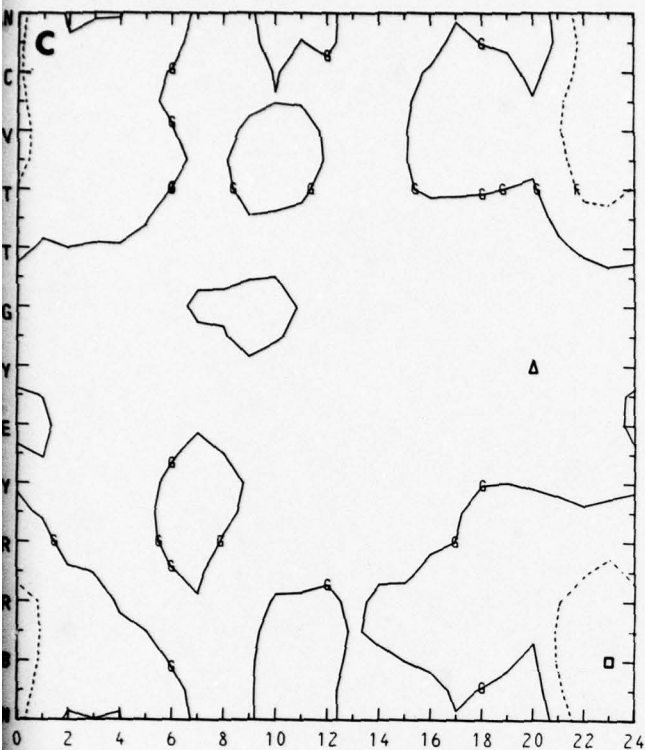
		□	Δ
A.	Maximum/Median	1.273	2.715
B.	Upper Quartile/Median	1.081	1.753
C.	Lower Quartile/Median	0.525	0.895
D.	Minimum/Median	0.247	0.694

Figure 3-9. Smoothed Ratios of Electron Densities at F2 Layer Peak for Ft. Churchill vs GMT and Month

GMT
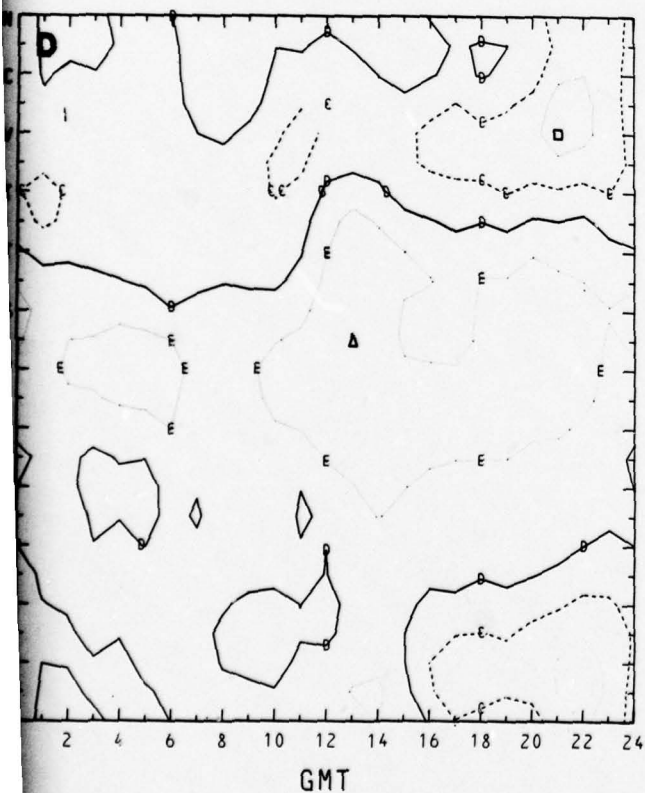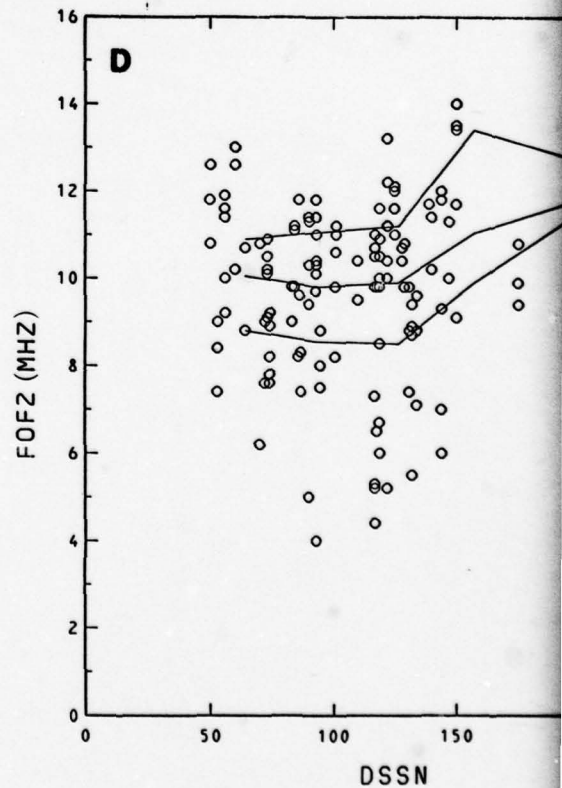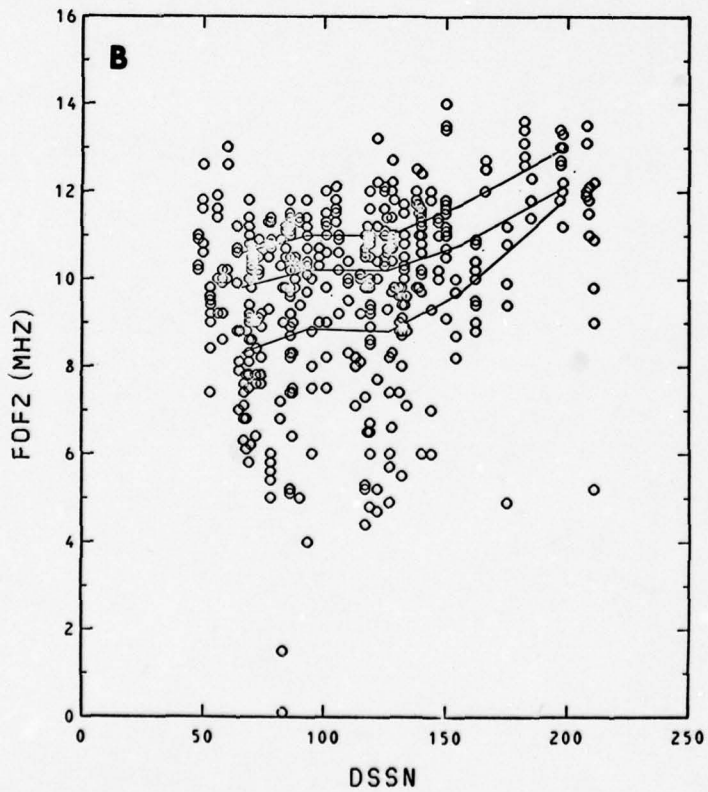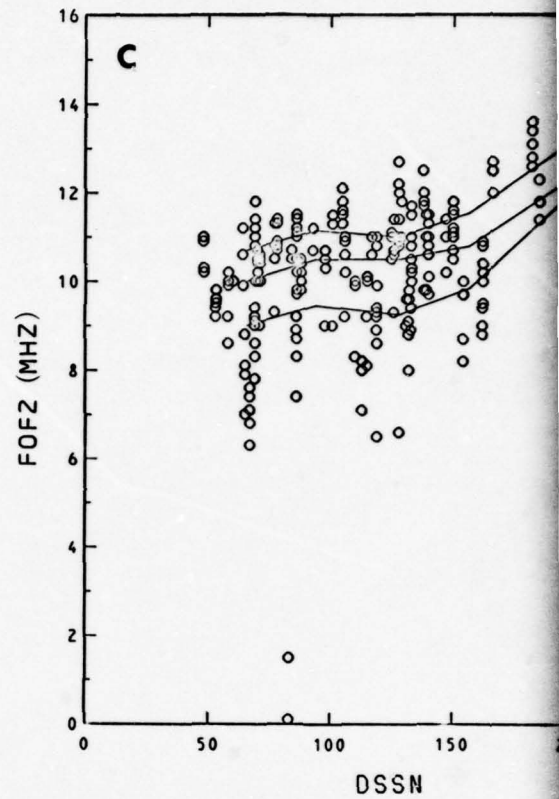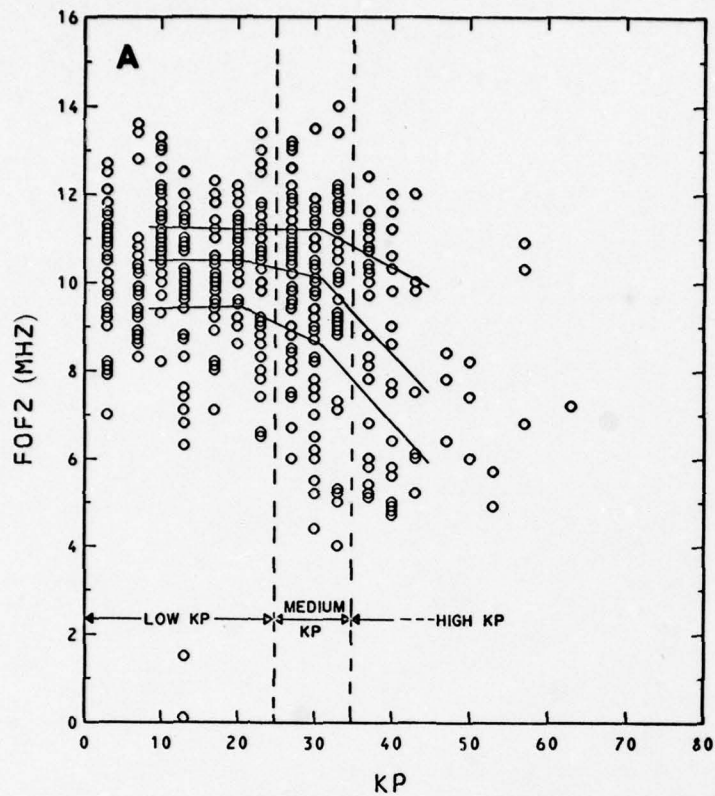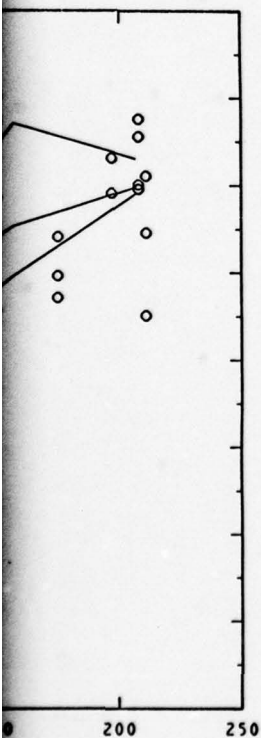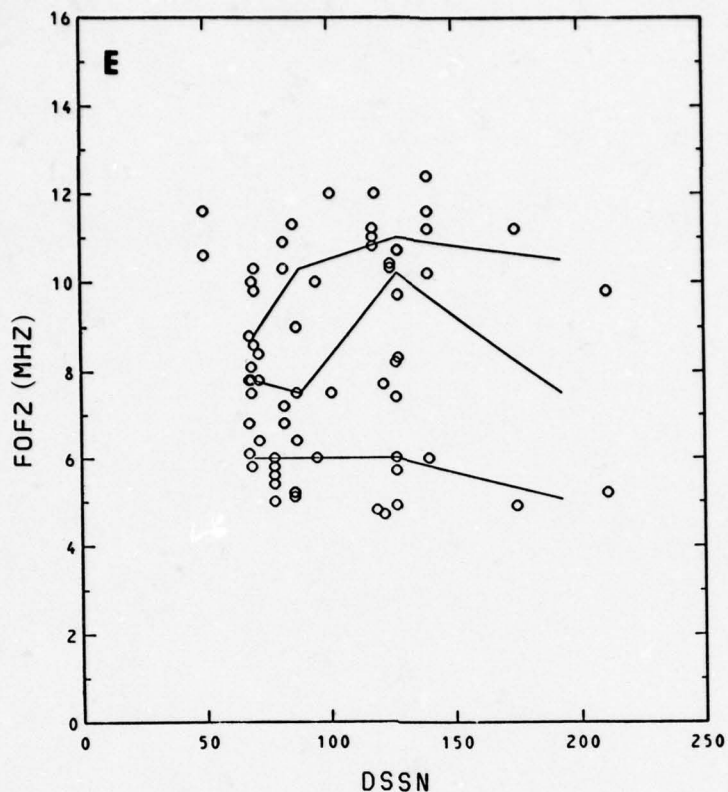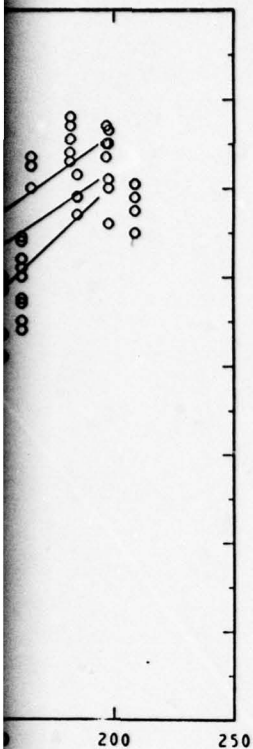
A. foF2 vs K_p, All K_p
B. foF2 vs DSSN, All K_p
C. foF2 vs DSSN, $0 \leq K_p \leq 23$
D. foF2 vs DSSN, $27 \leq K_p \leq 33$
E. foF2 vs DSSN, $K_p \geq 37$.

Circles are data points. Lines
give calculated lower quartile,
median, and upper quartile levels.

Figure 3-10. Ordinary Critical Frequency at F2 Layer
Maximum (foF2 in MHz) vs Planetary Geomagnetic
Disturbance Index (K_p) and Daily
Sunspot Number (DSSN)

3-19
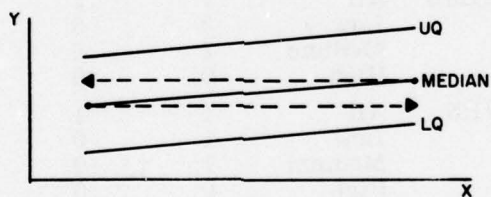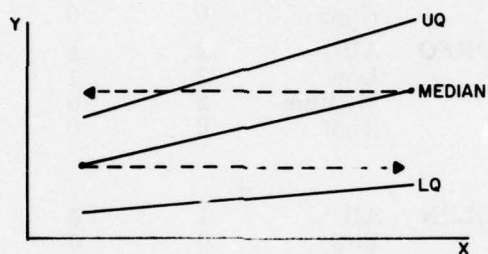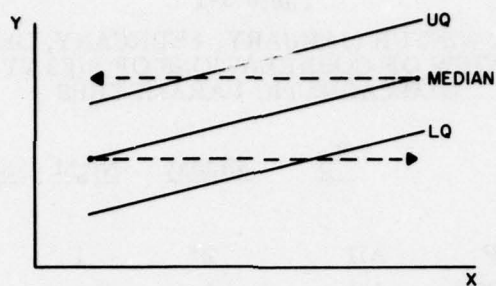
A. Correlation Significant

B. Correlation Marginal

C. Correlation Not Significant

Figure 3-11. Method Used to Determine
Significance of Correlation

Table 3-1

FT. CHURCHILL WINTER (JANUARY, FEBRUARY, DECEMBER 1968) OVERVIEW OF CORRELATIONS OF foF2 VERSUS GEOMAGNETIC PARAMETERS

Parameter		K_p	Midday	Night	Sum	Parameter Total
Global						
Magnetic	KP	All	2*	1	3	3
Solar	DSSN	All	2	1	3	
		Low	2	2	4	
		Medium	2	1	3	10
		High	0	0	0	
Solar	DORFO	All	2	1	3	
		Low	2	1	3	
		Medium	2	0	2	8
		High	0	0	0	
Local Magnetic						
	DELHN	All	1	0	1	
		Low	0	0	0	
		Medium	0	1	1	4
		High	1	1	2	
	DELHE	All	1	1	2	
		Low	2	0	2	
		Medium	2	0	2	6
		High	0	0	0	
	AVHN	All	1	1	2	
		Low	1	0	1	
		Medium	1	0	1	4
		High	0	0	0	
	AVHE	All	2	0	2	
		Low	0	1	1	
		Medium	0	1	1	4
		High	0	0	0	
	AVHV	All	2	0	2	
		Low	1	0	1	
		Medium	0	1	1	7
		High	2	1	3	
Time of Day Total			31	15	46	

*0 = No significance, 1 = Marginal, 2 = Significant correlation.

3-22

Table 3-2

DETERMINATION OF foF2 AT FT. CHURCHILL - WINTER 1968, DAYTIME, ALL K_p

Geophysical Parameter (PAR)		Sensitivity of foF2 Determination for PAR Ranges with 15 Data Points		Uncertainty (50% Confidence Limits) in foF2 [UfoF2 (MHz)]	Quality of Measurement $Q = \frac{\Delta foF2}{UfoF2}$	Rank
		ΔPAR	$\Delta foF2$ (MHz)			
Global						
Magnetic	KP	36.2 (1)	3.00	±1.275	2.35	1A
Solar	DSSN	132.7 (1)	2.30	±0.985	2.34	1B
	DORFO	$102.6 \times 10^{-22} \frac{W}{M^2 Hz}$	2.10	±0.895	2.35	1C
Local						
Magnetic	DELHN	110.02 (Gammas)	2.00	±1.255	1.59	4
	DELHE	110.4 (Gammas)	2.63	±1.30	2.02	2
	AVHN	119.0 (Gammas)	1.99	±1.31	1.52	5
	AVHE	58.2 (Gammas)	1.42	±1.195	1.19	6
	AVHV	121.1 (Gammas)	2.20	±1.33	1.65	3

3-23

values of foF2 for each group. The relative quality of this foF2 determination was then calculated as

$$Q = \frac{\Delta foF2}{\left| UfoF2 \right|} . \tag{3-8}$$

3.6.3 <u>Results</u>. Correlation results were revealed by examining the trend-lines of each scatter plot and are described by numerical values of 1, 2, or 3 in Table 3-1. It was found that the correlations of foF2 with the eight geophysical parameters were much better during the midday period than at night. During mid-day and covering "all K_p" conditions foF2 was significantly correlated with K_p with the two daily solar indices and with the hourly averages of the east and vertical geomagnetic field components at Ft. Churchill.

The quantitative assessment of these correlations, considering both the sensitivity and uncertainty of foF2 determination for the midday, "all K_p" condition revealed that the global parameters (K_p and the two daily solar indices) provided a fair measurement of foF2, while the hourly range of the east geomagnetic field component was the only local parameter of similar quality. None of the separately studied geophysical parameters determined foF2 uniquely.

Subdividing the data into three K_p groups according to low, medium, and high K_p also revealed a complicated behavior of the foF2 correlations with the other seven parameters. For the more frequent occurrences of low and medium K_p and under midday conditions, foF2 was significantly correlated with the two daily solar indices and the hourly ranges in the east geomagnetic field. All correlations deteriorated under high K_p conditions.

3.7 Correlation of foF2 with Lagged Planetary Geomagnetic Disturbance Index, K_p

The strong (negative) correlation of foF2 with the planetary geomagnetic index, K_p, is known and was shown in the previous study (Section 3.6). It was also suspected that foF2 might be better predicted from K_p at times other than that of the observed foF2, and this prompted a correlations study of this critical frequency with a lagged K_p.

Scatter plots were made of foF2 for the time 19:30 GMT vs K_p at times before and after 19:30 for the winter months of January, February, and December 1968. Similarly, K_p centered on this time was plotted versus the lagged K_p's (KPB1, KPB2, etc., which are described in Table 3-3). The upper quartile, median, and lower quartile lines on these scatter plots were examined for significance of correlation according to the method shown in Figure 3-11. This preliminary investigation revealed a delayed influence of K_p into foF2, and that foF2 of midday

3-24

might be better predicted on the basis of the previous local midnight's K_p; foF2 at 19:30 GMT was best correlated with KP3 at 07.30 GMT. Also, finding a better

Table 3-3

TIME RELATIONS FOR CORRELATIONS OF SMOOTHED ORDINARY CRITICAL FREQUENCY AT F2 PEAK (foF2) WITH GEOMAGNETIC DISTURBANCE INDEX (K_p) LAGGED BY ΔT — EXAMPLES FOR TIME OF SfoF2 MEASUREMENT AT TSfoF2 = 19:30 GMT.

Time of K_p Data (TKP)

Day Relative To Day of foF2 Data	Time of Day		ΔT (hrs) = TKP - TSfoF2	Name of K_p Value	Sample Figure
	GMT	LCGT			
Before	01:30	18:30	-42	KPB1	3-13A
	04:30	21:30	-39	KPB2	
	07:30	00:30	-36	KPB3	
	10:30	03:30	-33	KPB4	
	13:30	06:30	-30	KPB5	
	16:30	09:30	-27	KPB6	
	19:30	12:30	-24	KPB7	
	22:30	15:30	-21	KPB8	
Same	01:30	18:30	-18	KP1	
	04:30	21:30	-15	KP2	
	07:30	00:30	-12	KP3	3-13B
	10:30	03:30	-9	KP4	
	13:30	06:30	-6	KP5	
	16:30	09:30	-3	KP6	
	19:30	12:30	0	KP7	3-13C
	22:30	15:30	+3	KP8	
After	01:30	18:30	+6	KPA1	3-13D
	04:30	21:30	+9	KPA2	
	07:30	00:30	+12	KPA3	
	10:30	03:30	+15	KPA4	
	13:30	06:30	+18	KPA5	
	16:30	09:30	+21	KPA6	
	19:30	12:30	+24	KPA7	
	22:30	15:30	+27	KPA8	

numerical way to describe quality of correlation seemed necessary as a means of clarifying cases found using the manual method (see Figure 3-11) that were just barely or questionably correlated. Figure 3-12 shows a method of calculating a correlation quality ratio (CQR) and sensitivity (SENSY) from the parameters A and B, where

$$CQR = \frac{BDIFF}{QAV} \tag{3-9}$$

and the uncertainty

$$QAV = \frac{1}{2n} \sum_{m=1}^{n} [UQ(m) - LQ(m)] \quad . \tag{3-10}$$

The sensitivity

$$SENSY = \frac{BDIFF}{ADIFF} \quad . \tag{3-11}$$

The CQR is thus related to the manual determination previously used and is a general statement of the ratio Q described in Section 3.6.2. The significance of correlation was decided as follows:

    A. $|CQR| < 1.0$ (no correlation)

    B. $|CQR| \cong 1.0$ (marginal correlation)

    C. $|CQR| > 1.0$ (significant correlation).

Since foF2 is negatively correlated with K_p, the absolute values of CQR here are also negative. The foF2 data were again scatter plotted versus a range of K_p's and the correlations were described by the CQR. Hourly values of SfoF2(t) were obtained by weighted smoothing of hourly values of foF2 like

$$SfoF2(t) = \frac{1}{6} \cdot [foF2(t - 1.5) + 2 \cdot foF2(t - 0.5) + 2 \cdot foF2(t + 0.5) + foF2(t + 1.5)] \tag{3-12}$$

to resemble more closely the three-hourly K_p index. Figure 3-13 is a sample of these plots of three-hour-averaged foF2 data versus KPB1, KP3, KP7, and KPA1 for the hours 18:00 to 20:00 GMT. The K_p times are described in Table 3-3 and in the legend of Figure 3-13. Noteworthy, again, is the stronger correlation of the noontime SfoF2 with the local midnight KP3 than with KP7. KP7, which is for the same three-hour time period as SfoF2, was plotted versus the range of K_p's, KPB, ..., KPA8, as shown, e.g., in Figure 3-14.

Considering only cases where $|CQR| > 2$, (a) SfoF2 was well correlated with K_p's within the same day and for 15 hours before, i.e., KP2 through KP7, and (b) KP7 was well correlated with a range of K_p for 9 hours before and 12 hours

3-26
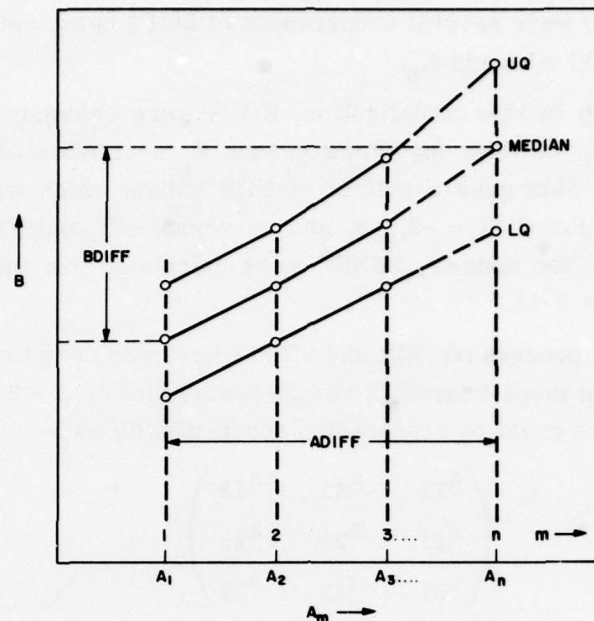
Figure 3-12. Method for Calculating a Correlation
Quality Ratio, Sensitivity, and Uncertainty
from the Parameters A and B

after, or KP4 through KPA3. The findings from (a) above are due partially to the good correlation of KP7 with lagged K_p's except that in the case of KP7 vs KP3 there was no correlation whereas SfoF2 and KP3 were highly correlated. These relations are made clearer in Figure 3-15 developed by J. H. W. Unger [1973]. This shows the distribution of calculated CQRs for one hour in the winter, 19:30 GMT. Note in Figure 3-15(A) the peak CQR of -5.0 for SfoF2 versus KP3 ($\Delta T = -12$), and in Figure 3-15(B) a CQR indicating a marginal correlation of KP7 with KP3 ($\Delta T = -12$).

Figure 3-16 by J. H. W. Unger [1973] shows the complexity in predicting foF2 on the basis of K_p. For each season of 1968, the peak CQR's for the cross correlation of SfoF2 with K_p's lagged by ΔT from +27 to -42 in three-hour steps were selected and plotted here with respect to the time difference for the peaks versus the local corrected geomagnetic time (LCGT) for SfoF2. LCGT differs from GMT by seven hours and from LT at Ft. Churchill by one hour. The most surprising event here is that most occurrences of peak correlation do not happen for values of SfoF2 and K_p at $\Delta T = 0$. For these data, this same time correlation seems to occur mainly in winter and fall during the sunset period and in the spring for a few hours after sunrise. Otherwise, the scatter in peak correlations is quite complicated. In the winter from early morning until

3-27

early afternoon there were several occurrences of SfoF2 being well correlated with the previous LCG midnight K_p.

As a final step in this investigation, CQRs were calculated for each season or approximately 90 days for SfoF2 versus K_p's at $\Delta T = +27$ to $\Delta T = -18$ in one-hour steps. This gave a matrix of CQR values which were smoothed and contour plotted for CQR = -2, -3, and -4 versus ΔT and TSfoF2 as seen in Figure 3-17. In like manner, SENSY were calculated and these contours are shown in Figure 3-18.

The smoothing process on CQR and SENSY here was done to compensate for the time difference of three-hour K_p's versus hourly SfoF2. 3×3 sections of CQR or SENSY, which could be represented schematically as

$$
\begin{pmatrix}
a_{11} & a_{12} & a_{13} \\
a_{21} & a_{22} & a_{23} \\
a_{31} & a_{32} & a_{33}
\end{pmatrix}
$$

where a_{ij} are these values for K_p time in j and SfoF2 time in i, were averaged by weighting a_{22} by the sum of the weights of the neighboring points. The weighting could be described as

$$
\begin{pmatrix}
1/3 & 1/3 & 1/3 \\
1 & 4 & 1 \\
1/3 & 1/3 & 1/3
\end{pmatrix},
$$

and thus each centerpoint or smoothed data point

$$
a_{22} = \frac{1}{24} \cdot \left(a_{11} + a_{12} + a_{13} + 3a_{21} + 12a_{22} + 3a_{23} + a_{31} + a_{32} + a_{33} \right) \quad (3\text{-}13)
$$

From Figure 3-17, contours of CQR ≥ 2 (which represent areas of strong correlation) serve to emphasize the complexity in determining foF2 from lagged K_p's. We have in no way developed here a model for predicting such behavior, but have a suggested method of approaching the subject even for other locations.

For the Ft. Churchill data, these plots show some interesting trends. The winter maximum CQR of -5.2 [see Figure 3-17(A)] corresponds with the winter peak electron density which occurs near 14:00 LCGT or 21:00 GMT. In this same season the LCGT noontime SfoF2 are well correlated near the previous LCGT midnight K_p's; in the spring [Figure 3-17(B)] we also see a correlation between the SfoF2 data and K_p's near the previous LCGT midnight. The peak CQR's for the fall data [Figure 3-17(D)] occur for values of SfoF2 near 01:00 LCGT versus K_p's around the previous LCGT noon. The only instance of a peak CQR for $\Delta T = 0$ or for K_p and SfoF2 at the same time occurs in the summer as seen in Figure 3-17(C).

3-28
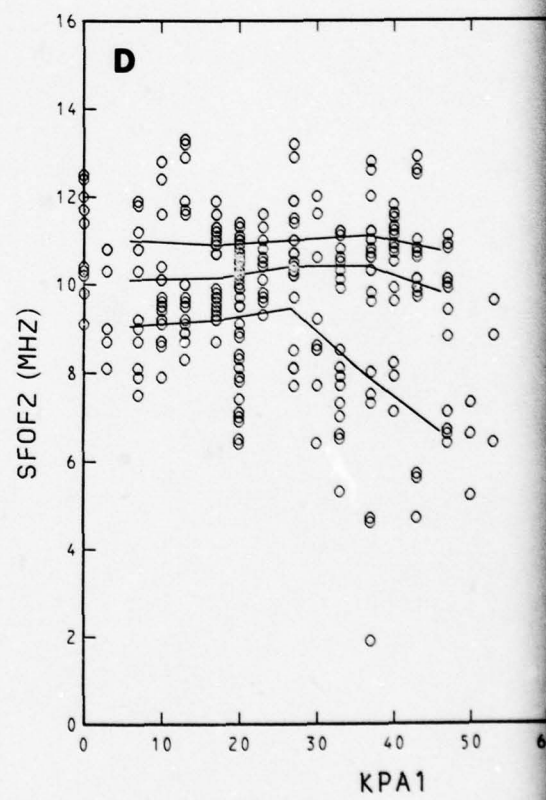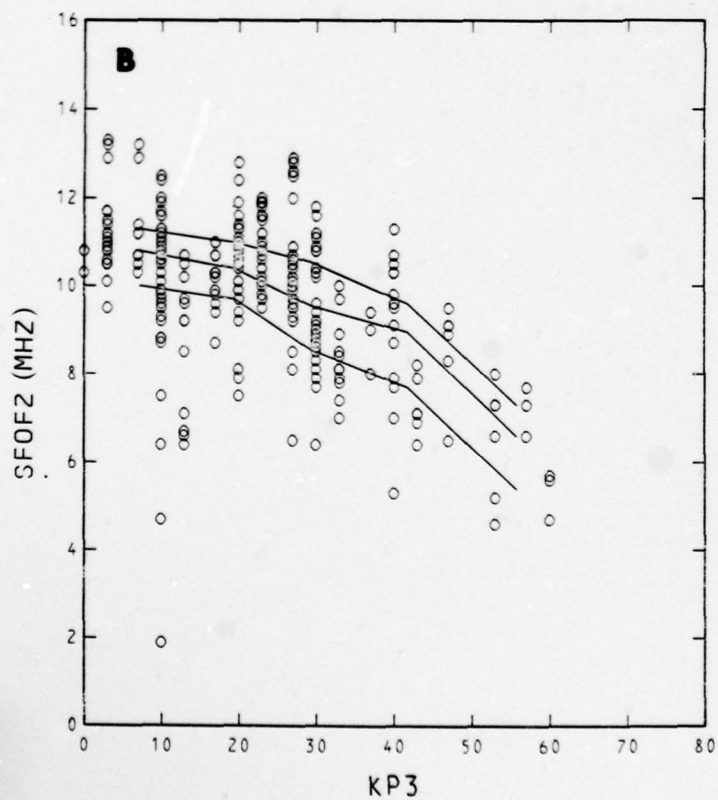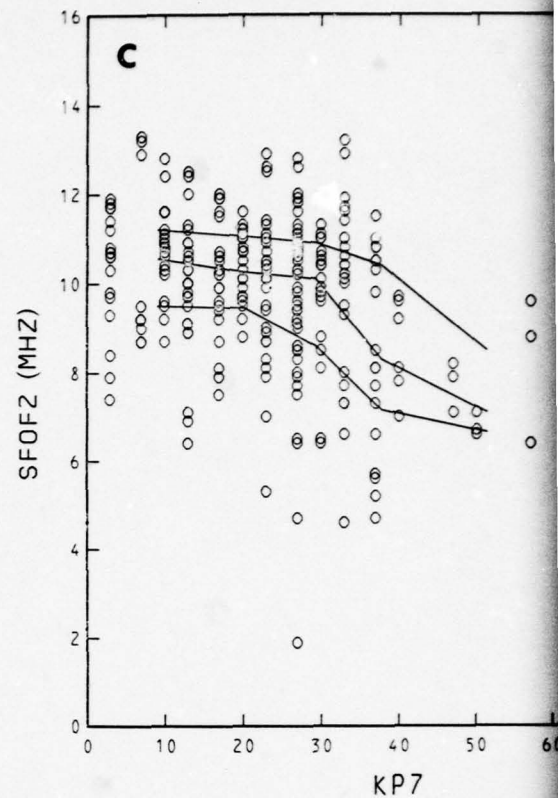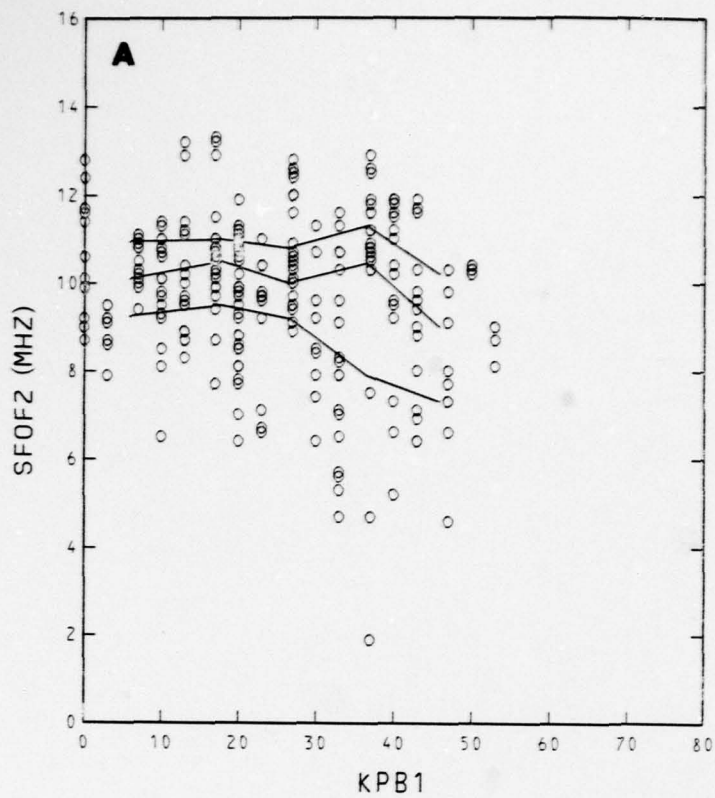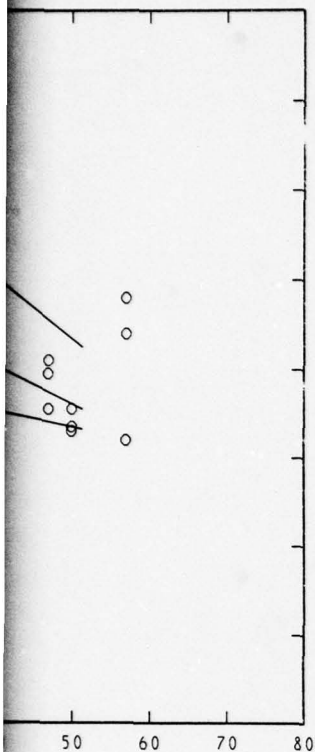
A. 01:30 GMT
   KPB1 Valid on Day Before foF2
   CQR = -0.991   SENSY = -0.027

B. 07:30 GMT
   KP3 Valid on Same Day as foF2
   CQR = -5.000   SENSY = -0.084

C. 19:30 GMT
   KP7 Valid on Same Day as foF2
   CQR = -3.224   SENSY = -0.082

D. 01:30 GMT
   KPA1 Valid on Day After foF2
   CQR = -0.240   SENSY = -0.007

Figure 3-13. Smoothed Ordinary Critical Frequency
at F2 Peak (SfoF2 in MHz) at Ft. Churchill in
January, February, and December 1968
at 18:00 to 20:00 GMT vs K_p*
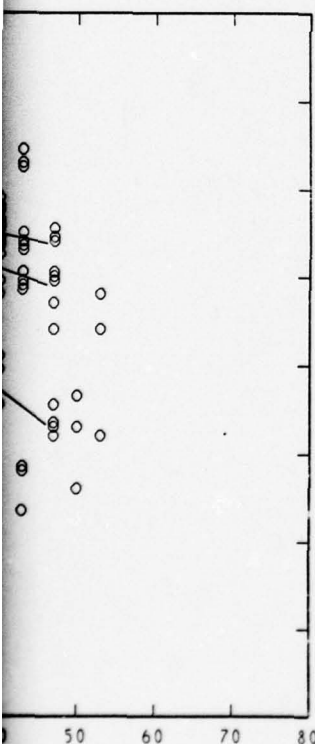
---

*Circles are data points. Lines give calculated Lower Quar-
tile, Median, and Upper Quartile levels.
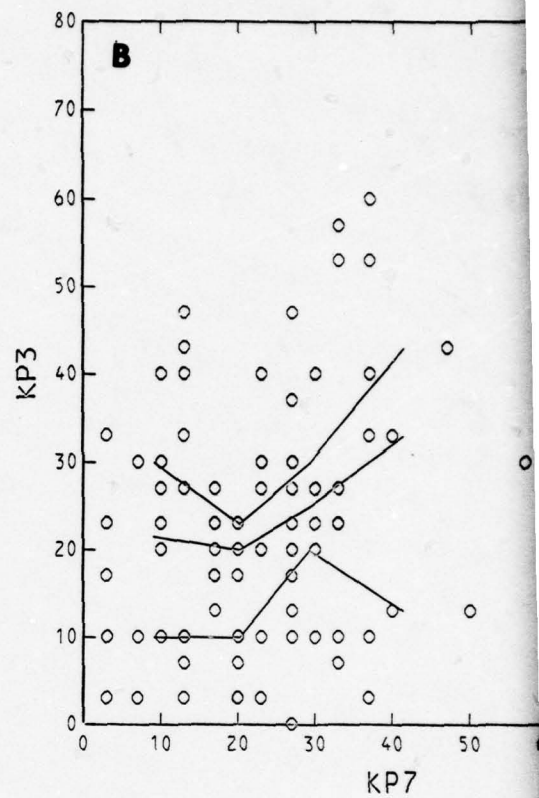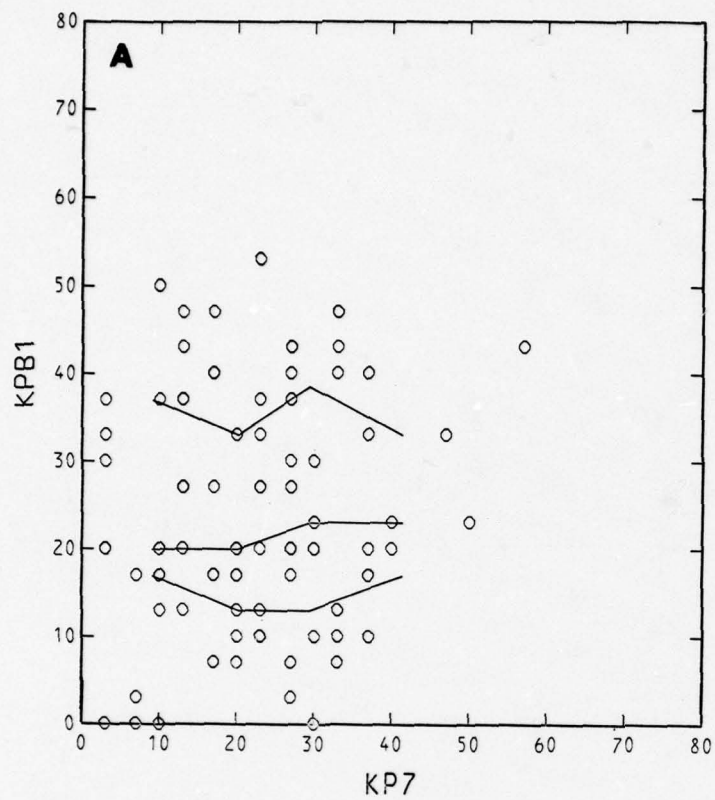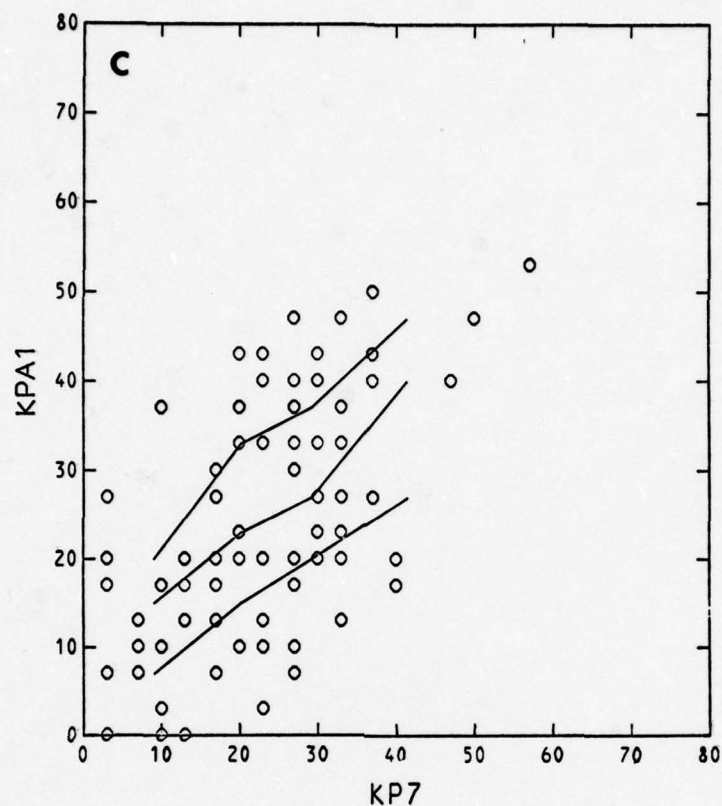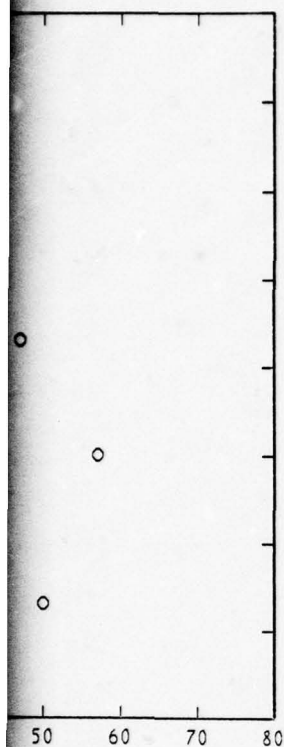
A. KPB1 at 01:30 GMT vs KP7 at 19:30 GMT
   KPB1 valid on the day before KP7
   CQR = 0.294   SENSY = 0.093

B. KP3 at 07:30 GMT vs KP7 at 19:30 GMT
   KP3 valid the same day as KP7
   CQR = 1.260   SENSY = 0.355

C. KPA1 at 01:30 GMT vs KP7 at 19:30 GMT
   KPA1 valid on the day after KP7
   CQR = 2.941   SENSY = 0.772

Figure 3-14. K_p for January, February, and December 1968
vs KP7 at 19:30 GMT*

---

*Circles are data points. Lines give calculated Lower Quartile, Median, and Upper Quartile levels.

3-31
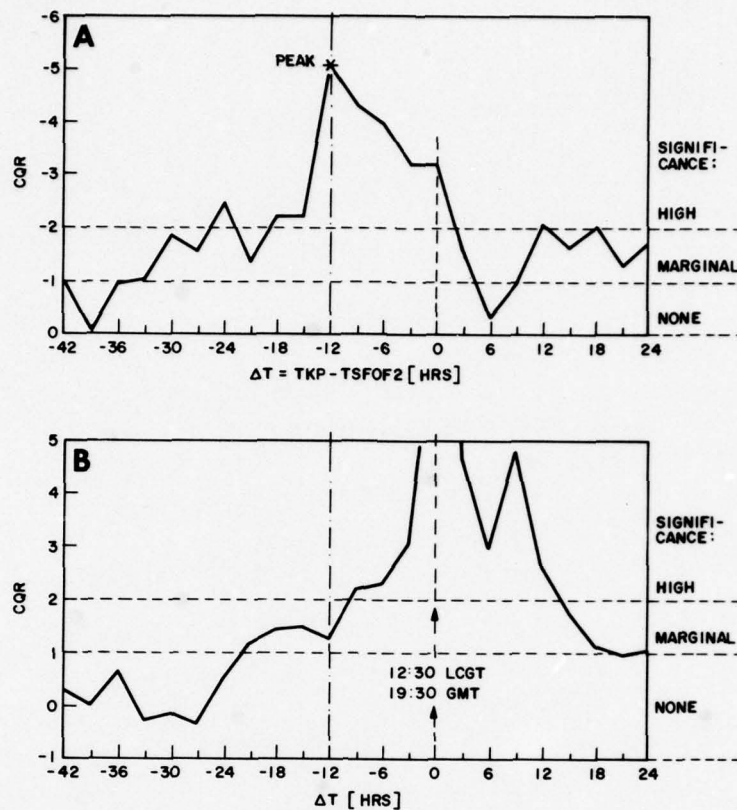
A. Cross-correlation of Three-Hour Smoothed foF2 With K_p

B. Auto-correlation of K_p

Figure 3-15. Distribution of Calculated CQRs for One Hour
in Winter 1968 at 19:30 GMT and vs ΔT,
the Time between SfoF2 and K_p

During the summer months and between the hours 03:00 LCGT and 12:00 LCGT we
see a continuing but diminishing influence of K_p for up to 24 hours after a peak
correlation at $\Delta T = 0$ and SfoF2 at 08:30 LCGT. Figure 3-18 shows similar plots,
but for the sensitivity (SENSY).
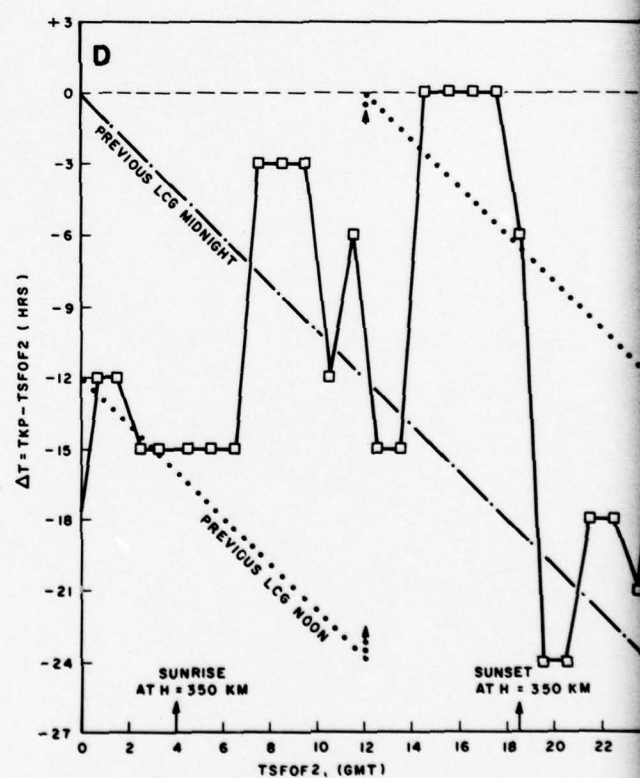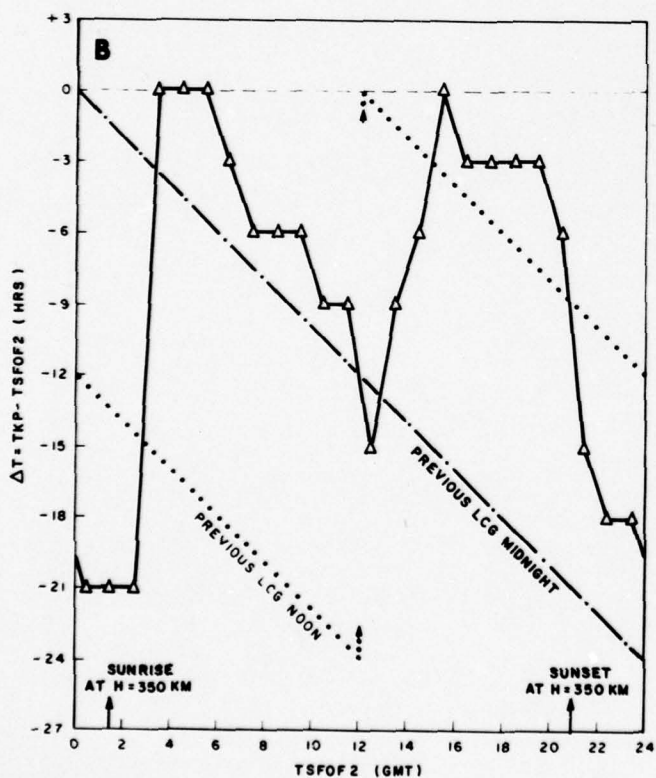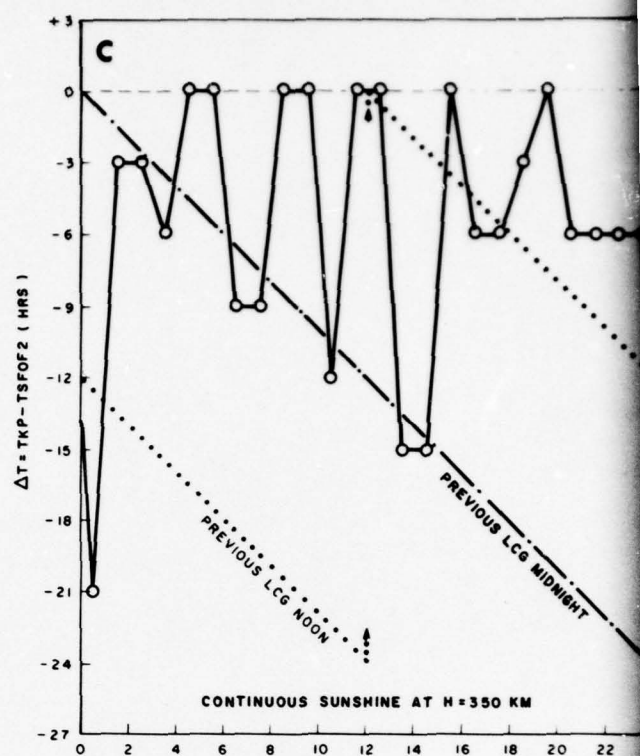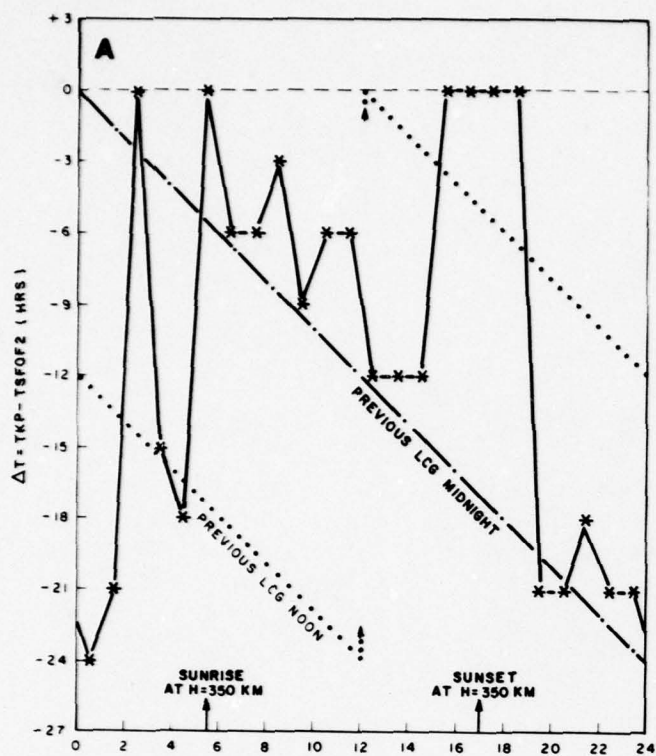
A. Winter (January, February, December)

B. Spring (March, April, May)

C. Summer (June, July, August)

D. Fall (September, October, November)

Figure 3-16. Peak CQR vs ΔT and TSfoF2 (LCGT) for Each Season of 1968

3-35
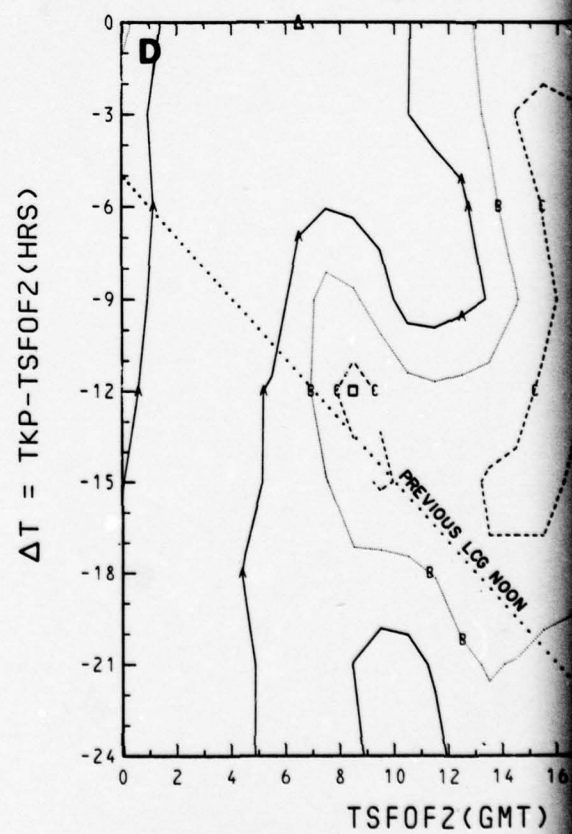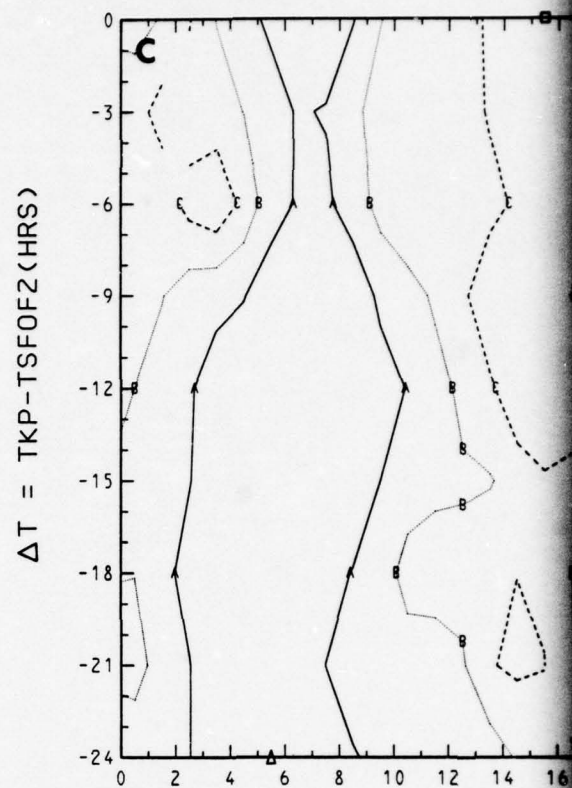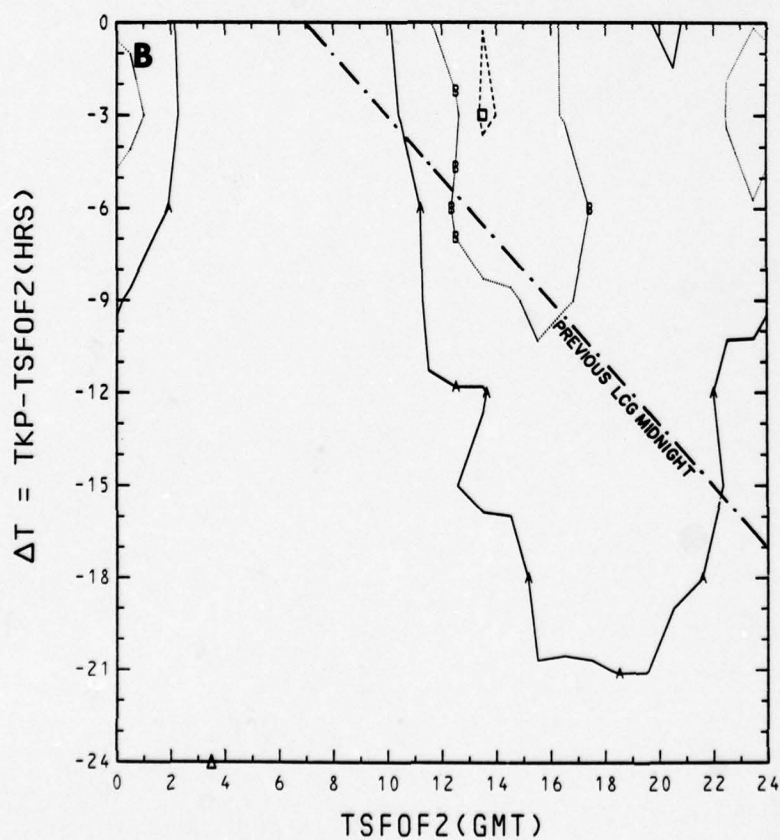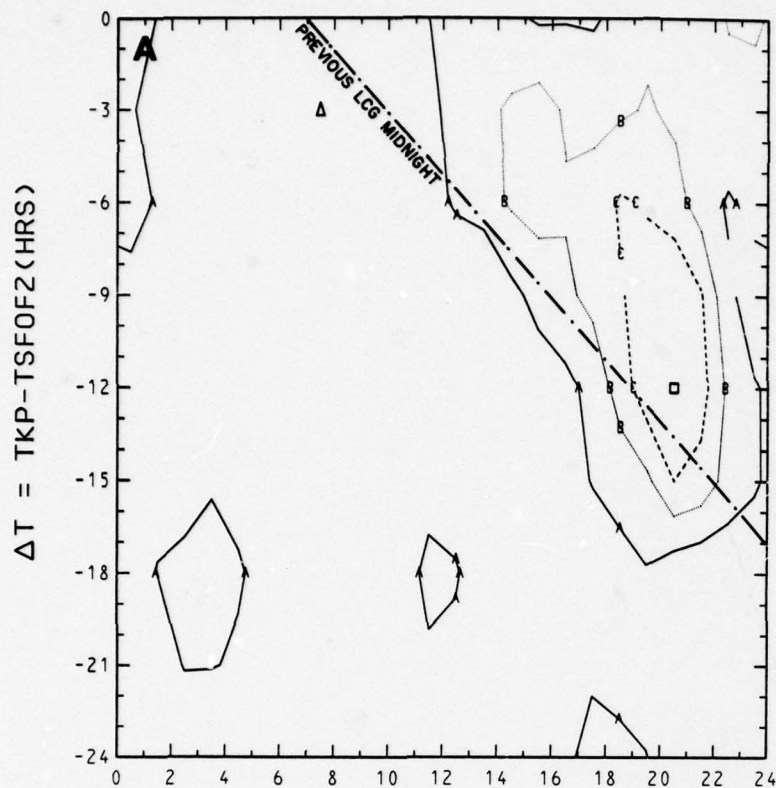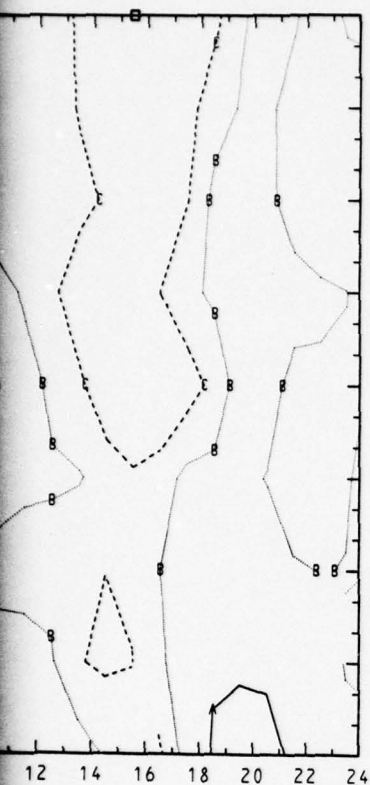
Contour
Levels

A = -2.000
B = -3.000
C = -4.000

A. Winter (January, February, December)
    □ = -5.180   Δ = 0.440

B. Spring (March, April, May)
    □ = -4.154   Δ = 0.341

C. Summer (June, July, August)
    □ = -6.188   Δ = -0.647

D. Fall (September, October, November)
    □ = -4.408   Δ = -0.298

Figure 3-17. Smoothed Contours of Correlation
Quality Ratio (CQR) Between Three-Hour-
Averaged foF2 data and K_p vs Time of
foF2 data (TSfoF2) and Time Difference
(ΔT) Between Time of K_p Data and
TsfoF2 for Ft. Churchill 1968
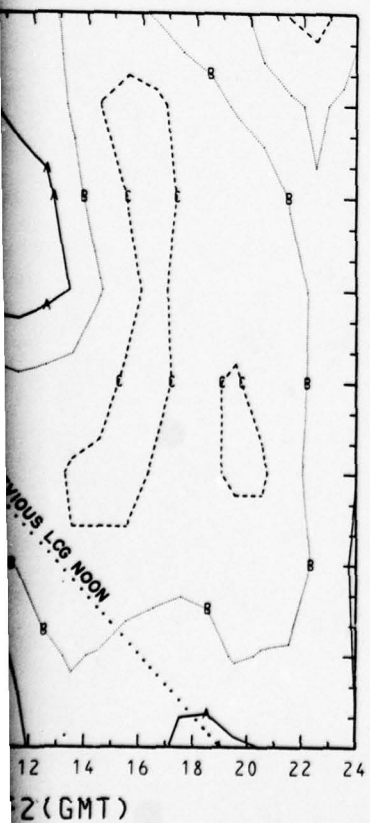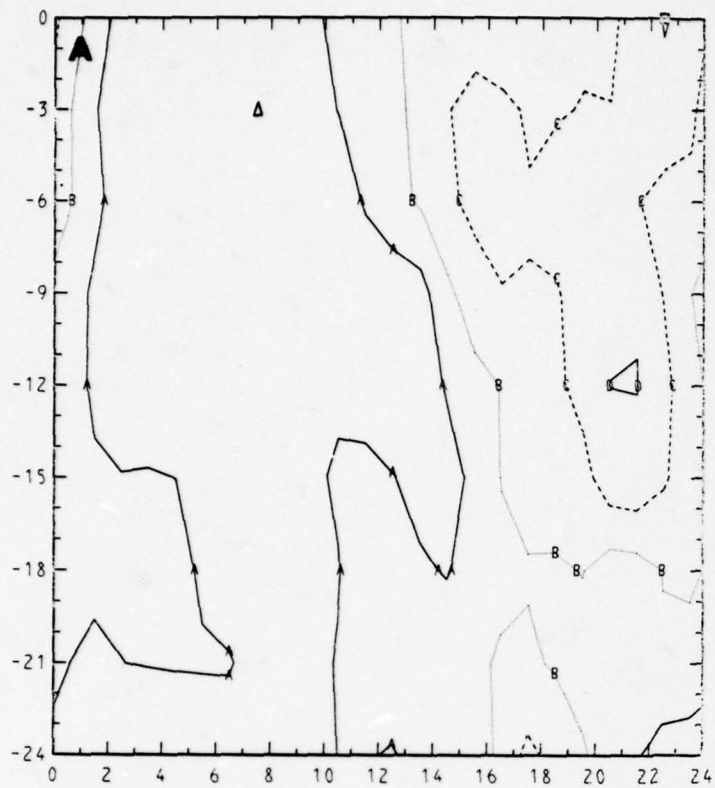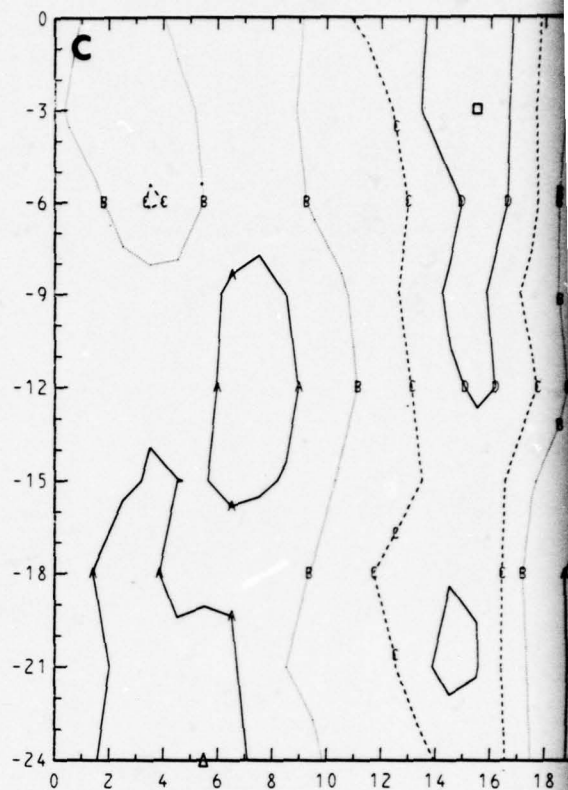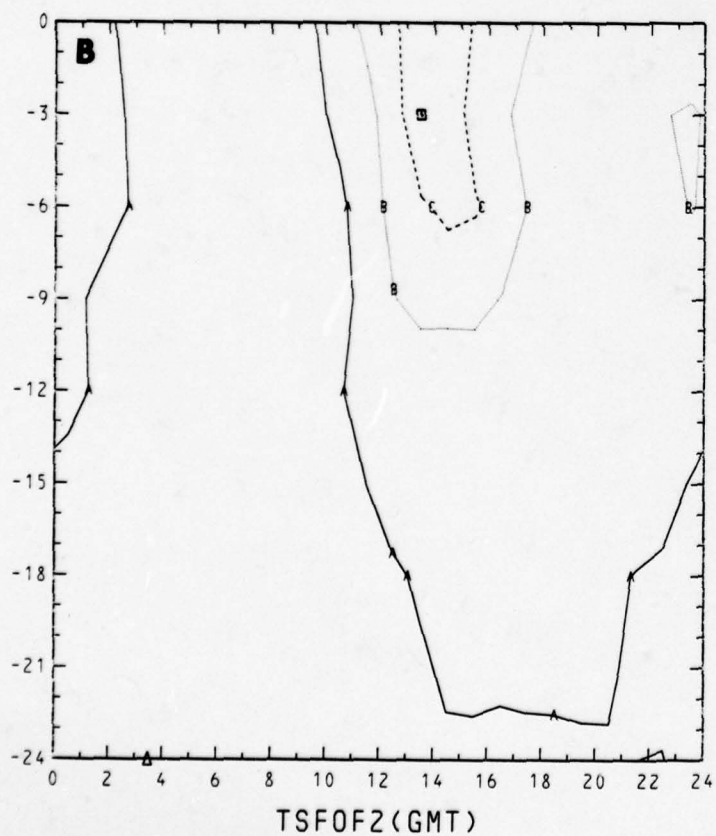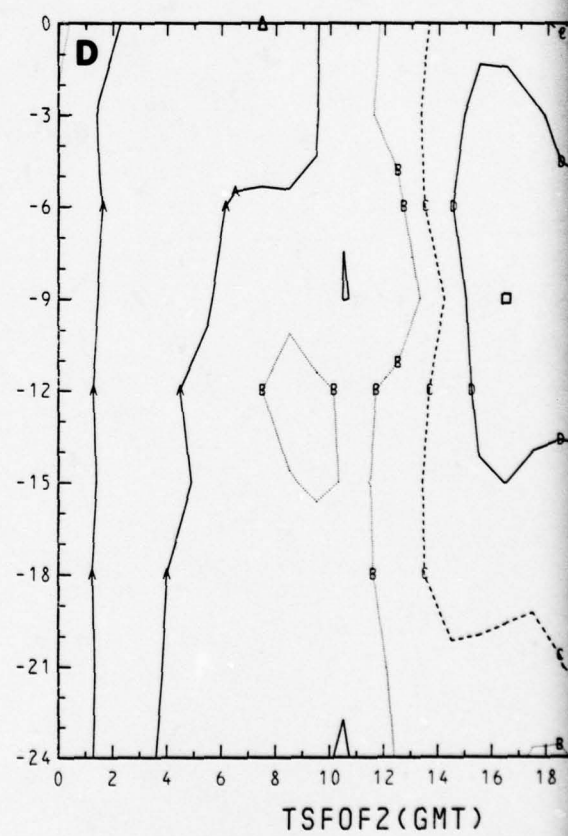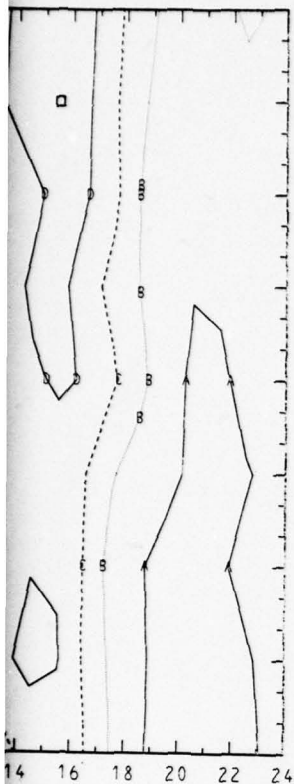
Contour
Levels

A = -0.250
B = -0.500
C = -1.000

A. Winter (January, February, December) 1968

☐ = -1.016   Δ = 0.063

B. Spring (March, April, May) 1968

☐ = -1.005   Δ = 0.042

C. Summer (June, July, August) 1968

☐ = -1.187   Δ = -0.124

D. Fall (September, October, November) 1968

☐ = -1.270   Δ = -0.052

Figure 3-18. Smoothed Contours of Sensitivity (SENSY)
of Three-Hour-Averaged foF2 Values to K_p Changes
vs Time of foF2, data (TSfoF2) and Time Difference
(ΔT) Between Time of K_p Data and TSfoF2 for
Ft. Churchill, 1968.

4. ACKNOWLEDGMENTS

5. REFERENCES

1. Badura, D. C., "Modified Chapman Fits to Millstone Hill Thomson Scatter Data," Bell Laboratories, Unpublished Work, 1971.

2. Bates, H. F., Belon, A. E., and Hunsucker, R. D., "Aurora and the Poleward Edge of the Main Ionospheric Trough," J. Geophys. Res., 78, 648 (1973).

3. Brice, N. M., "Bulk Motion of the Magnetosphere," J. Geophys. Res., 72, 5193 (1967).

4. Carpenter, D. L., "Whistler Evidence of a 'Knee' in the Magnetospheric Ionization Density Profile," J. Geophys. Res., 68, 1675 (1963).

5. Carpenter, D. L., "Whistler Studies of the Plasmapause in the Magnetosphere, 1, Temporal Variations in the Position of the Knee and Some Evidence on Plasma Motions Near the Knee," J. Geophys. Res., 71, 693 (1966).

6. Catalogue of Data on Solar-Terrestrial Physics, World Data Center A, Report UAG-11, June 1970.

7. Director, Telecommunications and Electronics Branch, Department of Transport, Ottawa, Ontario, Canadian Ionospheric Data (Churchill), Monthly, January through December 1968.

8. Dudziak, W. F., Kleinecke, D. D., and Kostigen, T. T., Graphic Displays of Geomagnetic Geometry, GE-TEMPO (Technical Military Planning Operation) Report RM 63 TMP-2, DASA 1372, 1 April 1963.

9. Essa Research Laboratories, "Solar-Geophysical Data," U. S. Department of Commerce, Environmental Data Service, February through November 1968, January and February 1969.

10. Evans, J. V., et al., "Disturbed Noncyclic Model of the High-Latitude Ionosphere," minutes of the BTL/LL Refraction Correction Working Group for 31 May 1972 (unpublished).

11. Evans, J. V., et al., "SATSUM Plots of NAVSAT Satellite Tracks of December 16 and December 17, 1971" (unpublished).

12. Feinblum, D. A. and Horan, R. J., "Calculation of the Solar Zenith Angle," Bell Laboratories, Unpublished Work, September 13, 1973.

13. Feldstein, Y. I., "Some Problems Concerning the Morphology of Auroras and Magnetic Disturbances at High Latitudes," Geomagnetism and Aeronomy, 3, 183 (1963).

14. Fleury, L. and Taieb, C., "Simultaneous Measurements of Electronic Density Using Topside Soundings and Incoherent Scatter Soundings," J. Atm. Terr. Phys., 33, 904 (1971).

15. Francis, S. H., "Theory and Models of Atmospheric Acoustic-Gravity Waves and Traveling Ionospheric Disturbances," Bell Laboratories/Lincoln Laboratories Joint Radar Propagation Study, 1973.

16. Hakura, Y., "Tables and Maps of Geomagnetic Coordinates Corrected by the Higher Order Spherical Harmonic Terms," Rep't. Iono. and Space Res., 19, 2, 121 (1965).

17. Horan, R. J., "Correlations of Peak Critical Frequencies of the Ionospheric F2 Layer with Geophysical Parameters for Ft. Churchill," Bell Laboratories, Unpublished Work, September 15, 1972.

18. Huldqvist, B., "The Geomagnetic Field Lines in Higher Approximation," Arkiv För Geofysik, 3, 4, 63 (1958).

19. Matsushita, S., "Lunar Tides in the Ionosphere," Encyclopedia of Physics, Vol. 49/2, Springer, New York, 1967.

20. McIlwain, C. E., "Coordinates for Mapping the Disturbances of Magnetically-Trapped Particles," J. Geophys. Res., 66, 3681 (1961).

21. Muldrew, D. B., "F-Layer Ionization Troughs Deduced from Alouette Data," J. Geophys. Res., 70, 11 (1965).

22. Nishida, A., "Average Structure and Storm-Time Change of the Solar Topside Ionosphere at Sunspot Minimum," J. Geophys. Res., 72, 6051 (1967).

23. Roederer, J. G., "The Earth's Magnetosphere," Science, 183, 4120, 37 (1974).

24. Serson, P. H., Director, Division of Geomagnetism, Dominion Observatory, Ottawa, Canada, Private Communication (Observations made at Ft. Churchill, Manitoba, 1968).

25. Rawer, K., and Suchy, K., "Radio Observations of the Ionosphere," Encyclopedia of Physics, Vol. 49/2, Springer, New York, 1967.

26. Thomas, J. O. and Andrews, M. K., "Transpolar Ionospheric Plasma I," J. Geophys. Res., 73, 7407 (1968).

27. Tulunay, Y., and Sayers, J., "Characteristics of the Mid-Latitude Trough as Determined by the Electron Density Experiment on Ariel III," J. Atm. Terr. Phys., 33, 1737 (1971).

28. Unger, J. H. W., "Ionospheric Effects, Statistics, and Models," Bell Laboratories, Unpublished Work, September 6, 1973.

29. Valley, S. L., Handbook of Geophysical and Space Environment, McGraw-Hill Co., Inc., 1965.

30. VanZandt, T. E. and Lund, D. S., "Observations of Mid-Latitude Troughs," URSI Fall Meeting, Ann Arbor, Michigan, 1967.

Appendix A

LATITUDE OF THE TROUGH AT THE
LONGITUDE OF MILLSTONE HILL

     This appendix illustrates the model predictions of the geographic latitude of the center of the main trough at the longitude of Millstone Hill (71.49°W) as a function of local time. Figure A-1 presents curves for all integral values of K_p from 0 (most northern) through 7, as labeled on the first plot. Note that the longitude is rounded to the nearest degree.
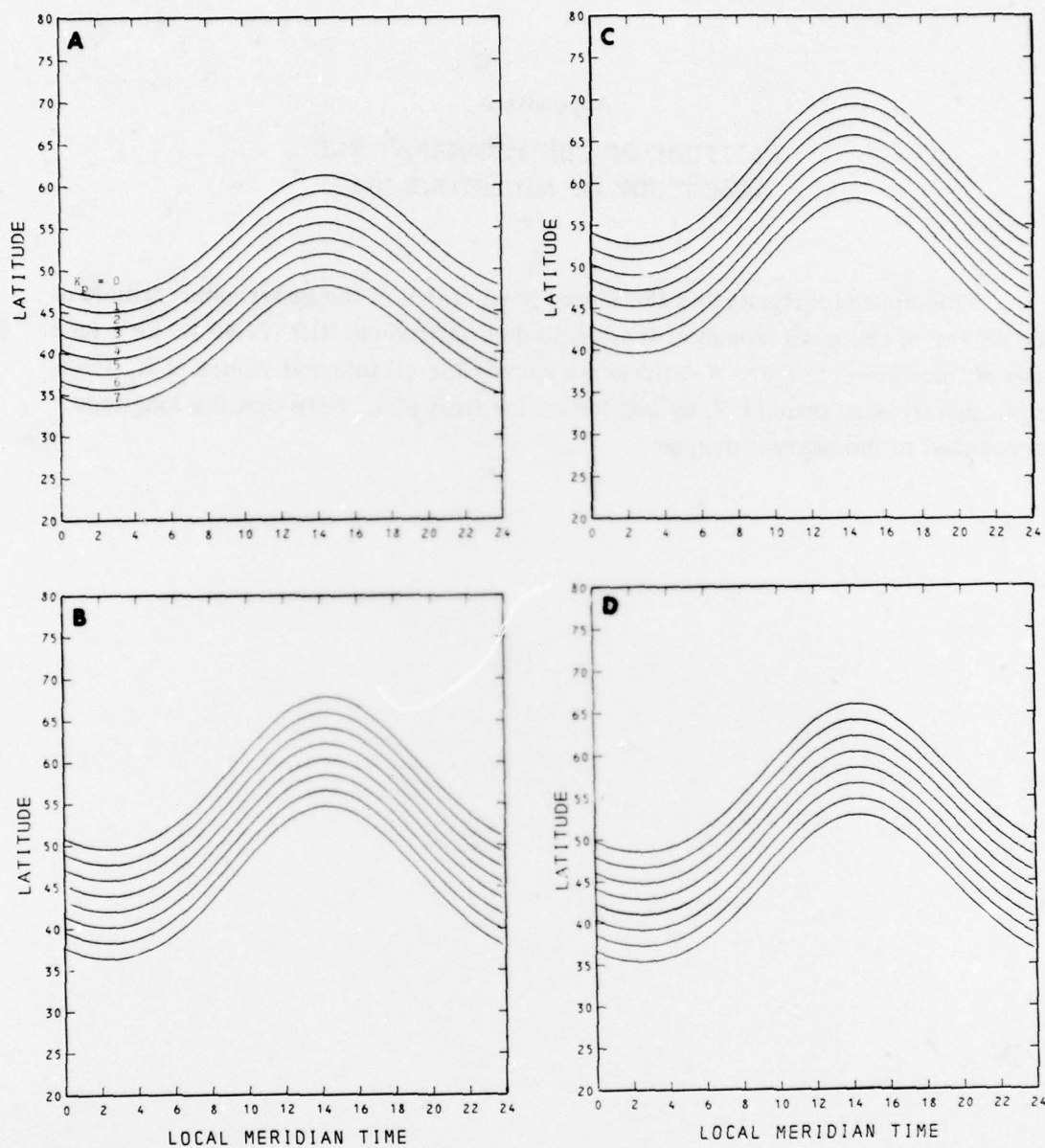
A. January 1   B. April 1   C. July 1   D. October 1

Figure A-1. Latitude of the Center of the Main Trough
at 71° West Longitude for Integral Values of K_p

Appendix B

ACCURACY TESTS OF THE LINEARIZED FITTING METHOD

This appendix documents the accuracy tests of the linearized fitting method. Table B-1 pertains to linearized method fits to artificial data with correlated Gaussian noise added to critical frequencies. Table B-2 deals with linearized method fits to artifical data with uncorrelated Gaussian noise added to altitudes.

Part A

NOTES: Unperturbed functions: $z = -0.5 + 2\left(\dfrac{h}{100} - 3\right) - 0.1\left(\dfrac{h}{100} - 3\right)^2$

Unperturbed parameters: foF2 = 5 MHz, $N_m = 3.097 \times 10^5$ e/cc,

$H_m = 325.3$ km, $S_m = 51.3$ km,

rms noise = 0.01 MHz

Critical frequencies are supplied to the fitting program at 17 altitudes from 344 km to 1000 km taken from a representative set of Alouette I data.

rms perturbation to frequency at lowest altitude $\sim \sqrt{17} \times$ rms noise.

Trial	H_m	δH_m	S_m	δS_m	N_m	δN_m
1	334.2	8.9	50.1	-0.7	3.097	(forced)
2	329.3	4.0	51.0	-0.3	3.097	
3	317.3	-8.1	52.3	0.6	3.097	
4	324.3	-1.0	50.2	-1.1	3.097	
5	328.1	2.8	51.3	0.	3.097	
6	330.0	4.6	50.5	-0.8	3.097	
7	318.7	-6.6	51.5	-0.5	3.097	
rms (1-7)		5.79		0.66		
8	333.2	7.9	50.6	-0.7	3.01	-0.09
9	332.0	6.7	50.6	-0.7	2.99	-0.11
10	329.7	4.4	50.6	-0.7	3.06	-0.04
rms (1-10)		6.01		0.67		

Part B

NOTE: Same as Part A, except foF2 = 2 MHz, $N_m = 4.96 \times 10^5$ e/cc

Trial	H_m	δH_m	S_m	δS_m	N_m	δN_m
1	328.1	2.8	51.5	0.2	0.552	0.056
2	327.2	1.9	49.9	-1.4	0.478	-0.018
3	333.3	8.0	48.4	-2.9	0.499	0.003
4	331.0	5.7	50.4	-0.9	0.520	0.024
5	328.7	3.4	48.1	-3.2	0.506	0.010
6	332.7	7.4	48.3	-3.0	0.516	0.020
7	329.5	4.2	50.1	-1.2	0.519	0.023
8	332.4	7.1	47.9	-3.4	0.508	0.012
9	325.7	0.4	51.8	0.5	0.589	0.093
10	330.8	5.5	51.1	-0.2	0.506	0.010
rms		5.2		2.1		0.037

/

LINEARIZED METHOD FITS TO ARTIFICIAL
WITH CORRELATED GAUSSIAN NOISE AD
TO CRITICAL FREQUENCIES

Part C

me as Part B, except rms noise = 0.02 MHz

H_m	δH_m	S_m	δS_m	N_m	δN_m
329.0	3.7	58.2	6.9	0.556	0.060
329.0	3.7	46.6	-4.7	0.519	0.023
331.5	6.2	48.5	-2.8	0.480	-0.016
337.4	12.1	49.5	-1.8	0.496	0.
328.2	2.9	49.5	-1.8	0.550	0.054
325.0	-0.3	49.3	-2.0	0.493	-0.003
331.8	6.5	48.5	-2.8	0.458	-0.038
317.4	-7.9	57.8	6.5	0.500	0.004
333.4	8.1	48.4	-2.9	0.487	-0.009
327.2	1.9	61.6	10.3	0.551	0.055
	6.3		5.0		0.034

Part D

me as Part C, except:

ed function: $z = -0.5 + 3\left(\dfrac{h}{100} - 3\right) - 0.1\left(\dfrac{h}{100} - 3\right)^2 + 0.01\left(\dfrac{h}{100} - 3\right)^3$

ed parameters: H_m = 325.3 km, S_m = 51.2 km

H_m	δH_m	S_m	δS_m	N_m	δN_m
321.8	-3.5	50.9	-0.3	0.497	0.001
319.2	-6.1	56.2	5.0	0.460	-0.036
329.0	3.7	61.2	10.0	0.468	-0.028
326.6	1.3	59.7	8.5	0.429	-0.067
336.1	10.8	56.3	5.1	0.444	-0.052
332.9	7.6	51.8	0.6	0.456	-0.040
336.0	10.7	46.3	-4.9	0.557	0.061
323.6	1.7	61.8	10.6	0.445	-0.051
321.1	-4.2	55.3	4.1	0.502	0.006
328.5	3.2	50.9	-0.3	0.415	-0.081
	6.2		6.1		0.049

Part E

NOTE: Same as Part C, except:

Unperturbed function:

$$z = -0.5 + 2\left(\frac{h}{100} - 3\right) - 0.2\left(\frac{h}{100} - 3\right)^2 + 0.01\left(\frac{h}{100}\right.$$

Unperturbed parameters: H_m = 325.7 km, S_m

Trial	H_m	δH_m	S_m	δS_m	N_m
1	322.3	-3.4	58.6	6.0	0.40
2	321.1	-4.6	70.4	17.8	0.43
3	322.9	-2.8	57.4	4.8	0.45
4	322.7	-3.0	55.3	2.7	0.51
5	321.1	-4.6	60.5	7.9	0.44
6	318.8	-6.9	56.8	4.2	0.45
7	321.3	-4.4	60.3	7.7	0.49
8	318.3	-7.4	63.3	10.7	0.49
9	323.0	-2.7	59.4	6.8	0.53
10	324.0	-1.7	63.6	11.0	0.55
11	329.7	4.0	50.4	-2.2	0.42
12	327.5	1.8	52.8	0.2	0.45
rms		4.3		8.2	

Part F

NOTE: Same as Part E except rms noise = 10 km

Trial	H_m	δH_m	S_m	δS_m	N_m
1	324.9	0.9	54.3	4.3	0.488
2	333.8	9.8	50.4	0.4	0.466
3	287.8	-36.2	63.3	13.3	0.546
4	336.0	12.0	45.2	-4.8	0.477
5	308.7	-15.3	55.5	5.5	0.507
6	281.9	-42.1	67.3	17.3	0.553
7	340.8	16.8	44.7	-5.3	0.476
8	319.6	-4.4	60.1	10.1	0.476
9	244.8	-79.2	58.1	8.1	0.747
10	353.2	29.2	38.2	-11.8	0.464
11	337.9	13.9	46.4	-3.6	0.467
rms		31.88		9.03	

processor time for 11 trials on IBM 370/165: 29.2 sec.

$$0.01\left(\frac{h}{100} - 3\right)^3$$

km, $S_m = 52.6$ km

N_m	δN_m
0.401	-0.095
0.432	-0.064
0.455	-0.041
0.511	0.015
0.441	-0.055
0.455	-0.041
0.494	-0.002
0.493	-0.003
0.535	0.039
0.550	0.054
0.422	-0.074
0.451	-0.045
	0.051

km

N_m	δN_m	No. of Major Steps Needed
0.488	-0.008	80
0.466	-0.030	70
0.546	0.050	86
0.477	-0.019	74
0.507	0.012	74
0.553	0.058	98
0.476	-0.020	72
0.476	-0.020	69
0.747	-0.252	99
0.464	-0.032	80
0.467	-0.029	62
	0.082	

0.2 sec.

3

Table B-2
LINEARIZED METHOD FITS TO ARTIFICIAL DATA WITH UNCORRELATED GAUSSIAN NOISE ADDED TO ALTITUDES

Part A

NOTES: Unperturbed function:

$$z = \frac{1}{S_m}\left(h - H_m\right) - 0.2\left(\frac{h - H_m}{100}\right)^2 + 0.01\left(\frac{h - H_m}{100}\right)$$

Unperturbed parameters:

$foF2 = 2$ MHz, $\qquad N_m = 0.496 \times 10^5$ e/cc, $\qquad H_m = 324$ km,

$S_m = 33.33$ km, $\qquad$ rms noise = 4 km,

Program estimate of $N_m = 0.480 \times 10^5$ e/cc

Critical frequencies are presented to fitting program at same (unperturbed) altitudes as in Table B-1.

Trial	H_m	δH_m	S_m	δS_m
1	328.4	4.4	34.6	1.3
2	325.4	1.4	33.8	0.5
3	333.0	9.0	31.0	-2.3
4	322.8	-1.2	35.3	2.0
5	320.8	-3.2	36.7	3.4
6	330.3	6.3	33.0	-0.3
7	321.6	-2.4	36.4	3.1
8	321.7	-2.3	36.6	3.3
9	330.9	6.9	32.4	-0.9
10	326.3	2.3	33.7	0.4
11	326.9	2.9	34.2	0.9
rms		4.5		2.0

Part B

NOTE: Same as Part A, except: rms noise = 10 km.

Trial	H_m	δH_m	S_m	δS_m
1	321.6	-2.4	36.0	2.7
2	321.4	-2.6	37.2	3.9
3	321.4	-2.6	34.5	1.2
4	325.8	1.8	33.6	0.3
5	330.0	6.0	33.4	0.1
6	324.7	0.7	36.2	2.9
7	315.9	-8.1	38.3	5.0
8	327.1	3.1	35.3	2.0
9	324.1	0.1	35.8	2.5
10	326.1	2.1	38.0	4.7
rms		3.7		3.0

Appendix C

ACCURACY TESTS OF A BASIC NONLINEAR FITTING METHOD

This appendix documents the accuracy tests of a basic nonlinear fitting method. Table C-1 deals with nonlinear least-squares fits to artificial data with uncorrelated noise added to altitudes.

Part A

NOTES: Unperturbed function: $z = \dfrac{1}{S_m}\left(h - H_m\right)$

Unperturbed parameters: $foF2 = 2$ MHz, $N_m = 0.496 \times 10^5$ e/cc,

$H_m = 324$ km, $S_m = 50$ km,

rms noise = 4 km

N_m is determined by least squares fit. Data is presented to fitting program at the same (unperturbed) altitudes as in Table B-1.

Trial	H_m	δH_m	S_m	δS_m	N_m	δN_m	No. of Major Steps Needed
1	337.6	13.6	44.1	-5.9	0.480	-0.016	48
2	306.7	-17.3	60.0	10.0	0.515	0.020	62
3	318.0	-6.0	53.1	3.1	0.509	0.014	54
4	338.8	14.8	43.4	-6.6	0.475	-0.021	44
5	327.8	3.8	47.9	-2.1	0.488	-0.008	55
6	322.1	-1.9	51.5	1.5	0.498	0.003	58
7	293.5	-30.5	58.3	8.3	0.571	0.076	51
8	321.3	-2.7	48.3	-1.7	0.508	0.013	60
9	320.7	-3.3	49.4	-0.6	0.501	0.006	53
10	338.1	14.1	43.4	-6.6	0.480	-0.016	52
11	331.1	7.1	45.4	-4.6	0.487	-0.009	44
rms		13.3		5.5		0.026	

processor time for 11 trials on IBM 370/165: 16.9 sec.

NOTE

Trial

1
2
3
4
5
6
7
8
9
10
11

rms

rms (1-

process

NOTE

Trial

1
2
3
4
5
6
7
8
9
10
11

rms

process

Table C-1

NONLINEAR LEAST SQUARES FIT
WITH UNCORRELATED NOISE A

Part B

NOTE: Same as Part A, except rms noise = 10 km.

Trial	H_m	δH_m	S_m	δS_m	N_m	δN_m	No. of Major Steps Needed
1	273.6	-50.4	56.3	6.3	0.637	0.142	63
2	334.5	10.5	43.8	-6.2	0.478	-0.018	44
3	332.5	8.5	49.1	-0.9	0.481	-0.015	36
4	324.6	0.6	51.3	1.3	0.485	-0.011	55
5	311.2	-12.8	57.1	7.1	0.505	0.010	45
6	229.3	-94.7	84.0	34.0	0.707	0.212	73
7	321.1	-2.9	62.3	12.3	0.476	-0.020	46
8	348.0	24.0	39.6	-10.4	0.463	-0.033	51
9	332.5	8.5	45.8	-4.2	0.490	-0.006	43
10	333.6	9.6	46.3	-3.7	0.487	-0.009	45
11	157.2	-166.8	115.6	65.6	0.942	0.447	75
rms		60.6		23.1		0.156	
rms (1-5, 7-10)		20.1		6.9		0.050	

processor time for 11 trials on IBM 370/165: 16.3 sec.

Part C

NOTE: Same as Part A, except

Unperturbed function is: $z = \dfrac{1}{S_m}\left(h - H_m\right) - 0.2\left(\dfrac{h - H_m}{100}\right)^2$

Trial	H_m	δH_m	S_m	δS_m	N_m	δN_m	No. of Major Steps Needed
1	321.4	-2.6	50.2	0.2	0.501	0.006	51
2	315.0	-9.0	49.9	-0.1	0.528	0.033	53
3	327.4	3.4	49.2	-0.8	0.499	0.004	66
4	320.1	-3.9	49.7	-0.3	0.509	0.014	53
5	321.5	-2.5	50.1	0.1	0.501	0.006	45
6	319.1	-4.9	50.9	0.9	0.505	0.010	47
7	324.5	0.5	50.4	0.4	0.488	-0.008	42
8	329.2	5.2	50.1	0.1	0.483	-0.013	42
9	322.3	-1.7	50.1	0.1	0.500	0.005	55
10	319.9	-4.1	51.3	1.3	0.497	0.002	52
11	314.8	-9.2	50.4	0.4	0.519	0.024	61
rms		5.0		0.6		0.014	

processor time for 11 trials on IBM 370/165: 16.4 sec.

Trial	H_m	δH_m	S_m	δS_m
1	344.1	20.1	45.7	-4
2	301.9	-22.1	53.1	3
3	311.5	-12.5	48.2	-1
4	332.4	8.4	48.0	-2
5	315.9	-8.1	53.2	3
6	333.1	9.1	49.4	-0
7	329.5	5.5	49.6	-0
8	333.4	9.4	51.4	1
9	333.0	9.0	46.7	-3
10	320.7	-3.3	52.1	2
11	312.3	11.7	51.5	1
rms		12.1		2

processor time for 11 trials on IBM 370/1

Trial	H_m	δH_m	S_m	δS_m
1	270.7	-53.3	61.3	11
2	315.8	-8.2	53.3	3
3	333.4	9.4	46.7	-3
4	304.1	-19.9	58.1	8
5	303.7	-20.3	56.7	6
6	325.5	1.5	49.5	-0
7	330.6	6.6	52.7	2
8	328.6	4.6	49.2	-0
9	319.3	-4.7	49.0	-1
10	304.1	-19.9	55.1	5
11	338.0	14.0	42.4	-7
rms		20.2		5

processor time for 11 trials on IBM 370/1

RES FITS TO ARTIFICIAL DATA
NOISE ADDED TO ALTITUDES

Part D

rms noise = 10 km.

	δS_m	N_m	δN_m	No. of Major Steps Needed
	-4.3	0.461	-0.035	53
	3.1	0.531	0.036	51
	-1.8	0.535	0.040	55
	-2.0	0.487	-0.009	49
	3.2	0.483	-0.013	35
	-0.6	0.480	-0.016	50
	-0.4	0.485	-0.011	38
	1.4	0.472	-0.024	35
	-3.3	0.488	-0.008	51
	2.1	0.487	-0.009	44
	1.5	0.506	0.011	56
	2.4		0.022	

BM 370/165: 15.0 sec.

Part E

unperturbed function is:

$$0.2\left(\frac{h - H_m}{100}\right)^2 + 0.01\left(\frac{h - H_m}{100}\right)^3$$

	δS_m	N_m	δN_m	No. of Major Steps Needed
	11.3	0.622	0.127	91
	3.3	0.510	0.015	46
	-3.3	0.483	-0.013	71
	8.1	0.530	0.035	87
	6.7	0.528	0.033	74
	-0.5	0.490	-0.006	84
	2.7	0.478	-0.018	61
	-0.8	0.483	-0.013	98
	-1.0	0.520	0.025	93
	5.1	0.530	0.035	91
	-7.6	0.483	-0.013	94
	5.7		0.044	

BM 370/165: 30.6 sec.

DISTRIBUTION LIST

Aeronomy Corporation
P.O. Box 2209, Station A
Champaign, Illinois 61802

Attn: Dr. S. A. Bowhill

Air Force Cambridge Research Labs
Ionospheric Laboratory Code L.I.R.
L. G. Hanscom Field
Bedford, Massachusetts 01730

Attn: Dr. J. Aarons

Air Force Cambridge Research Labs
Ionospheric Laboratory Code CRPA
L. G. Hanscom Field
Bedford, Massachusetts 97130

Attn: Dr. T. J. Elkins
      Major H. Fischer

CALSPAN
4455 Genesse Street
P.O. Box 235
Buffalo, New York 14221

Attn: Dr. W. Blum
      Mr. D. Phillips

Commander
Rome Air Development Center
Griffith AFB, New York 13441

Attn: Mr. V. J. Coyne

Commander
Ballistic Missile Defense Systems
  Command
P.O. Box 1500
Huntsville, Alabama 35807

Attn: Mr. R. C. Wicks (BMDSC-TEN)
      Mr. D. E. Bowers (BMDSC-TEB)
      Mr. H. M. Porter (BMDSC-HS)

Department of the Army
Ballistic Missile Defense Program
  Office
Commonwealth Building
1300 Wilson Blvd
Arlington, Virginia 22209

Attn: Mr. J. H. Best
      DACS-SAT
      Mr. J. J. Shea
      Col. L. E. Oder

Department of Elec. Engineering
N-7034 Trondheim — NTH
Norway

Attn: Professor Tor Hagfors

Director
Advanced Research Project Agency
Strategic Technology Office
1400 Wilson Blvd
Arlington, Virginia 22209

Attn: Dr. D. Levine
      Mr. R. A. Moore

Director
Defense Nuclear Agency (RAAE)
Washington, D. C. 20305

Attn: Mr. D. E. Evelyn
      Dr. H. C. Fitz
      Mr. P. Fleming
      Mr. A. C. Meier

Director
Ballistic Missile Defense Advanced
  Technology Center
P.O. Box 1500
Huntsville, Alabama 35807

Attn: Mr. M. Capps
      Dr. W. R. Mahaffey

Director
Ballistic Missile Defense Advanced
  Technology Center
Commonwealth Building
1300 Wilson Blvd
Arlington, Virginia 22209

Attn: Dr. J. Gilstein

Director
Defense Research and Engineering
Pentagon
Washington, D. C.

Attn: Mr. W. Delaney

Director
U.S. Naval Research Laboratory
4555 Overlook Avenue, SW
Washington, D.C. 20375

Attn: Dr. T. Coffey (Code 7750)
      Dr. J. R. Davis (Code 5464)
      Dr. R. Shanny

General Electric Company
Bldg 9, Room 8
Court Street
Syracuse, New York 13201

Attn: Dr. G. H. Millman

General Electric Company
Tempo Division
816 State Street
Santa Barbara, California 93102

Attn: Mr. T. J. Barrett

General Electric Company
Tempo Division
P.O. Drawer QQ
Santa Barbara, California 93102

Attn: Mr. R. J. Jordano

General Research Corporation
P.O. Box 3587
Santa Barbara, California 93105

Attn: Dr. J. Ise

Geophysical Institute of the
University of Alaska
College, Alaska

Attn: Prof. R. D. Hunsucker

Institute for Defense Analysis
400 Army-Navy Drive
Arlington, Virginia 22202

Attn: Dr. J. Bengston

Lockheed Missile & Space Company
3251 Hanover Street
Palo Alto, California 94303

Attn: Dr. B. M. McCormac (52-14, 201)

Massachusetts Institute of Technology
Lincoln Laboratory
P.O. Box 73
Lexington, Massachusetts 02173

Attn: Dr. D. Clark L-196
Dr. R. Crane GR61-D428
Mr. S. H. Dodd
Mr. D. E. Dustin, Asst. Director
Dr. J. V. Evans
Dr. A. Freed
Dr. M. A. Herlin
Mr. G. B. Morse
Dr. J. Rheinstein
Dr. J. Salah
Dr. R. H. Wand

McDonnell-Douglas Astronautics Co.
5301 Bolsa Avenue
Huntington Beach, California 92647

Attn: Mr. D. Dean/A3-253-11-2

Mission Research Corporation
735 State Street, P.O. Drawer 719
Santa Barbara, California 93102

Attn: Dr. R. W. Hendrick
Dr. D. Sowle
Dr. R. L. Bogusch

NOAA
Space Environment Laboratory
Boulder, Colorado 80302

Attn: Dr. G. W. Adams
Dr. G. M. Lerfald

Office of Naval Research
Physics Program
800 N. Qunicy Street
Arlington, Virginia 22217

Attn: Dr. J. G. Dardis

Physical Dynamics, Inc.
P.O. Box 604
College Park Station
Detroit, Michigan 48221

Attn: Dr. A. R. Hochstim

Raytheon Company
Sudbury Engineering Facility
528 Boston Post Road
Sudbury, Massachusetts 01776

Attn: Dr. G. Meltz
Dr. G. D. Thome

R & D Associates
P.O. Box 3580
Santa Monica, California 90405

Attn: Dr. R. E. Le Levier

Riverside Research Institute
80 West End Avenue
New York, New York 10023

Attn: Dr. J. B. Minkoff

Science Applications, Inc.
P.O. Box 2351
1200 Prospect Street
La Jolla, California 92037

Attn: Dr. L. Linson
Dr. G. Stuart

Spectra Research Systems
2212 Dupont Drive
Irvine, California 92664

Attn: Dr. M. Sandhu

Stanford Research Institute
306 Wynn Drive
Huntsville, Alabama 35805

Attn: Mr. J. C. Belote
Mr. D. Divis

Stanford Research Institute
333 Ravenswood Avenue
Menlo Park, California 94025

Attn: Dr. W. G. Chesnut
Dr. E. J. Fremouw
Mr. V. Gonzalez
Dr. R. L. Leadabrand
Dr. D. McDaniel

The Pennsylvania State University
E E East
University Park, Pennsylvania 16802

Attn: Prof. J. S. Nisbet

University of California, San Diego
Dept. of AP & IS
La Jolla, California 92037

Attn: Mr. P. M. Banks

U.S. Army Air Defense Command
Ent Air Force Base
Colorado Springs, Colorado 80912

Attn: ADGEP-E

U.S. Army Ballistic Research Lab
Aberdeen Proving Ground
Maryland 21005

Attn: Dr. L. J. Puckett